IOWA STATE UNIVERSITY
Digital Repository

Graduate Theses and Dissertations

Iowa State University Capstones, Theses and Dissertations

2011

# Indirectly detected chemical shift correlation NMR spectroscopy in solids under fast magic angle spinning

Kanmi Mao
*Iowa State University*

Follow this and additional works at: https://lib.dr.iastate.edu/etd

 Part of the Chemistry Commons

Recommended Citation
Mao, Kanmi, "Indirectly detected chemical shift correlation NMR spectroscopy in solids under fast magic angle spinning" (2011). *Graduate Theses and Dissertations*. 12249.
https://lib.dr.iastate.edu/etd/12249

This Dissertation is brought to you for free and open access by the Iowa State University Capstones, Theses and Dissertations at Iowa State University Digital Repository. It has been accepted for inclusion in Graduate Theses and Dissertations by an authorized administrator of Iowa State University Digital Repository. For more information, please contact digirep@iastate.edu.

www.manaraa.com

# Indirectly detected chemical shift correlation NMR spectroscopy in solids under fast magic angle spinning

by

**Kanmi Mao**

A dissertation submitted to the graduate faculty

in partial fulfillment of the requirements for the degree of

DOCTOR OF PHILOSOPHY

Major: Chemistry

Program of Study Committee:
Marek Pruski, Co-major Professor
Aaron Sadow, Co-major Professor
Klaus Schmidt-Rohr
Gordon Miller
Robert Houk

Iowa State University

Ames, Iowa

2011

Copyright © Kanmi Mao, 2011. All rights reserved.

www.manaraa.com

## Table of Contents



www.manaraa.com

www.manaraa.com

## Acknowledgements

First and foremost, I owe my deepest gratitude to my Ph.D. advisor Dr. Marek Pruski, whose support, encouragement and guidance enable me to understand the knowledge in solid-state NMR as well as the broad view of scientific research. He not only taught me how to progress the current research, and also helped me develop my further career.

I deeply appreciate the invaluable suggestions and great support provided by my committee members: Dr. Aaron Sadow, Dr. Klaus Schmidt-Rohr, Dr. Gordon Miller and Dr. Robert Houk.

This work would not have been possible without my colleagues in Dr. Marek Pruski's group. I would like to thank Dr. Jerzy W. Wiench for teaching me how to write pulse sequences and operate the spectrometers, Dr. Takeshi Kobayashi for collaboration on PFP, CTAB/CPB and corrole projects, and Mrs. Stacey M. Althaus for cooperation on N-15 and coal projects. I also would like to thank Dr. Victor Shang-Yi Lin and his group for providing samples and inspirable discussions. I also wish to acknowledge Dr. John Stringer from Agilent for designing the prototype probe for fast MAS, Dr. Gordon J. Kennedy from ExxonMobil for cooperation on coal project, and Dr. Marek J. Potrzebowski and his group for corrole project.

Thanks to friends in other NMR groups for helping me about my research: Dr. Xueqian Kong, Dr. Yanyan Hu, Mr. Yongchao Su and Mrs. Yuan Zhang. Thanks to all my friends during my stay at Ames in different manners.

Finally, I would like to dedicate my thesis to my parents, Yuechang Mao and Jianfei Wang, for their unconditional support and love. Also, I would like to express my sincere gratitude to my husband, Rui Chen, who is the only other half that makes me whole.

www.manaraa.com

## Abstract

The development of fast magic angle spinning (MAS) opened up an opportunity for the indirect detection of insensitive low-γ nuclei (e.g., $^{13}C$ and $^{15}N$) via the sensitive high-γ nuclei (e.g., $^{1}H$ and $^{19}F$) in solid-state NMR, with advanced sensitivity and resolution. In this thesis, new methodology utilizing fast MAS is presented, including through-bond indirectly detected heteronuclear correlation (HETCOR) spectroscopy, which is assisted by multiple RF pulse sequences for $^{1}H$-$^{1}H$ homonuclear decoupling. Also presented is a simple new strategy for optimization of $^{1}H$-$^{1}H$ homonuclear decoupling. As applications, various classes of materials, such as catalytic nanoscale materials, biomolecules, and organic complexes, are studied by combining indirect detection and other one-dimensional (1D) and two-dimensional (2D) NMR techniques.

Indirectly detected through-bond HETCOR spectroscopy utilizing refocused INEPT (INEPTR) mixing was developed under fast MAS (Chapter 2). The time performance of this approach in $^{1}H$ detected 2D $^{1}H\{^{13}C\}$ spectra was significantly improved, by a factor of almost 10, compared to the traditional $^{13}C$ detected experiments, as demonstrated by measuring naturally abundant organic-inorganic mesoporous hybrid materials. The through-bond scheme was demonstrated as a new analytical tool, which provides complementary structural information in solid-state systems in addition to through-space correlation.

To further benefit the sensitivity of the INEPT transfer in rigid solids, the combined rotation and multiple-pulse spectroscopy (CRAMPS) was implemented for homonuclear $^{1}H$ decoupling under fast MAS (Chapter 3). Several decoupling schemes ($PMLG5^{\bar{x}}_{m}$, $PMLG5^{\bar{x}x}_{mm}$ and SAM3) were analyzed to maximize the performance of through-bond transfer based on decoupling efficiency as well as scaling factors. Indirect detection with assistance of $PMLG5^{\bar{x}}_{m}$ during INEPTR transfer proved to offer the highest sensitivity gains of 3-10. In addition, the CRAMPS sequence was applied under fast MAS to increase the $^{1}H$ resolution during $t_1$ evolution in the traditional, $^{13}C$ detected HETCOR scheme. Two naturally abundant solids, tripeptide *N-formyl*-L-methionyl-L-leucyl-L-phenylalanine (f-MLF-OH) and brown coal, with well ordered and highly disordered structures, respectively, are studied to confirm the capabilities of these techniques.

www.manaraa.com

Concomitantly, a simple optimization of $^{1}H$ homonuclear dipolar decoupling at MAS rates exceeding 10 kHz was developed (Chapter 4). The fine-tuned decoupling efficiency can be obtained by minimizing the signal loss due to transverse relaxation in a simple spin-echo experiment, using directly the sample of interest. The excellent agreement between observed decoupling pattern and earlier theoretical predictions confirmed the utility of this strategy.

The properties of naturally abundant surface-bound fluorocarbon groups in mesoporous silica nanoparticles (MSNs) were investigated by the above-mentioned multidimensional solid-state NMR experiments and theoretical modeling (Chapter 5). Two conformations of (pentafluorophenyl)propyl groups (abbreviated as PFP) were determined as PFP-prone and PFP-upright, whose aromatic rings are located above the siloxane bridges and in roughly upright position, respectively. Several 1D and 2D NMR techniques were implemented in the characterizations, including indirectly detected $^{1}H\{^{13}C\}$ and $^{19}F\{^{13}C\}$ 2D HETCOR, Carr-Purcell-Meiboom-Gill (CPMG) assisted $^{29}Si$ direct polarization and $^{29}Si\{^{19}F\}$ 2D experiments, 2D double-quantum (DQ) $^{19}F$ MAS NMR spectra and spin-echo measurements. Furthermore, conformational details of two types of PFP were confirmed by theoretical calculation, operated by Dr. Takeshi Kobayashi.

Finally, the arrangement of two surfactants, cetyltrimetylammoium bromide (CTAB) and cetylpyridinium bromide (CPB), mixed inside the MSN pores, was studied by solid-state NMR (Chapter 6). By analyzing the $^{1}H$–$^{1}H$ DQMAS and NOESY correlation spectra, the CTAB and CPB molecules were shown to co-exist inside the pores without forming significant monocomponent domains. A “folded-over” conformation of CPB headgroups was proposed according to the results from $^{1}H$–$^{29}Si$ 2D HETCOR.

www.manaraa.com

# Chapter 1

# Introduction to solid-state NMR

## 1.1 The basics of solid-state NMR spectroscopy

Since the first observation of nuclear magnetic resonance (NMR) in solid [1] and solution samples [2] in 1940s, NMR has grown as an essential technique widely implemented in numerous areas of science. Due to the lack of fast motional averaging of anisotropic interactions, the resolution of solid-state NMR is remarkably lower than that encountered in solution NMR, which also causes relatively lower sensitivity. In order to improve the quality of solid spectra, magic angle spinning (MAS) was developed in 1958 [3], which assists in removing the orientation-dependent interactions (e.g., chemical shift anisotropy and dipolar couplings) by mechanical sample rotation. With the technological progress in probe technology, the spinning frequencies have approached 80 kHz [4], which provides the possibility of eliminating strong homonuclear dipolar couplings between $^{1}$H nuclei. The resulting enhancement of resolution enabled successful implementation of indirect detection in solid-state NMR [5-8] which greatly benefits the sensitivity of multidimensional correlation spectra. In addition, through-bond heteronuclear spectroscopy via scalar (J) coupling is feasible due to the extended relaxation time under fast MAS [9], providing a complementary alternative to cross polarization (CP) that offers through-space correlations based on dipolar interactions. Here, some basic solid-state NMR concepts are addressed and several techniques closely related to our research are described.

*Semi-classical model of NMR*

The semi-classical model is suitable to describe the NMR properties of isolated spin-1/2 nuclei. The net magnetization $\vec{M}$ is considered as the vectorial sum of all individual nuclear

www.manaraa.com

magnetic moments, which is non-zero in the presence of an external magnetic field (Figure 1.1), and is given by

$$\vec{M} = \gamma \vec{J}\,, \tag{1.1}$$

where $\gamma$ is the magnetogyric ratio, a constant for a given nucleus, and $\vec{J}$ is the net spin angular momentum.

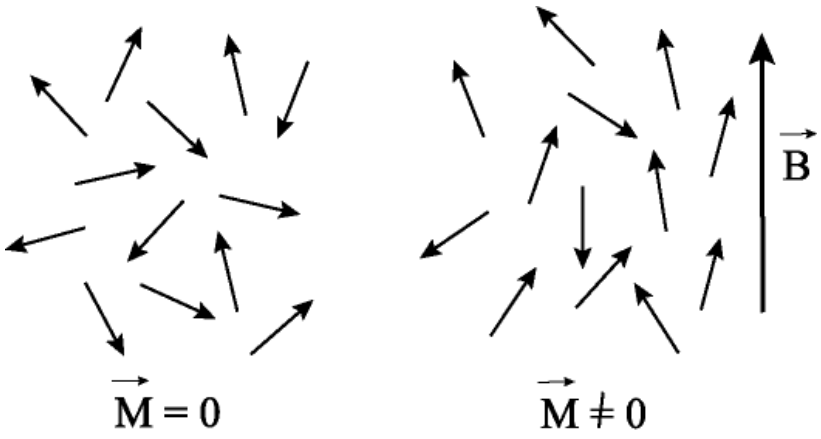


**Figure 1.1**. The semi-classical model of the net magnetization, $\vec{M}$. In the absence of the external magnetic field, $\vec{M} = 0$, due to the orientations of individually magnetic moments (indicated by small vectors) being randomly distributed. With the field $\vec{B}$ applied, the non-zero net magnetization appears along the $\vec{B}$ direction.

If the magnetic momentum $\vec{M}$ is placed in a homogeneous magnetic field $\vec{B}$, a torque $\vec{N}$ is exerted as

$$\vec{N} = \vec{M} \times \vec{B} \tag{1.2}$$

Also, the relationship between torque $\vec{N}$ and angular momentum $\vec{J}$ is

www.manaraa.com

$$\vec{N} = \frac{d}{dt}\vec{J} \tag{1.3}$$

Combining Equations 1.1, 1.2 and 1.3, the motion of the magnetization is

$$\frac{d}{dt}\vec{M} = \gamma \vec{M} \times \vec{B}, \tag{1.4}$$

which indicates that the magnetization $\vec{M}$ precesses around $\vec{B}$ at a constant frequency $\omega = -\gamma B$. In NMR experiments, the external magnetic field is generally assumed to be oriented along the z direction, $\vec{B} = (0, 0, B_0)$, and the corresponding precession frequency is called the Larmor frequency $\omega_0$. For a nucleus with magnetogyric ratio $\gamma$ in a fixed magnetic field

$$\omega_0 = \gamma B_0 \tag{1.5}$$

To conveniently describe the NMR experiments, the so-called rotating frame of reference is usually employed. For the observer in the laboratory frame, the coordinates of the rotating frame are rotating with the Larmor frequency, in the same sense. Thus, the precessing motions of the nuclear magnetic moments are frozen in the rotating frame, if only an external magnetic field is applied.

*Quantum mechanical concepts of NMR*

*Zeeman interaction*

For an isolated spin in a static, homogenous magnetic field, the Hamiltonian $\hat{H}$ of that spin is associated with the Zeeman interaction

$$\hat{H} = -\hat{\mu} \cdot \vec{B}_0 = -\gamma \hbar \hat{I} \cdot \vec{B}_0 = -\gamma \hbar \hat{I}_z B_0, \tag{1.6}$$

where the nuclear magnetic moment operator, $\hat{\mu} = \gamma \hbar \hat{I}$, the nuclear spin operator, $\hat{I} = (\hat{I}_x, \hat{I}_y, \hat{I}_z)$, and $\vec{B}_0 = (0, 0, B_0)$.

www.manaraa.com

In most NMR experiments the Zeeman interaction is the dominant part of the Hamiltonian. However, the Zeeman interaction term alone is not a useful source of structural information. The local fields arising from other interactions, such as chemical shift and dipolar couplings, which depend on the distribution of other nuclei and electrons in the vicinity of the observed spin, provide structural information on the atomic scale.

*Chemical shift interaction*

One contribution to the local field is produced by the electron cloud around the nuclei that is affected by the magnetic field $\vec{B}_0$. This local field causes the change of the resonance frequency in the NMR spectrum, referred to as chemical shift.

The chemical shift Hamiltonian of a certain spin I is

$$\hat{H}_{cs} = -\gamma\hbar\vec{I}^{\mathrm{T}} \cdot \sigma \cdot \vec{B}_0 \tag{1.7}$$

Here $\sigma$ is a second-rank tensor, which is represented by a 3 x 3 matrix in a laboratory frame of reference. In the case of $\vec{B}_0 = (0,0,B_0)$, the truncated chemical shift Hamiltonian is

$$\hat{H}_{cs} = -\gamma\hbar\hat{I}_z\sigma_{zz}^{lab}B_0 \tag{1.8}$$

The relative frequency change due to the chemical shift interactions is

$$\omega_{cs} = -\gamma\sigma_{zz}^{lab}B_0 = -\omega_0\sigma_{zz}^{lab} \tag{1.9}$$

In order to examine $\omega_{cs}$ further, the chemical shielding tensor is rewritten in the principal axis frame (PAF) associated with the orientation of the local molecular framework, as shown in Figure 1.2. In terms of principal values, $\omega_{cs}$ can be decomposed into two parts, the isotropic component and the anisotropic component:

$$\omega_{cs} = \omega_{cs}^{iso} + \omega_{cs}^{aniso} = -\omega_0\sigma_{iso} - \frac{1}{2}\omega_0\Delta\left\{3\cos^2\theta - 1 + \eta\sin^2\theta\cos 2\phi\right\}, \tag{1.10}$$

www.manaraa.com

where $\theta$ and $\phi$ are angles defined in PAF, $\sigma_{iso} = \frac{1}{3}(\sigma_{xx}^{PAF} + \sigma_{yy}^{PAF} + \sigma_{zz}^{PAF})$, $\Delta = \sigma_{zz}^{PAF} - \sigma_{iso}$, and $\eta = (\sigma_{xx}^{PAF} - \sigma_{yy}^{PAF}) / \sigma_{zz}^{PAF}$.

In a typical powdered sample, each molecular orientation has a different chemical shift, depending on the specific values of $\theta$ and $\phi$. The resulting powder spectrum is a superposition of orientation-dependent contributions from all possible orientations $0 \leq \theta \leq \pi$ and $0 \leq \phi \leq 2\pi$.

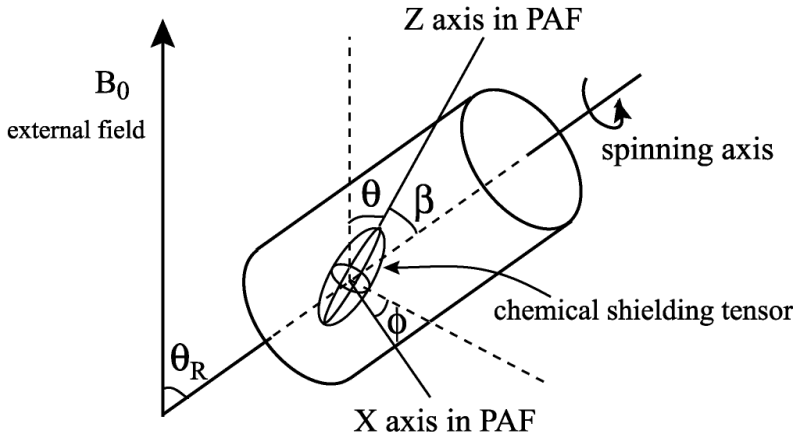


**Figure 1.2**. The illustration of the principal axis frame (PAF) in the magic angle spinning experiment. The chemical shielding tensor is in ellipsoid representation. The sample is spun around an axis that aligned at the magic angle $\theta_R = 54.74^o$ with respect to the external field. (see section 1.2)

*Dipolar coupling*

Dipolar coupling, arising from the direct interaction between two magnetic dipoles, is averaged out by rapid molecular tumbling in solution, but is a major reason for line broadening in solid-state NMR. The Hamiltonian of dipolar coupling between two spins I and S is

www.manaraa.com

$$\hat{H}_{dd} = -(\frac{\mu_0}{4\pi})\gamma_I\gamma_S\hbar^2(\frac{\vec{I}\cdot\vec{S}}{r^3} - 3\frac{(\vec{I}\cdot\vec{r})(\vec{S}\cdot\vec{r})}{r^5}) \quad (1.11)$$

The dipolar coupling constant, *d*, is defined as

$$d = \frac{\mu_0}{4\pi}\hbar^2\frac{\gamma_I\gamma_S}{r^3} \quad (1.12)$$

In terms of spherical polar coordinates, the truncated homonuclear and heteronuclear dipolar Hamiltonians are written respectively as

$$\hat{H}_{dd}^{\text{homo}} = -d\frac{1}{2}(3\cos^2\theta - 1)[3\hat{I}_z\hat{S}_z - \hat{I}\cdot\hat{S}] \quad (1.13)$$

$$\hat{H}_{dd}^{\text{hetero}} = -d(3\cos^2\theta - 1)\hat{I}_z\hat{S}_z \quad (1.14)$$

The distance $r$ between spins I and S, and angle $\theta$ are defined in Figure 1.3.

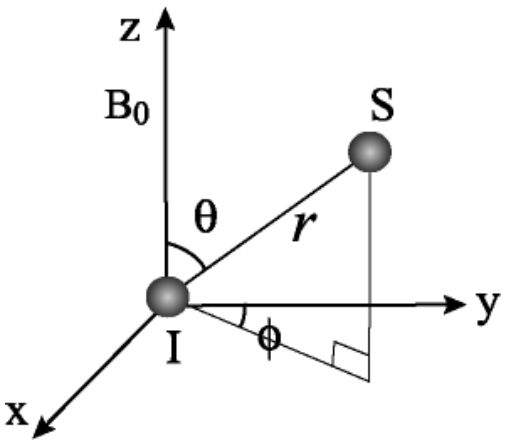


**Figure 1.3**. Illustration of I-S dipolar coupling with respect to the applied field, $B_0$.

In solid-state NMR, the indirect coupling of spins through the bonding electrons, typically referred to as scalar (J) coupling, is often neglected due to much smaller magnitude compared to other interactions. However, through-bond spectroscopy is becoming feasible in solids, as will be described in Section 1.4 and in Chapters 2, 3 and 5.

*Quadrupolar coupling*

www.manaraa.com

For nuclei with a spin greater than one-half, the distributions of nuclear charges are no longer spherical, which generates the electric quadrupole moments that can interact with the gradients of electric fields due to the electronic charges surrounding the nucleus. For many nuclei, the quadrupolar coupling is stronger than other local interactions in NMR, e.g., chemical shift interaction and dipolar coupling. In some cases it can even exceed the Zeeman interaction. The Hamiltonian of quadrupolar coupling in PAS of electronic field gradient (EFG) is written by

$$\hat{H}_Q = \frac{1}{6}\hbar^2\omega_Q[3I_z^2 - \hat{I}(\hat{I}+1) + \eta_Q(I_x^2 - I_y^2)], \tag{1.15}$$

where $\omega_Q = \frac{3e^2qQ}{2I(2I-1)\hbar}$ is the so-called quadrupole frequency, and $\eta_Q = (V_{yy} - V_{xx})/V_{zz}$ (in case of $|V_{zz}| \geq |V_{yy}| \geq |V_{xx}|$) is the asymmetry parameter.

The parameter referred to as the quadrupole coupling constant is often used, given by

$$Q_{cc} = e^2qQ/h \tag{1.16}$$

**1.2 Magic angle spinning (MAS)**

Lacking the averaging effect by fast motion in solution, the anisotropic broadenings in spectra of solid samples cause much lower resolution and sensitivity. The development of MAS has remarkably improved the solid-state NMR spectra by mechanically rotating samples at an axis that is oriented at the magic angle ($\theta_R = 54.74^o$) with respect to the external magnetic field $\vec{B}_0$ (see Figure 1.2). If the spinning speed is larger than the couplings, MAS averages out the anisotropic interactions, leading to notable spectral narrowing.

In case of chemical shift anisotropy, the averaged frequency under fast MAS is written as

$$\omega_{cs} = -\frac{1}{2}\omega_0\Delta\{3\cos^2\beta - 1 + \eta\sin^2\beta\cos 2\phi\}\frac{1}{2}(3\cos^2\theta_R - 1) + \omega_{cs}^{iso} \tag{1.17}$$

www.manaraa.com

Here the angles $\beta$ and $\theta_R$ are indicated in Figure 1.2, and other parameters are predefined in equation (1.10). If the rotor orientation is set at the so-called magic angle, $\theta_R$ = 54.74$^o$, the term $3\cos^2\theta_R - 1 = 0$, and thus the broadening due to chemical shift anisotropy is eliminated.

For dipolar couplings, the geometric factor $(3\cos^2\theta - 1)$ in equations (1.13) and (1.14) can also be averaged, at least partly, assuming that the rate of MAS exceeds the dipolar interaction

$$< 3\cos^2\theta - 1 >= \frac{1}{2}(3\cos^2\theta_R - 1)(3\cos^2\beta - 1) \qquad (1.18)$$

However, in rigid systems the line broadening due to $^1$H-$^1$H homonuclear dipolar couplings cannot be completely eliminated by MAS alone due to its size and homogeneous character. A technique referred to as CRAMPS (combined rotation and multiple-pulse spectroscopy) can be implemented to achieve state-of-the-art resolution in $^1$H (or $^{19}$F) spectra of such systems [10].

*Homogeneous and inhomogeneous line broadening*

Based on its origin, the line broadening can be classified as inhomogeneous or homogeneous (see Figure 1.4). In the case of inhomogeneous broadening, the spectrum is a superposition of independent narrow lines, whose individual Larmor frequencies continuously span a wide spectral range. For example, the inhomogeneity of the external field $\vec{B}_0$ results in position-dependent Larmor frequencies, so the overall lineshape is a sum of contributions from nuclei in different locations in a sample. Other typical examples of inhomogeneous broadening are: chemical shift anisotropy, chemical shift dispersion, and two-spin dipolar coupling. The resonances contributing to the inhomogeneously broadened spectra can be individually observed by using selective excitation. In contrast, in the case of homogenous broadening, the whole spectrum reacts to excitation as an undivided entity.

www.manaraa.com

Such is the case for broadening caused by multi-spin dipolar coupling interactions. In fast MAS, the linewidth of homogeneously broadened $^1$H spectra is roughly inversely proportional to the MAS rate, $\upsilon_R$. That is, homogeneous broadening can be further narrowed by increasing $\upsilon_R$.

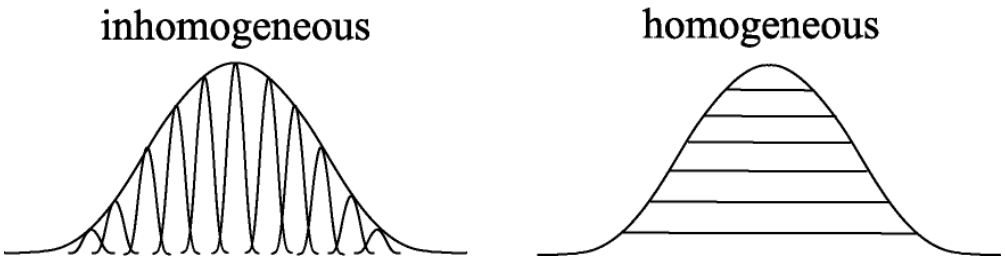


**Figure 1.4**. Visualization of inhomogeneous and homogeneous line broadening.

The recent development of fast MAS (40 - 80 kHz) provided new opportunities for eliminating both homogeneous and inhomogeneous dipolar broadening interactions. In addition, fast MAS provided opportunity to introduce indirect detection and though-bond spectroscopy into solid-state NMR. Until recently, these techniques were rarely implemented due to broad $^1$H linewidth and fast transverse relaxation. In addition, fast MAS offers several other advantages that promote the application of solid-state NMR spectroscopy, including the possibility of probing small samples, using high radiofrequency (RF) power as well as low-power RF decoupling schemes [11], generating side-band free spectra, and utilizing the large spectral width of the indirect dimension in rotor-synchronized experiments.

In the following sections, the indirect detection and though-bond spectroscopy, which are mostly related to our research, are addressed.

### 1.3 Indirect detection of low-γ nuclei

www.manaraa.com

During the last two decades most of heteronuclear shift correlation NMR experiments in solution utilized direct detection of $^{1}$H, whereas the low-$\gamma$ nuclei, such as $^{13}$C or $^{15}$N, were observed indirectly. The detection of $^{1}$H nuclei in the F2 dimension is advantageous due to their high magnetogyric ratio $\gamma$. In solid-state NMR spectroscopy, these so-called indirect detection schemes were impractical, because of the need of using RF irradiation for homonuclear $^{1}$H-$^{1}$H decoupling.

The general expression for the signal-to-noise ratio (S/N) derived from 1D measurements is

$$\frac{S}{N} \propto NT^{-1}B_0^{3/2}\gamma_{exc}\gamma_{obs}^{3/2}W_{obs}^{-1/2}(NS)^{1/2}, \tag{1.19}$$

where $N$ is the number of NMR active spins in the sample, which is related to the amount of molecules in the sample volume and the abundance of the observed spins; $T$ is the temperature of the sample with the surrounding coil; $\gamma_{exc}$ represents magnetogyric ratio of the excited spins, $\gamma_{obs}$ is the magnetogyric ratio of the observed spins, $W_{obs}$ indicates the linewidth of observed spins, and NS denotes the total number of scans in the experiment. The sensitivity scales as $\gamma_{exc}$ due to the larger Boltzmann population difference. The $\gamma_{obs}{}^{3/2}$ term is due to the proportionality between $\gamma_{obs}$ and the nuclear magnetic moment as well as the Larmor frequency (and thus the signal induced in the coil). Regardless of the value of $\gamma$, the S/N ratio depends on $B_0{}^{3/2}$, due to the proportionality between $\gamma$ and $\omega_0$ and between the signal induced in the coil and $B_0{}^{1/2}$.

Take $^{1}$H-$^{13}$C heteronuclear shift correlation as an example to compare the signal-to noise (S/N) ratios of direct detection (DD) and indirect detections (ID). With the same excited spin ($^{1}$H) and different observed spins ($^{13}$C and $^{1}$H, respectively) the sensitivity enhancement factor [12] is given by

www.manaraa.com

$$\xi = \frac{(S/N)_{ID}}{(S/N)_{DD}} \propto (\frac{\gamma_H}{\gamma_C})^{3/2} (\frac{W_C}{W_H})^{1/2} \qquad (1.20)$$

In solution NMR, the lines are naturally narrow, and the enhancement factor of indirect detection depends mainly on the gyromagnetic ratios of the nuclei involved (~8 in the case of $^{1}$H-$^{13}$C and ~30 for $^{1}$H-$^{15}$N). In solids this advantage is diminished due to much broader $^{1}$H lines, unless the strong $^{1}$H homonuclear couplings are reduced by fast MAS. Indeed, the development of indirect detection in solid-state NMR, and the sensitivity enhancements have been obtained in both isotopically enriched samples [5,13] and natural abundant samples [9,14]. Further improvement of sensitivity can be achieved by redesigning the NMR probes to favor observation of $^{1}$H and $^{19}$F nuclei.

### 1.4 Through-bond spectroscopy

Through-bond correlation spectroscopy, which maps out the interactions through chemical bonds by scalar (J) coupling, is one of the key areas of NMR methodology. It is widely used in solution NMR, where a great number of pulse sequences have been developed that rely on polarization transfer between J-coupled homonuclear or heteronuclear spin pairs, e.g., correlation spectroscopy (COSY) and heteronuclear single quantum correlation (HSQC).

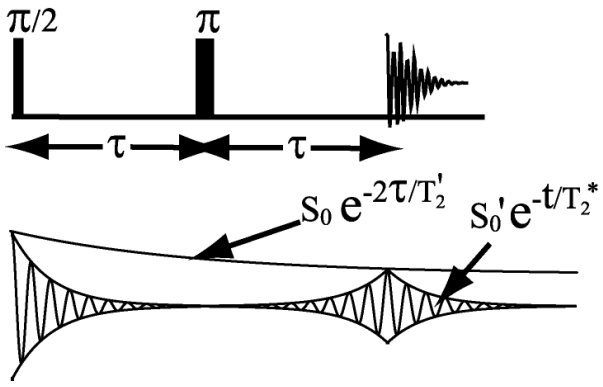


**Figure 1.5**. Definition of $T_2'$ in the spin-echo experiment.

www.manaraa.com

Although the utilization of J coupling has been increasing in solid-state, mainly for spectral editing [15-16] and direct measurement of J values in organic and inorganic materials [17-18], wider application of though-bond spectroscopy in solids was hindered by the fast decay of transverse spin magnetization. However, as mentioned in section 1.2, the homogeneous dipolar interactions can be reduced by increasing the rate of MAS. In other words, the transverse relaxation time $T_2'$ (described in Figure 1.5), which is related to the decay of magnetization due to strong dipolar couplings that is non-refocusable by the spin-echo sequence, can be extended with the help of faster MAS [19].

To explain the effect of $T_2'$ on the magnetization transfer via J coupling, consider as an example a basic through-bond experiment, such as insensitive nuclei enhanced by polarization transfer (INEPT).

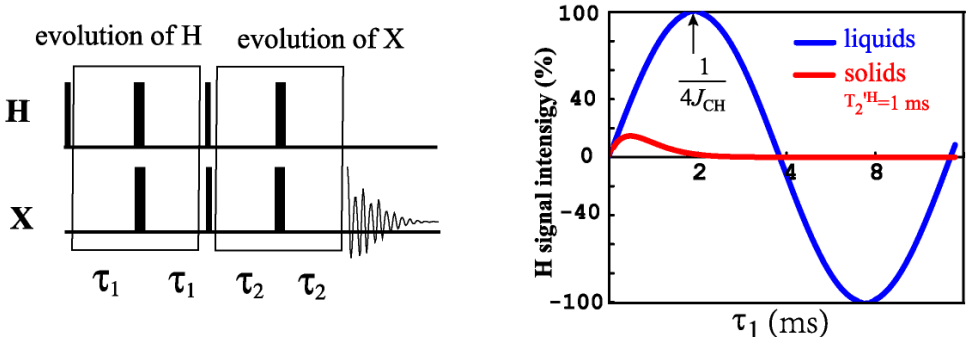


**Figure 1.6**. The pulse sequence of INEPT (left) and the proton evolution curves of typical liquid and solid samples (right). The curves are given by following expression: $\sin(2\pi J_{CH}\tau_1)$ (blue, liquids) and $\sin(2\pi J_{CH}\tau_1)e^{-2\tau_1/T_2'}$ (red, solids).

As indicated in Figure 1.6, in an INEPT experiment, during the first spin-echo sequence the $^1$H nuclei are subject to the transverse relaxation, whereas during the second part of the

www.manaraa.com

sequence the relaxation losses are incurred by the polarized spins, in this case $^{13}C$. The right part of Fig. 1.6 shows the evolution of $^{1}H$ magnetization in a CH pair in liquid (blue) and solid (red) samples. In liquids, fast molecular reorientation essentially eliminates the relaxation losses during the polarization transfer, i.e. the transferred magnetization evolves as $\sin(2\pi J_{CH}\tau_1)$ with typical $J_{CH}$ values being around 130 Hz. In solids, on the other hand, this evolution is attenuated by strong exponential decay, which significantly reduces the efficiency of magnetization transfer. In case of $T_2'$ = 1 ms, at $\tau_1 = 1/4J_{CH}$ (the optimized parameter in solution), the signal intensity in solid drops to only 2 %, and the maximum achievable intensity obtained with this fast decay is less than 20%. Thus, slowing down the transverse relaxation in solids is crucial for improving the efficiency of polarization transfer via J coupling.

Besides fast MAS, an alternative way to increase $T_2'$ is the previously mentioned CRAMPS method. Recently, through-bond spectroscopy assisted by CRAMPS under fast MAS has been successfully implemented on rigid solid samples with natural abundance, e.g., tripeptide *N-formyl*-L-methionyl-L-leucyl-L-phenylalanine (f-MLF-OH) and brown coal [14]. These experiments demonstrate the gradual merging of instrumental and methodological aspects of NMR spectroscopy in solids and solutions.

**1.5 References**

[1] E. M. Purcell, H. C. Torrey and R. V. Pound, Resonance absorption by nuclear magnetic moments in a solid, *Phys.Rev.*, 69 (1946) 37-38.

[2] F. Bloch, W. W. Hansen, and M. E. Packard, Nuclear induction, *Phys.Rev.*, 69 (1946) 127-128.

[3] E.R. Andrew, A. Bradbury and R. G. Eades, Nuclear magnetic resonance spectra from a crystal rotated at high speed, *Nature.*, 182 (1958) 1659.

www.manaraa.com

[4] A. Samoson, T. Tuherm, J. Past, A. Reinhold, T. Anupold and I. Heinmaa, New horizons for Magic-Angle spinning NMR, *Topics Curr. Chem.*, 246 (2004) 15-31.

[5] Y. Ishii and R. Tycko, Sensitivity enhancement in solid state $^{15}$N NMR by indirect detection with high-speed magic angle spinning, *J. Magn. Reson.* 142 (2000) 199-204.

[6] B. Reif, R.G. Griffin, $^{1}$H detected $^{1}$H,$^{15}$N correlation spectroscopy in rotating solids, *J. Magn. Reson.* 160 (2003) 78-83.

[7] J.W. Wiench, C.E. Bronniman, V.S.-Y. Lin, M. Pruski, Chemical shift correlation NMR spectroscopy with indirect detection in fast rotating solids: Studies of organically functionalized mesoporous silicas, *J. Am. Chem. Soc.* 129 (2007) 12076-12077.

[8] D.H. Zhou, G. Shah, M. Cormos, C. Mullen, D. Sandoz, C.M. Rienstra, Proton-detected solid-state NMR spectroscopy of fully protonated proteins at 40 kHz magic-angle-spinning, *J. Am. Chem. Soc.* 129 (2007) 11791-11801.

[9] K. Mao, J.W. Wiench, V.S.-Y. Lin and M. Pruski, Indirectly detected through-bond chemical shift correlation NMR spectroscopy under fast MAS: Studies of organic-inorganic hybrid materials, *J. Magn. Reson.* 196 (2009) 92-95.

[10] B.C. Gerstein, R.G. Pembleton, R.C. Wilson, L.M.J. Ryan, High resolution NMR in randomly oriented solids with homonuclear dipolar broadening: Combined multiple pulse NMR and magic angle spinning, *Chem. Phys.* 66 (1977) 361-362.

[11] M. Ernst, M.A. Meier, T. Tuherm, A. Samoson, B.H. Meier, Low-power high-resolution solid-state NMR of peptides and proteins, *J. Am. Chem. Soc.* 126 (2004) 4764-4765.

[12] Y. Ishii, J. P. Yesionowski, R. Tycko, Sensitivity enhancement in solid-state $^{13}$C NMR of synthetic polymers and biopolymers by $^{1}$H NMR detection with high-speed magic angle spinning, *J. Am. Chem. Soc.* 123 (2001) 2921-2922.

[13] E.K. Paulson, C.R. Morcombe, V. Gaponenko, B. Dancheck, R.A. Byrd, and K.W. Zilm, Sensitive high resolution inverse detection NMR spectroscopy of proteins in the solid state, *J. Am. Chem. Soc.* 125 (2003) 15831-15836.

www.manaraa.com

[14] K. Mao and M. Pruski, Directly and indirectly detected through-bond heteronuclear correlation solid-stat NMR spectroscopy under fast MAS, *J. Magn. Reson.* 201 (2009) 165-174.

[15] N. C. Nielsen, H. Bildsøe, H. J. Jakobsen, O. W. Sørensen, SEMUT spectral editing and determination of radio-frequency field strengths for carbon-13 cross-polarization/magic angle spinning NMR of solids, *J. Magn. Reson.* 79 (1988) 554-560.

[16] D. Sakellariou, A. Lesage, L. Emsley, Spectral Editing in Solid-State NMR Using Scalar Multiple Quantum Filters, *J. Magn. Reson.* 151 (2001) 40-47.

[17] A. Lesage, D. Sakellariou, S. Steuernagel, L. Emsley, Carbon-Proton Chemical Shift Correlation in Solid-State NMR by Through-Bond Multiple-Quantum Spectroscopy, *J. Am. Chem. Soc.* 120 (1998) 13194-13201.

[18] B. Alonso, D. Massiot, Multi-scale NMR characterization of mesostructured materials using $^{1}H$-$^{13}C$ through-bond polarisation transfer, fast MAS, and $^{1}H$ spin diffusion, *J. Magn. Reson.* 163 (2003) 347-352.

[19] B. Elena, A. Lesage, S. Steuernagel, A. Böckmann, L. Emsley, Proton to Carbon-13 INEPT in Solid-State NMR Spectroscopy, *J. Am. Chem. Soc.* 127 (2005) 17296-17302.

www.manaraa.com

# Chapter 2

# Indirectly detected through-bond chemical shift correlation NMR spectroscopy in solids under fast MAS: Studies of organic-inorganic hybrid materials

Published in *J. Magn. Reson.,* 196 (2009) 92-95

Kanmi Mao, Jerzy W. Wiench, Victor S.-Y Lin, and Marek Pruski

## 2.1 Abstract

Indirectly detected, through bond NMR correlation spectra between $^{13}C$ and $^{1}H$ nuclei are reported for the first time in solid state. The capabilities of the new method are demonstrated using naturally abundant organic-inorganic mesoporous hybrid materials. The time performance is significantly better, almost by a factor of 10, than in the corresponding $^{13}C$ detected experiment. The proposed scheme represents a new analytical tool for studying other solid-state systems and the basis for the development of more advanced 2D and 3D correlation methods.

## 2.2 Introduction

The usefulness of solid-state NMR spectroscopy in structural analysis hinges on the availability of high-resolution spectra and good sensitivity. Remarkable advances are currently being made in both these areas due to the development of fast magic angle spinning (MAS) [1,2]. Recent reports have shown the major advantages of using fast MAS in the study of organic-inorganic mesoporous materials [3,4]. Most importantly, MAS at 40 kHz provided a simple and artefact-free way of achieving high $^{1}H$ resolution in these materials without the use of multiple-pulse radiofrequency (RF) irradiation and stroboscopic observation (CRAMPS [5]) [3]. Excellent sensitivity per spin, lack of spinning sidebands and

www.manaraa.com

the possibility of using low-power decoupling schemes [6] have enabled convenient acquisition of highly resolved 2D $^{13}C\{^{1}H\}$ and $^{29}Si\{^{1}H\}$ heteronuclear correlation (HETCOR) NMR spectra. Another consequence of achieving CRAMPS-quality resolution without stroboscopic sampling is the opportunity for sensitivity enhancement by detecting the low-$\gamma$ (X) nuclei indirectly via high-$\gamma$ $^{1}H$ nuclei. Although the maximum gain of $(\gamma_H/\gamma_X)^{3/2}$ is unrealistic in solids, we found the time performance of indirect detection to be better than the standard $^{13}C\{^{1}H\}$ HETCOR experiment by a factor of more than ten. Remarkably, the indirectly detected $^{13}C$-$^{1}H$ HETCOR spectra of samples containing a few μmole of covalently bound functional groups (in the absence of templating molecules) were obtained within minutes or hours without using isotope enrichment [4].

The fast MAS-based HETCOR spectra reported thus far are based on cross polarization (CP), providing through-space correlations via the dipolar interaction. Due to the strength of dipolar coupling (which is on the order of 20 kHz for closely spaced C-H pairs), the CP transfers are fast and efficient. However, they can be affected by molecular motions and are poorly suited for differentiating between short- and long-range correlations. Although the through-bond scalar (*J*) couplings are much weaker (in directly bonded C-H pairs the $^{1}J_{CH}$ values are on the order of 100 Hz), their utilization in solids has become increasingly practical following the progress in MAS technology and RF decoupling methods. The *J* couplings have been successfully exploited in various 1D and 2D experiments, including measurement of *J*-coupling constants [7-9], spectral editing [10-12], and acquisition of homo- and heteronuclear correlation spectra in organic and inorganic materials [13-16].

The heteronuclear *J* correlation sequences reported for solids are based on mixing schemes developed for solution NMR, of which refocused INEPT is the most common. The key to achieving high efficiency in this experiment is to prevent the decoherence of transverse magnetization due to interactions that are non-refocusable by the rotor-synchronized spin-echo sequence under fast MAS. Since transverse relaxation is dominated by the dipolar

www.manaraa.com

couplings, the corresponding $T_2'$ values and the efficiency of INEPT are expected to increase with increasing MAS rate $\nu_R$. In addition to fast MAS, the use of proton homonuclear decoupling can be used to extend the $^1$H coherence lifetimes [17].

Here, we demonstrate that the benefits of fast MAS and polarization transfer via INEPT can be mutually utilized to measure, for the first time, the indirectly detected 2D $^1$H{$^{13}$C} through bond correlation spectra in solids. The new method is used to study mesoporous silica nanoparticles (MSN's) containing the templating molecules or covalently bound surface functional groups under natural abundance.

## 2.3 Experimental

*NMR measurements*

The pulse sequence for the 2D $^1$H{$^{13}$C} INEPT experiment, shown in Figure 2.1b, draws from the previously described CP-based schemes (Figure 2.1a) [4,18]. The experiment uses the tangentially ramped $^{13}$C{$^1$H} CP (or $^{13}$C{$^1$H} INEPT, not shown) to create the initial $^{13}$C magnetization, which then evolves during $t_1$ under the isotropic chemical shift in the presence of low-power decoupling (SPINAL-64 or, as shown in the figure, a single $\pi$ pulse [4]). Following the $t_1$ period, $^{13}$C magnetization is stored along the $B_0$ field, while the residual $^1$H coherence is purged using two long pulses ($\tau_{RR}$ = 40 ms for CTAB and 25 ms for PFP) with orthogonal phases, where the magnitude of RF field at the $^1$H frequency satisfies the rotary resonance recoupling condition $\nu_{RF}^{H} = 0.5\,\nu_R$ [19,20]. Subsequently, the INEPT sequence is applied to transfer $^{13}$C polarization back to $^1$H nuclei. The SPINAL-64 $^{13}$C decoupling is used during the detection period ($t_2$), to eliminate the residual dipolar broadening and the $J$ splitting of $^1$H lines in the $\nu_2$ dimension. The so-called steady duty cycle compensation is implemented (if needed, i.e. when SPINAL-64 $^1$H decoupling is used during $t_1$) [21], along with other previously described measures [4], to minimize the $t_1$-noise. All measurements

www.manaraa.com

were performed on a Varian NMR System 600 spectrometer, equipped with a 1.6-mm triple resonance FastMAS$^{TM}$ probe, using $\nu_R$ = 40 kHz.

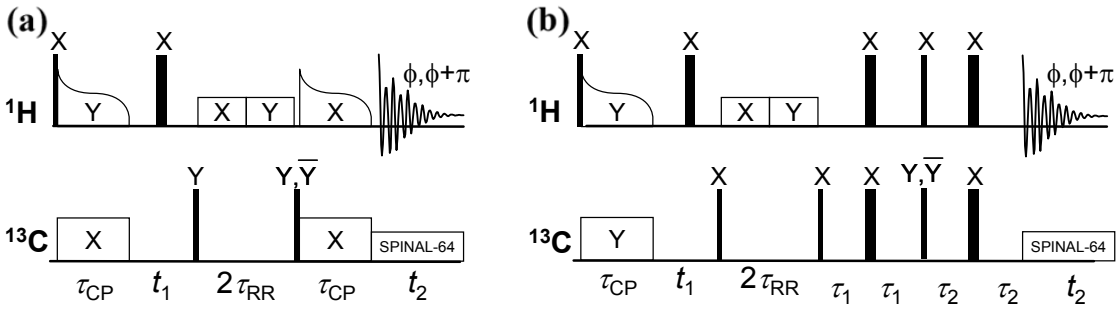


**Figure 2.1**. Pulse sequences for CP-based (a) and INEPT-based (b) $^{1}$H detected HETCOR experiments under fast MAS. Solid rectangles represent $\pi/2$ and $\pi$ pulses. Phase cycling was simplified by the use of direct digital receiver. States-TPPI detection was implemented through appropriate phase switching of the first $\pi/2$ pulse in the $^{13}$C channel.

*Sample preparation*

Two samples were synthesized according to the procedures described in our previous papers: (1) a non-functionalized sample of mesoporous silica containing the surfactant (CTAB), referred to as CTAB-MSN [22], and (2) a sample functionalized via co-condensation with covalently bound pentafluorobenzene groups (-$CH_2$-$CH_2$-$CH_2$-$C_6F_5$), and referred to as PFP-MSN [23]. CTAB was removed from PFP-MSN by acid extraction. Based on the deconvolution of $^{29}$Si MAS spectra, we estimated that 13 ±2 % of silicon atoms in this sample are bound to carbon, which corresponds to the functional group concentration of 1.2 mmol/g. The samples were packed in MAS rotors after exposure to ambient conditions in the laboratory. The static $^{1}$H linewidths were 6 kHz in CTAB-MSN and 12 kHz in PFP-MSN.

**2.4 Results and discussion**

www.manaraa.com

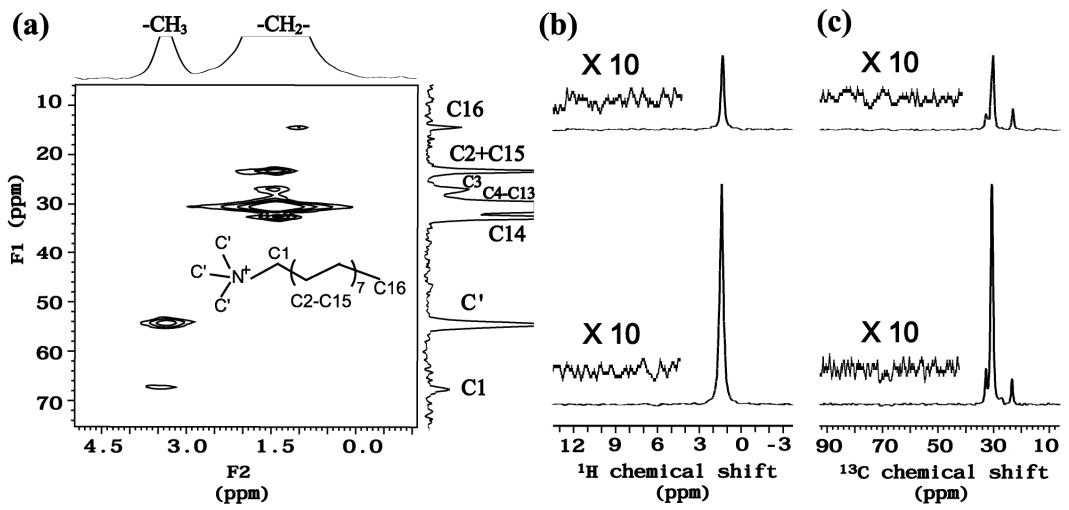


**Figure 2.2**. (a) 2D indirectly detected $^{1}H\{^{13}C\}$ spectrum of CTAB-MSN with INEPT mixing recorded at 14.1 T, using $\nu_R$ = 40 kHz, $\nu_{RF}^{H}$ = 110 kHz during short pulses, $\nu_{RF}^{H}$ = 60 kHz (with tangent ramp) during CP, $\nu_{RF}^{C}$ = 100 kHz during short pulses and CP, $\nu_{RF}^{C}$ = 10 kHz during SPINAL-64 decoupling. The spectrum was acquired in 240 rows, 4 scans per row with $t_1$ increments of 50 $\mu$s, $\tau_{CP}$ = 2.0 ms, $\tau_1$ = 1.1 ms, $\tau_2$ = 1.2 ms, and recycling delay of 1.5 s. Total acquisition time was 50 min. (b), (c) Selected cross-sections along H (b) and C (c) dimensions of spectrum (a) (bottom traces), and of the corresponding C-detected spectrum acquired under the same experimental conditions (top traces).

The 2D $^{1}H\{^{13}C\}$ INEPT spectrum of CTAB-MSN is shown in Figure 2.2a, where the peak assignments are shown based on the NMR spectrum of CTAB in solution. Acquisition of 4 scans per row yielded a signal to noise ratio of ≅ 200 for $^{13}C$ resonance at 30.5 ppm. As demonstrated in Figures 2.2b and 2.2c, the sensitivity is better by a factor of 3 than in the corresponding $^{13}C$ detected spectrum, and as good as in the indirectly detected CP-based spectrum (not shown). 2D CP-based and INEPT-based $^{1}H\{^{13}C\}$ correlation spectra of PFP-MSN are shown in Figures 2.3a and 2.3b. The observed cross-peaks show that the attached functional groups have the structure consistent with the PFP groups shown in Figure 2.3a,

www.manaraa.com

thereby confirming that functionalization of the silica surface has indeed taken place as intended. Also present is a resonance representing the surface methoxy groups. The correlations due to long-range interactions (C2-H1, C2-H3, C3-H2 and C4-H3,) are only observed in Figure 2.3a, which well demonstrates the through-bond filtering capabilities of $^{1}H\{^{13}C\}$ INEPT method. For the most prominent peaks, the CP-based and INEPT-based 2D spectra in Figure 2.3 have similar intensities per scan. We note, however, that spectrum (a) has been acquired using $\tau_{CP}$ = 4.5 ms in order to achieve substantial polarization between weakly coupled nuclei. This condition did not favor the strongly coupled pairs (C1-H1, C2-H2 and C3-H3) whose intensities would have been higher when using $\tau_{CP}$ in the 0.5 ms range. By shortening $\tau_{CP}$ to 50 $\mu$s, the correlations due to weakly coupled spins can be completely eliminated, yielding a spectrum similar to $^{13}C\{^{1}H\}$ INEPT, albeit much less intense.

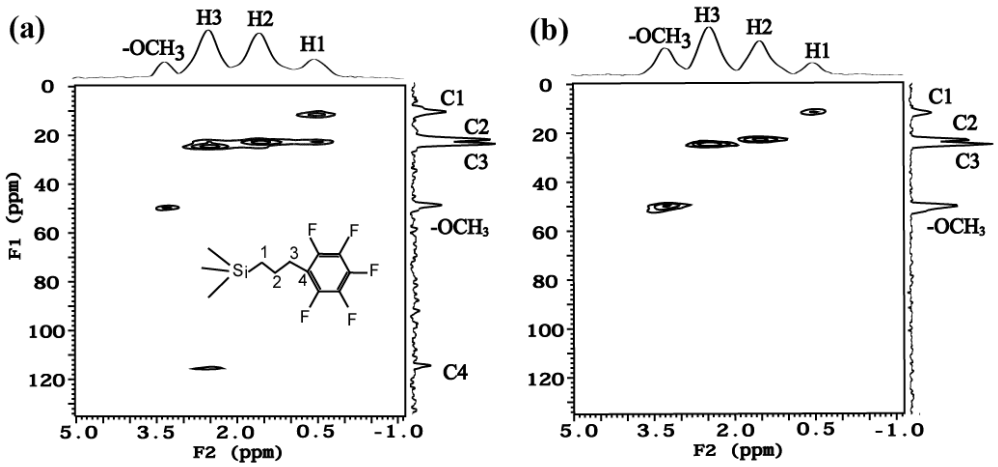


**Figure 2.3**. 2D indirectly detected $^{1}H\{^{13}C\}$ spectra of PFP-MSN with CP (a) and INEPT (b) mixing. The spectra were acquired in 160 rows, with $t_1$ increments of 25 $\mu$s, $\tau_{CP}$ = 4.5 ms, recycling delay of 1 s, 48 (a) and 128 (b) scans per row, $\tau_1$ = 0.6 ms, and $\tau_2$ = 0.8 ms (c). Acquisition times were 4.5 h (a), and 12.5 h (b). Other experimental details are provided in caption to Figure 2.2.

www.manaraa.com

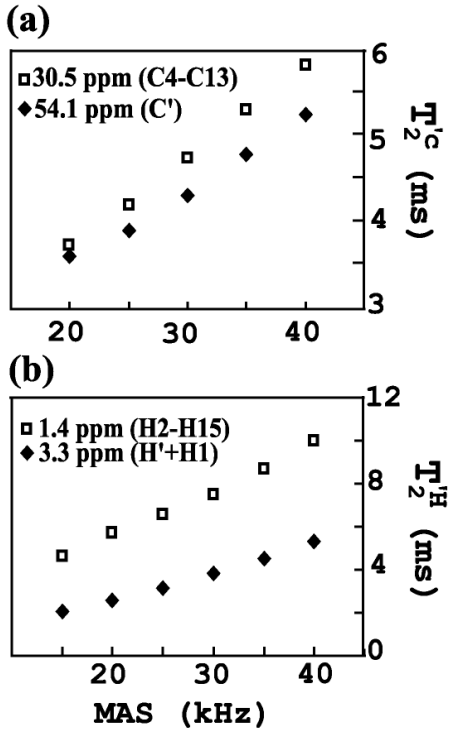


**Figure 2.4**. Measurements of transverse relaxation times $T'^{C}_{2}$ (b) and $T'^{H}_{2}$ (c) during INEPT as a function of $\nu_R$.

While all expected resonances were detected in the MSNs, the relative intensities are influenced by a both CP and INEPT transfers. A detailed analysis of optimization strategies in this and other indirectly detected schemes will be presented separately. Here, we only report on the measurements of transverse relaxation in CTAB, which were made as a function of $\nu_R$ under conditions relevant to INEPT, i.e., using Hahn echo without heteronuclear decoupling. The measurement of $^{13}C$ relaxation ($T'^{C}_{2}$), which in our experiment is operative during $\tau_1$, used $^{13}C\{^{1}H\}$ CP, whereas dephasing of $^{1}H$ (described by $T'^{H}_{2}$ and effective during $\tau_2$) was studied following the $^{1}H\{^{13}C\}$ INEPT. As shown in Figures 2.4a and 2.4b, a linear dependence on $\nu_R$ was found, both for $T'^{H}_{2}$ and $T'^{C}_{2}$, in agreement with an earlier report [16]. This is critically important to our experiment. By reducing $\nu_R$ to 20 kHz, the

www.manaraa.com

sensitivity gain due to indirect detection would be essentially eliminated even if $^{1}H$ resolution remained constant.

## 2.5 Conclusions

We have demonstrated that refocused INEPT can be used with fast MAS to measure through-bond, $^{1}H$ detected HETCOR spectra of naturally abundant organic-inorganic mesoporous solids with excellent sensitivity and resolution. The time performance is significantly better, almost by an order of magnitude, than in the $^{13}C$ detected 2D $^{13}C\{^{1}H\}$ INEPT and matches that of through space, CP based $^{1}H\{^{13}C\}$ method. The proposed scheme represents a new analytical tool for studying other solid-state systems and the basis for the development of more advanced 2D and 3D correlation methods. The development of more efficient homonuclear dipolar decoupling schemes can further improve the efficiency of this technique in strongly coupled spin systems.

## 2.6 Acknowledgment

This research was supported at the Ames Laboratory by the Department of Energy, Basic Energy Sciences, under Contract No. DE-AC02-07CH11358, and ExxonMobil Research and Engineering Corporate Strategic Research.

## 2.7 References

[1] A. Samoson, Extended Magic-Angle Spinning, in: D. M., R. Grant, K. Harris (Eds.), Encyclopedia of nuclear magnetic resonance, John Wiley & Sons: Chichester, Vol. 9, 2002, pp 59-64.

[2] L. S. Du, A. Samoson, T. Tuherm, C. P. Grey, $^{19}F/^{23}Na$ double resonance MAS NMR study of oxygen/fluorine ordering in the oxyfluoride $Na_5W_3O_9F_5$, *Chem. Mater.* 12 (2000) 3611-3616.

www.manaraa.com

[3] J. Trebosc, J. W. Wiench, S. Huh, V. S. Y. Lin, M. Pruski, Studies of organically functionalized mesoporous silicas using heteronuclear solid-state correlation NMR spectroscopy under fast magic angle spinning, *J. Am. Chem. Soc.* 127 (2005) 7587-7593.

[4] J. W. Wiench, C. E. Bronniman, V. S.-Y. Lin, M. Pruski, Chemical shift correlation NMR Spectroscopy with Indirect Detection in Fast Rotating Solids: Studies of Organically Functionalized Mesoporous Silicas, *J. Am. Chem. Soc.* 129 (2007) 12076-12077.

[5] B. C. Gerstein, R. G. Pembleton, R. C. Wilson, L. M. J. Ryan, High resolution NMR in randomly oriented solids with homonuclear dipolar broadening: Combined multiple pulse NMR and magic angle spinning, *Chem. Phys.* 66 (1977) 361-362.

[6] M. Ernst, A. Samoson, B. H. Meier, Low-power decoupling in fast magic-angle spinning NMR, *Chem. Phys. Lett.* 348 (2001) 293-302.

[7] K. W. Zilm, D. M. Grant, High-resolution NMR spectra with J couplings in solids, *J. Magn. Reson.* 48 (1982) 524-526.

[8] H.-M. Kao, C. P. Grey, INEPT experiments involving quadrupolar nuclei in solids, *J. Magn. Reson.* 133 (1998) 313-323.

[9] S. P. Brown, M. Perez-Torralba, D. Sanz, R. M. Claramunt, L. Emsley, The direct detection of a hydrogen bond in the solid state by NMR through the observation of a hydrogen-bond mediated $^{15}N$-$^{15}N$ *J* coupling, *J. Am. Chem. Soc.* 124 (2002) 1152-1153.

[10] N. C. Nielsen, H. Bildsøe, H. J. Jakobsen, O. W. Sørensen, SEMUT spectral editing and determination of radio-frequency field strengths for carbon-13 cross-polarization/magic angle spinning NMR of solids, *J. Magn. Reson.* 79 (1988) 554-560.

[11] T. Terao, H. Miura, A. Saika, Simplification and assignment of carbon-13 spectra by using J-resolved NMR spectroscopy in solids, *J. Am. Chem. Soc.* 104 (1982) 5228-5229.

[12] D. Sakellariou, A. Lesage, L. Emsley, Spectral editing in solid-state NMR using scalar multiple quantum filters, *J. Magn. Reson.* 151 (2001) 40-47.

www.manaraa.com

[13] C. A. Fyfe, H. Meyer zu Altenschildesche, K. C. Wong-Moon, H. Grondey, J. M. Chezeau, 1D and 2D solid state NMR investigations of the framework structure of as-synthesized AlPO4-14, *Solid State Nucl. Magn. Reson.* 9 (1997) 97-106.

[14] J. W. Wiench, M. Pruski, Probing through bond connectivities with MQMAS NMR, *Solid State Nucl. Magn. Reson.* 26 (2004) 51-55.

[15] A. Lesage, D. Sakellariou, S. Steuernagel, L. Emsley, Carbon-proton chemical shift correlation in solid-state NMR by through-bond multiple-quantum spectroscopy, *J. Am. Chem. Soc.* 120 (1998) 13194-13201.

[16] B. Alonso, D. Massiot, Multi-scale NMR characterization of mesostructured materials using $^{1}H$-$^{13}C$ through-bond polarisation transfer, fast MAS, and $^{1}H$ spin diffusion, *J. Magn. Reson.* 163 (2003) 347-352.

[17] B. Elena, A. Lesage, S. Steuernagel, A. Böckmann, L. Emsley, Proton to carbon-13 INEPT in solid-state NMR Spectroscopy, *J. Am. Chem. Soc.* 127 (2005) 17296-17302.

[18] Y. Ishii, R. Tycko, Sensitivity enhancement in solid state $^{15}N$ NMR by indirect detection with high-speed magic angle spinning, *J. Magn. Reson.* 142 (2000) 199-204.

[19] Y. Ishii, J. P. Yesionowski, R. Tycko, Sensitivity enhancement in solid-state $^{13}C$ NMR of synthetic polymers and biopolymers by $^{1}H$ NMR detection with high-speed magic angle spinning, *J. Am. Chem. Soc.* 123 (2001) 2921-2922.

[20] T. G. Oas, R. G. Griffin, M. H. Levitt, Rotary resonance recoupling of dipolar interactions in solid-state nuclear magnetic resonance spectroscopy, *J. Chem. Phys.* 89 (1988) 692-695.

[21] C. R. Morcombe, E. K. Paulson, V. Gaponenko, R. A. Byrd, K. W. Zilm, $^{1}H$-$^{15}N$ correlation spectroscopy of nanocrystalline proteins, *J. Biomol. NMR* 31 (2005) 217-230.

[22] S. Huh, J. W. Wiench, J.-C. Yoo, M. Pruski, V. S.-Y. Lin, Organic functionalization and morphology control of mesoporous silicas via a co-condensation synthesis method, *Chem. Mater.* 15 (2003) 4247-4256.

www.manaraa.com

[23] R. Kumar, H. T. Chen, J. L. V. Escoto, V. S.-Y. Lin, M., Pruski, Template removal and thermal stability of organically functionalized mesoporous silica nanoparticles, *Chem. Mater.* 18 (2006) 4319-4327.

www.manaraa.com

# Chapter 3

# Directly and indirectly detected through-bond heteronuclear correlation solid-state NMR spectroscopy under fast MAS

Published in *J. Magn. Reson.,* 201 (2009) 165-174

Kanmi Mao and Marek Pruski

## 3.1 Abstract

Two-dimensional through-bond $^{1}H\{^{13}C\}$ solid-state NMR experiments utilizing fast magic angle spinning (MAS) and homonuclear multipulse $^{1}H$ decoupling are presented. Remarkable efficiency of polarization transfer can be achieved at MAS rates exceeding 40 kHz, which is instrumental in these measurements. Schemes utilizing direct and indirect detection of heteronuclei are compared in terms of resolution and sensitivity. A simple procedure for optimization of $^{1}H$ homonuclear decoupling sequences under these conditions is proposed. The capabilities of these techniques were confirmed on two naturally abundant solids, tripeptide *N-formyl*-L-methionyl-L-leucyl-L-phenylalanine (f-MLF-OH) and brown coal.

## 3.2 Introduction

Astounding advances are currently being made in solid-state NMR spectroscopy following the development of magic angle spinning (MAS) at rates approaching 70 kHz [1,2]. Recent reports have highlighted several advantages of fast MAS probes, including their excellent sensitivity per spin and efficient cross-polarization (CP) transfer [3,4], the possibility of generating very high radiofrequency (RF) magnetic fields, and the possibility of using low-power RF schemes during preparation, mixing and decoupling periods [5]. In addition, fast MAS affords increased frequency range of the indirect dimension in rotor-synchronized experiments and eliminates the spinning sidebands at

www.manaraa.com

high magnetic fields or in the presence of large chemical shifts anisotropies (CSAs). Most importantly, it helps to reduce or, in some cases, eliminate the strong homonuclear dipolar couplings between high-$\gamma$ nuclei ($^{1}$H and $^{19}$F). Indeed, fast MAS by itself enabled the acquisition of directly detected (also referred to as X-detected or X{$^{1}$H}) and indirectly detected ($^{1}$H-detected or $^{1}$H{X}) multi-dimensional heteronuclear correlation (HETCOR) NMR spectra of organic materials in which $^{1}$H spin systems were isotopically diluted, exhibited some degree of motional narrowing, or were fully coupled [4,6-10]. In our studies, MAS at 40 kHz was used to achieve high $^{1}$H resolution in mesoporous organic-inorganic hybrid materials [4]. The CRAMPS-quality resolution was attainable in such systems by MAS alone because the local molecular dynamics limited the $^{1}$H linewidth to less than half of the static value. Subsequently, it became possible to enhance the sensitivity of through-space (i.e., using CP) two-dimensional (2D) HETCOR experiments by detecting the low-$\gamma$ (X) nuclei indirectly via high-$\gamma$ $^{1}$H nuclei [8]. In the case of $^{1}$H-detected HETCOR experiments, the sensitivity of indirect detection is typically several times better than that of the standard X{$^{1}$H} method [6-10].

Most recently, it has been demonstrated that fast MAS is fully compatible with homonuclear $^{1}$H decoupling using RF pulse sequences, either previously known yet deemed relevant only under MAS rates below 25 kHz, or newly designed [11,12]. Under optimal experimental conditions the resolution of $^{1}$H spectra obtained under MAS at 40 to 70 kHz turned out to be comparable to or better than that obtained in previous state-of-the-art CRAMPS experiments [11]. Thus, fast MAS also offers new opportunities for through-bond heteronuclear spectroscopy, e.g. using pulse sequences similar to heteronuclear single quantum correlation (HSQC) experiments in solution NMR. The utility of using $^{1}$H-$^{1}$H homonuclear decoupling during INEPT in $^{13}$C-detected HETCOR experiments at a lower MAS rate (22 kHz) has been already demonstrated [13]. Indeed, decoupling using so-called “mind-boggling optimization” (DUMBO) during INEPT

www.manaraa.com

tripled the sensitivity in $^{13}C$ labelled L-isoleucine. The first $^{1}H$-detected, INEPT based HETCOR spectra in weakly coupled spin systems have been reported, as well [14]. Fast MAS was instrumental in improving the efficiency of the INEPT transfer because it reduced the magnetization losses due to transverse relaxation.

Herein, we seek to maximize the efficiency of INEPT in HSQC-type experiments in rigid solids by combining $^{1}H$-$^{1}H$ RF decoupling with MAS at $\nu_R \geq 40$ kHz and investigate the sensitivity benefit of indirect detection. The choice of $^{1}H$-$^{1}H$ decoupling method during INEPT is not obvious, because the effectiveness of polarization transfer depends on the decoupling efficiency as well as the scaling factor. We provide a comprehensive analysis of the performance of several decoupling schemes ( $PMLG5^{\bar{x}}_{m}$, $PMLG5^{\bar{x}x}_{mm}$ and SAM3) during the INEPT transfer, and propose a simple optimization scheme for such experiments. The merit of the indirect approach ($^{1}H\{^{13}C\}$) is gauged against the results of a $^{13}C\{^{1}H\}$ HETCOR experiment in which RF $^{1}H$-$^{1}H$ decoupling is also applied during $^{1}H$ evolution. The exciting capabilities of directly and indirectly detected through-bond HETCOR NMR under fast MAS are illustrated on two naturally abundant solids, tripeptide *N-formyl*-L-methionyl-L-leucyl-L-phenylalanine (f-MLF-OH) and brown coal, one well ordered and the other highly disordered.

### 3.3 Background and experimental procedure

*$^{1}H$ decoupling under fast MAS*

Traditionally, high-resolution $^{1}H$ experiments were performed by combining rotation and multiple-pulse sequences (CRAMPS) operated under the quasi-static condition $\tau_c << \tau_R$, where $\tau_c = (\nu_c)^{-1}$ describes the cycle time of the pulse sequence which should be short compared to $\tau_R = (\nu_R)^{-1}$, and it is assumed that $\nu_c$ exceeds the strength of the homogeneous broadening to be removed [15,16]. The development of high-field magnets and probes capable of MAS at rates of up to 25 kHz (now regarded as moderate) was

www.manaraa.com

followed by the implementation of modified CRAMPS strategies, as thoroughly reviewed by Vega et al. [17]. Several decoupling techniques held promise for successful performance at even higher MAS speeds. These included PMLG and DUMBO [18], which can be used both in windowless and windowed schemes without rotor synchronization. The recently introduced symmetry-based rotor-synchronized sequences $CN_n^{\nu}$, $RN_n^{\nu}$ and $ZN_n^{\nu}$ are also unrestricted by quasi-static approximation [12,19,20].

The PMLG sequence [21], which can be viewed as an on-resonance variant of the frequency-switched Lee-Goldburg (FSLG) experiment [22], suppresses the zero- and first-order terms in the average dipolar Hamiltonian. The basic version consists of two building blocks, each composed of a series of *n* pulses with sequentially advanced phases. It has been denoted as $\mathrm{PMLG}n_R^{\Phi}$ [23], where $\Phi$ is the initial phase of the first block and *R* specifies the direction of phase rotation in the *xy* plane, with *R* = *m* for clockwise and *R* = *p* for counter clockwise rotation. This sequence proved easy to implement and yielded good resolution for *n* = 3, 5, and 9, although line broadening and RF-rotor frequency lines appeared at certain combinations of $\nu_c$, $\nu_R$ and frequency offset values [24,25]. Windowed PMLG sequences (*w*PMLG) soon followed, providing opportunities for measuring 2D $^1$H-$^1$H and indirectly detected $^1$H{$^{13}$C} spectra [26]. The theoretical analysis of RF pulse imperfections led to the idea of using RF irradiation parameters (RF power and frequency offset) to obtain a $w\,\mathrm{PMLG}n_R^{\Phi}$ sequence with an effective field along the *z* direction. This so called *z*-rotation yielded spectra with improved resolution and fewer artifacts [27,28]. Subsequently, the supercycled sequence $\mathrm{PMLG}n_R^{\Phi}$ was introduced with $\Phi = \bar{\phi}\phi$ and *R* = *mm*, i.e., composed of two blocks $\mathrm{PMLG}n_m^{\bar{\phi}}$ and $\mathrm{PMLG}n_m^{\phi}$, which relaxed the offset dependencies of the line-narrowing efficiency and the *z*-rotation (and thus the scaling factor which, however, is considerably reduced in the supercycled experiment) [23]. In all of these studies the condition $\nu_c > \nu_R$ was assumed and deemed

www.manaraa.com

necessary to achieve high resolution, provided that the periodicities associated with RF irradiation and MAS did not interfere; i.e., the condition $a\,\nu_R + b\,\nu_c = 0$ with $a$ and $b$ being small integers, was to be avoided. Most recently, however, it has been demonstrated that $w\text{PMLG5}^{\bar{x}x}_{mm}$ (as well as $w$DUMBO) can perform comparably or better when applied at the highest available $\nu_R$ frequencies (up to 65 kHz), even under the condition $\nu_c < \nu_R$, as long as $|a/b|$ ratios are not equal to 1/2, 2/3, 1/3, etc. [11].

The family of rotor-synchronized SAM pulse sequences was recently introduced to achieve efficient homonuclear $^1$H decoupling under very fast MAS by using smooth cosine modulation of the RF magnetic field amplitude [12]. We chose the SAM3 version of the sequence, with the modulation frequency $\nu_c = 3\,\nu_R$, because it does not reintroduce the heteronuclear dipolar and CSA interactions. It proved easy to optimize and tolerant of RF inhomogeneity, which made it potentially useful for our application.

Here, we tested the utility of PMLG and SAM3 decoupling during the INEPT transfer, although DUMBO and symmetry-based methods can be applied, as well. We were primarily concerned with slowing down the decoherence of the transverse magnetizations ($T_2'$ relaxation) of $^1$H and $^{13}$C nuclei during INEPT and less so with the minimization of artifacts such as zero peak, image peaks and RF-rotor frequency lines. Note, however, that the efficacy of these sequences in our experiments depends not only on their ability to slow down the $T_2'$ relaxation, but also on the scaling factors, which determine the effective $J$ coupling and the optimum duration of the polarization transfer.

*Pulse sequences and optimization of homonuclear decoupling*

The polarization transfer through chemical bond used here during mixing is based on a refocused INEPT (INEPTR) pulse sequence, which employs two pairs of rotor-synchronized delays. First, the antiphase proton magnetization is created during time delay $2\tau_1 \cong (2J_{CH})^{-1}$. A second pair of delays of similar duration $\tau_2$ is used to refocus this

www.manaraa.com

magnetization into an in-phase signal. Note that the relaxation losses during INEPT are attributable to the polarizing nuclei during $\tau_1$ and to those being polarized during $\tau_2$. The transverse relaxation during $\tau_1$ and $\tau_2$ is mainly due to $^1$H-$^1$H dipolar interaction, which we strive to overcome by using the combination of fast MAS and multiple-pulse sequences. The decoupling efficiency during INEPT can be conveniently assessed by measuring the $^1$H (or $^{13}$C) signal intensity versus $\tau$ in a simple spin-echo experiment shown in Figure 3.1a, using the SAM3, PMLG5$^{\bar{x}}_{m}$ and PMLG5$^{\bar{x}x}_{mm}$ decoupling sequences depicted in Figure 3.1d. The $^1$H measurements utilized direct polarization whereas $^{13}$C data were measured following the $^{13}$C{$^1$H} CP. The resulting spectra were used to evaluate the $T'^{H}_{2}$ and $T'^{C}_{2}$ relaxation times for all resolved proton and carbon sites in the f-MLF-OH tripeptide studied in this work.

The pulse sequence for the 2D HETCOR experiment with indirect detection of $^{13}$C is shown in Figure 3.1b. This sequence uses tangent $^{13}$C{$^1$H} CP transfer, followed by $t_1$ evolution of $^{13}$C magnetization, which is then stored along the $B_0$ field and transferred back to $^1$H nuclei via INEPT [14]. The $t_1$-noise was minimized using the duty compensation of the RF power and by purging the $^1$H magnetization during the $2\tau_{RR}$ period, as described earlier [8,29,30]. Figure 3.1c depicts the corresponding $^{13}$C-detected HETCOR scheme, which follows that proposed by Emsley et al. [13], but is operated here at high MAS rate [11]. Based on the analysis of relaxation data, only the PMLG5$^{\bar{x}}_{m}$ scheme was used during INEPTR in 2D experiments (i.e., during $\tau_1$ and $\tau_2$ in Figure 3.1b and c). Both PMLG5$^{\bar{x}}_{m}$ and PMLG5$^{\bar{x}x}_{mm}$ sequences were tested during the $t_1$ evolution of the $^{13}$C-detected 2D experiment (Figure 3.1c). SPINAL-64 heteronuclear decoupling is used during $t_1$ and $t_2$ periods, as appropriate [31]. In experiments performed under fast MAS ($\nu_R \geq 41.666$ kHz), a low RF magnetic field of $\sim\nu_R/4$ (~11 kHz in our experiments) was

www.manaraa.com

used during heteronuclear decoupling because it was as effective as a high RF magnetic field of ~100 kHz at $\nu_R$ = 20.833 kHz [4,5,32].

All experiments were carried out at 14.1 T on a Varian NMR System 600 spectrometer, using a FastMAS$^{TM}$ probe operated at $\nu_R$ = 41.666 kHz and 20.833 kHz. Additional experimental parameters are given in figure captions and table footnotes, using the following symbols: $\nu_{RF}^{X}$ denotes the magnitude of the RF magnetic field applied to X spins, $\tau_{CP}$ the CP time, $\tau_{RD}$ the recycle delay, $\tau_{RR}$ the rotary resonance recoupling time, $\Delta t_1$ the increment of $t_1$ during 2D acquisition, NS the number of scans, and AT the total acquisition time of a 2D spectrum. The $^1$H and $^{13}$C chemical shifts are reported using the $\delta$ scale and are referenced to TMS at 0 ppm.

The introduction of homonuclear decoupling schemes into the 2D sequences in Figure 3.1 makes them appear complex to set up and optimize. However, we were able to maximize the performance of these sequences very simply by minimizing the signal loss due to $T_2'^{H}$ transverse relaxation in the spin-echo experiment shown in Figure 3.1a. The experimental procedure involves the use of a single delay $\tau$, and within a few minutes reliably provides the best choices for the pulse length, the RF power level, and the frequency offset. Because of the general relevance of this optimization to high-resolution $^1$H spectroscopy, we will detail it separately in a forthcoming publication.

www.manaraa.com

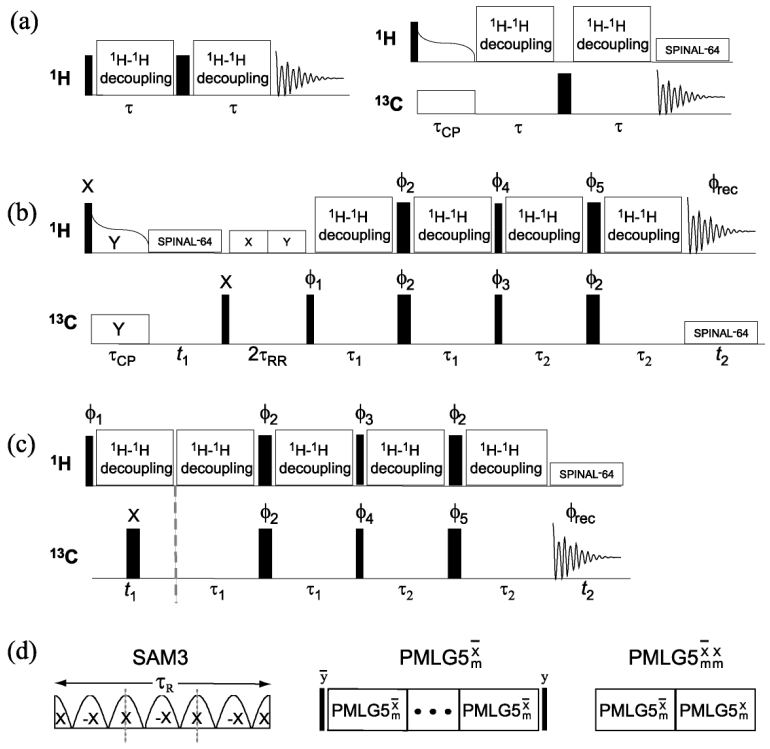


**Fig. 3.1**. Pulse sequences for $^{1}$H and $^{13}$C spin-echo (a), $^{1}$H-detected through-bond HETCOR (b), and $^{13}$C-detected through-bond HETCOR (c) experiments under fast MAS. Also shown are three RF $^{1}$H homonuclear decoupling schemes (SAM3, PMLG5$^{\bar{x}}_{m}$ and PMLG5$^{\bar{x}x}_{mm}$) tested in these experiments (d). Note that in experiments involving PMLG5$^{\bar{x}}_{m}$ additional pulses were used in the before and after each decoupling pulse block to rotate $^{1}$H magnetization from and into the *xy* plane. The effective field produced by the PMLG5$^{\bar{x}}_{m}$ sequence is almost parallel to the *z* axis, which leads to a broad-banded *z*-rotation of the magnetization and eliminates the need for preparatory pulses [23]. Solid rectangles represent π/2 and π pulses. The following phases were used in experiments (b) and (c): $\phi_1 = \{8x, 8(-x)\}$, $\phi_2 = 8\{x, -x\}$, $\phi_3 = 4\{y, y, -y, -y\}$, $\phi_4 = \{4x, 4y, 4(-x), 4(-y)\}$, $\phi_5 = 2\{x, -x, x, -x, y, -y, y, -y\}$, $\phi_{rec} = 2\{x, x, -x, -x, y, y, -y, -y\}$. States-TPPI detection was implemented in 2D experiments through appropriate phase switching of the first π/2 pulse in the $^{13}$C channel. The SAM3 and PMLG sequences followed the recipes given in [12] and [23], respectively.

www.manaraa.com

*Samples*

A common peptide and brown coal were chosen to demonstrate the applications of through-bond correlation methods. The solvent-free, naturally abundant tripeptide f-MLF-OH was purchased from Sigma-Aldrich. The f-MLF-OH structure features well resolved CH, $CH_2$, $CH_3$ and quaternary carbon sites, which exhibit a full range of $^{13}C$-$^{1}H$ couplings, from motionally narrowed to those typical of a fully rigid crystal lattice. The brown coal, originating from the former Cospuden coal mine near Leipzig (Germany), is chemically heterogeneous, which precludes the observation of sharp resonances in $^{1}H$ and $^{13}C$ NMR. Each sample was loaded into the MAS rotor under ambient conditions and studied at room temperature without any treatment.

## 3.4 Results and discussion

*$T_2'$ relaxation*

The $T_2'^{H}$ and $T_2'^{C}$ relaxation times were measured for f-MLF-OH using the spin-echo sequences shown in Figure 3.1a. The data obtained under MAS ($\nu_R$ = 41.667 kHz) and MAS with homonuclear decoupling (SAM3, PMLG5$^{\bar{x}}_{m}$ or PMLG5$^{\bar{x}\bar{x}}_{mm}$) are shown in Tables 3.1 and 3.2. Also shown are the relaxation data measured under PMLG5$^{\bar{x}}_{m}$ and PMLG5$^{\bar{x}\bar{x}}_{mm}$ decoupling with slower MAS ($\nu_R$ = 20.833 kHz). The relaxation times for individual sites were evaluated after acquiring spectra for 20 rotor-synchronized values of $\tau$, as explained in the footnotes to the tables. Most of the carbon sites in f-MLF-OH could be easily resolved and assigned following an earlier report of Griffin et al. [33] (Figure 3.2). The site-specific $T_2'^{C}$ values were not measured for $F^{\gamma}$ and carbonyl carbons (L', F' and M') because they were of no interest to us, or for the pairs of carbons in the phenyl ring ($F^{\delta 1,2}$ and $F^{\varepsilon 1,2}$) because they remained broad and unresolved due to the interference of the ring

www.manaraa.com

dynamics (see below) with heteronuclear decoupling. In the case of $T'^{H}_{2}$ measurements, the RF homonuclear decoupling was not applied during $^{1}$H detection, making resolution insufficient to resolve all proton sites (at $\nu_R$ = 41.667 kHz the resolution was comparable to that in Figure 3.3b). Therefore, the $^{1}$H spectra were deconvoluted into four groups of resonances centered at 0.8 ppm (representing $CH_3$ groups), 2.0 ppm (predominantly $CH_2$), 6.2 ppm (CH) and 8.8 ppm (formyl H), for which only the average values of $T'^{H}_{2}$ were evaluated by fitting the data with a single exponential decay. The performance of $^{1}$H decoupling sequences was optimized as described in section 2.2. Notably, under the PMLG sequences the best $T'^{H}_{2}$ and $T'^{C}_{2}$ values were obtained when $\nu_R$ was smaller than $\nu_c$ (e.g. in the case of PMLG5$^{\bar{x}x}_{mm}$, $\nu_R/\nu_c \approx 0.62$ for $\nu_R$ = 41.667 kHz and $\nu_R/\nu_c \approx 0.56$ for $\nu_R$ = 20.833 kHz; see footnote (a) to Tables 3.1 and 3.2). Although similar $T'^{H}_{2}$ and $T'^{C}_{2}$ results could be reached under the condition $\nu_R > \nu_c$ (by adjusting the RF power level such that the two frequencies did not interfere), the resulting scaling factors were considerably reduced.

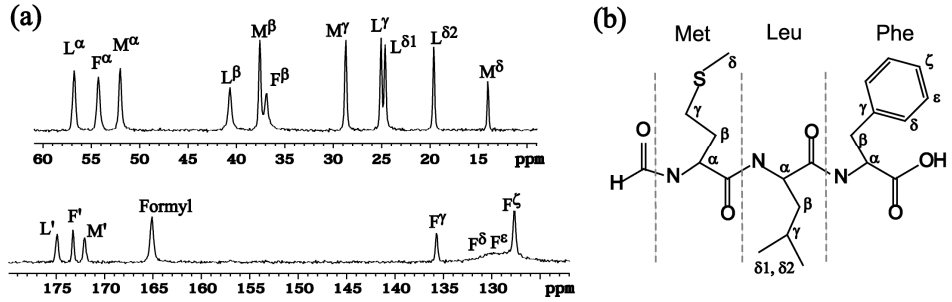


**Fig. 3.2**. $^{13}$C CPMAS spectrum (a) and molecular structure of f-MLF-OH (b). The spectrum was measured at room temperature using $\nu_R$ = 41.667 kHz, $\tau_{CP}$ = 0.3 ms, $\nu^{H}_{RF}$ = 62 kHz during CP (tangent), $\nu^{C}_{RF}$ = 104 kHz during CP, $\nu^{H}_{RF}$ = 11 kHz during SPINAL-64 decoupling, and $\tau_{RD}$ = 2 s. The assignments are made following reference 41.

www.manaraa.com

To facilitate the ensuing discussion, we note that in our measurements the $^{1}$H and $^{13}$C relaxation is influenced mainly by the residual homogeneous interactions that are non-refocusable by the rotor-synchronized π pulses under fast MAS and RF $^{1}$H homonuclear decoupling. The refocusable (inhomogeneous) interactions include chemical shift anisotropy (CSA) and heteronuclear couplings. The $^{1}$H and $^{13}$C linewidths can be additionally broadened due to disorder and/or anisotropic bulk magnetic susceptibility [34-36]. Notwithstanding the simplicity of the spin-echo sequence, the measured relaxation times are difficult to rationalize because of the complexity of the spin dynamics in extended networks of spins involving strongly interacting $^{1}$H nuclei under MAS and RF decoupling, where the effective couplings depend on the orientation of the local networks with respect to the magnetic field. Numerical *ab initio* simulations reported recently by Zorin et al. [37] allowed for comprehensive analysis of $^{1}$H linewidths in model systems with different dimensionalities and dynamics as a function of $\nu_R$, in the absence of RF decoupling. In agreement with earlier predictions and measurements [38,39], the intrinsic homogeneous component of $^{1}$H linewidth, as measured in the spin-echo experiment under MAS, was found to scale as $(\nu_R)^{-1}$, with the proportionality factor depending on the networks' dimensionality, geometry and dynamics [37]. The limit of homogeneous (spin-echo) linewidth at infinite $\nu_R$ is very low, because it is set by scalar $J_{HH}$ couplings (which are typically on the order of 10 Hz and are invariant during this experiment) and the spin-spin relaxation $T_2$. Even when using MAS at the highest currently available rates, the potential exists to increase the efficiency of homonuclear decoupling with RF pulse sequences. By making the heteronuclear dipolar interaction with the dilute ($^{13}$C) nuclei inhomogeneous, efficient homonuclear decoupling should have a similar effect on $T_2'^{C}$ processes.

www.manaraa.com

Table 3.1. Measurements of transverse relaxation time $T_2'^H$ in f-MLF-OH under MAS at 41.667 kHz, and MAS at 41.667 or 20.833 kHz with homonuclear RF pulse decoupling.

| Functional group | | $\delta_{1H}$ [ppm] | $T_2'^H$ [ms][a] | | | | | |
|---|---|---|---|---|---|---|---|---|
| | | | MAS only $s_f = 1.0$ | SAM3 $s_f = 0.71$ | $PMLG5_m^{\bar{x}}$ [b] $s_f = 0.71$ (*0.49*) | | $PMLG5_{mm}^{\bar{x}x}$ [b] $s_f = 0.36$ (*0.29*) | |
| CH | $M^\alpha$, $L^\alpha$, $F^\alpha$, $F^\delta$, $F^\varepsilon$, $F^\zeta$ | 6.2 | 0.6 | 2.4 | 3.5 | *5.2* | 5.1 | *5.9* |

[a] Each measurement consisted of 20 data points, which were fitted with a single exponential decay. The following rotor-synchronized increments of $\tau$ were used: $\Delta\tau = 24$ us (MAS), $\Delta\tau = 120$ us (SAM3), and $\Delta\tau = 240$ us ($PMLG5_m^{\bar{x}}$ and $PMLG5_{mm}^{\bar{x}x}$). The data were acquired with $\tau_{RD} = 2$ s using the RF magnetic fields $\nu_{RF}^H = 150$ kHz during $\pi/2$, $\pi$ and PMLG pulses, and $\nu_{RF}^H = 135$ kHz during the SAM3 sequence. In the $PMLG5_m^{\bar{x}}$ experiment, additional short pulses (1.2 μs, $\nu_{RF}^H = 150$ kHz) were used in the $^1$H channel before and after each decoupling block to rotate $^1$H magnetization from and into the *xy* plane. At $\nu_R = 41.667$ kHz, the optimized homonuclear decoupling conditions were as follows: during SAM3, the cosine line shape was defined by 120 segments of 0.2 us duration and total duration $\tau_c = 24$ us; during $PMLG5_m^{\bar{x}}$ and $PMLG5_{mm}^{\bar{x}x}$ decoupling, we used $\tau_{PMLG} = 0.75$ us ($\tau_c = 7.5$ us and 15 us, respectively). At $\nu_R = 20.833$ kHz, only the $PMLG5_m^{\bar{x}}$ and $PMLG5_{mm}^{\bar{x}x}$ decouplings were tested, which worked best with $\tau_{PMLG} = 1.35$ us ($\tau_c = 13.5$ and 27 us, respectively).

[b] Data obtained with $\nu_R = 20.833$ kHz are given in italics.

[c] $M^\delta$ and $L^\gamma$ are $CH_3$ and CH carbons, respectively.

[d] Resonances at 0.8 and 2.0 ppm were unresolved at $\nu_R = 20.833$ kHz.

www.manaraa.com

Table 3.1. (continued)

| Functional group | | $\delta_{1H}$ [ppm] | $T'^{H}_{2}$ [ms][a] | | | | | |
|---|---|---|---|---|---|---|---|---|
| | | | MAS only $s_f = 1.0$ | SAM3 $s_f = 0.71$ | PMLG5$^{\bar{x}}_{m}$ [b] $s_f = 0.71$ (*0.49*) | | PMLG5$^{\bar{x}\bar{x}}_{mm}$ [b] $s_f = 0.36$ (*0.29*) | |
| CH | Formyl | 8.8 | 1.1 | 5.7 | 6.2 | *9.6* | 12.1 | *8.2* |
| $CH_2$[c] | $M^{\delta}$, $M^{\gamma}$, $M^{\beta}$, $L^{\beta}$, $L^{\gamma}$, $F^{\beta}$ | 2.0 | 0.6 | 3.8 | 5.3 | *11.4*[d] | 10.3 | *15.2*[d] |
| $CH_3$ | $L^{\delta 1}$, $L^{\delta 2}$ | 0.8 | 0.4 | 2.1 | 4.4 | | 11.0 | |

Our measurements performed on organic-inorganic hybrid materials [14] and f-MLF-OH (data not included) also showed proportionality between $T'^{H}_{2}$ (as well as $T'^{C}_{2}$) and $\nu_R$ in the range of 20 - 42 kHz. In hybrid materials, the dipolar couplings in silica-bound species behaved inhomogeneously at $\nu_R$ = 40 kHz, yielding $T'^{H}_{2}$ and $T'^{C}_{2}$ relaxation times of more than 5 ms without the assistance of RF multiple-pulse sequences [14]. However, fast MAS alone proved insufficient in the case of a strongly coupled three-dimensional network of protons such as f-MLF-OH, where we observed sub-millisecond decays for many of the sites under similar conditions. By adding the RF decoupling the decay of transverse magnetization was slowed down dramatically, 5- to 20-fold compared to that in fast MAS (Tables 3.1 and 3.2). In general, the PMLG5$^{\bar{x}\bar{x}}_{mm}$ decoupling proved superior, while SAM3 performed less efficiently than both PMLG5$^{\bar{x}}_{m}$ and PMLG5$^{\bar{x}\bar{x}}_{mm}$ sequences.

Although the overall effect of decoupling is remarkable, the data in Tables 3.1 and 3.2 show considerable disparity between relaxation times measured for different sites. The measurements of $^1$H relaxation are difficult to interpret because they do not represent individual sites and functionalities. Most of the $T'^{H}_{2}$ times measured with PMLG

www.manaraa.com

decoupling at $\nu_R$ = 20.833 kHz are longer than those at $\nu_R$ = 41.667 kHz, whereas the $T'^C_2$ data are similar for most sites. Note, however, that the scaling factors are reduced at $\nu_R$ = 20.833 kHz.

In order to rationalize the results of $T'^C_2$ measurements, we note that parts of f-MLF-OH exhibit intrinsic motions at room temperature that are fast on the NMR timescale. These include the rotation of methyl groups (carbons $M^{\delta}$, $L^{\delta 1}$ and $L^{\delta 2}$) and 180º flips of the phenyl rings at a rate of ~$10^5$ $s^{-1}$; such rearrangements may be accommodated by additional motions of the surrounding chains. The $^1H$-$^{13}C$ couplings involving other carbons ($M^{\alpha}$, $L^{\alpha}$, $L^{\gamma}$, $F^{\alpha}$, $M^{\beta}$ and $M^{\gamma}$) were shown to be unaffected by motion at room temperature (see reference 34, Supporting Information). Accordingly, when both MAS and RF decoupling were used, the longest $T'^C_2$ times observed were for methyl ($M^{\delta}$, $L^{\delta 1}$ and $L^{\delta 2}$) and C-H ($M^{\alpha}$, $L^{\alpha}$, $F^{\alpha}$) carbons. The methylene carbons ($M^{\beta}$, $L^{\beta}$, $F^{\beta}$ and $M^{\gamma}$) relaxed faster, which suggests that further improvement can be achieved through more efficient decoupling. The $L^{\beta}$ and $F^{\beta}$ groups, however, also showed motional narrowing at room temperature [40], which may have interfered with decoupling. In the phenyl rings, carbons $F^{\delta 1,2}$ and $F^{\varepsilon 1,2}$ remained unresolved, whereas $F^{\zeta}$ also relaxed relatively fast, because the neighboring $^1H$ nuclei cannot be efficiently decoupled due to the flipping motion.

www.manaraa.com

Table 3.2. Measurements of transverse relaxation time $T_2'^{C}$ in f-MLF-OH under MAS at 41.667 kHz, as well as MAS at 41.667 or 20.833 kHz with homonuclear RF pulse decoupling.

| Functional group | | $\delta_{13C}$ [ppm] | $T_2^C$ [ms][(a)] | | | | | |
|---|---|---|---|---|---|---|---|---|
| | | | MAS only $s_f = 1.0$ | SAM3 $s_f = 0.71$ | PMLG5$\bar{5}^{\bar{x}}_{m}$ [(b)] $s_f = 0.71$ (*0.49*) | | PMLG5$\bar{5}^{\bar{x}\bar{x}}_{mm}$ [(b)] $s_f = 0.36$ (*0.29*) | |
| CH | $M^{\alpha}$ | 52.0 | 2.2 | 11.7 | 26.8 | *25.7* | 26.9 | *20.8* |
| | $L^{\alpha}$ | 56.8 | 1.2 | 8.8 | 25.6 | *22.3* | 22.7 | *18.8* |
| | $L^{\gamma}$ | 25.0 | 0.7 | 4.7 | 10.1 | -[(c)] | 5.4 | -[(c)] |

[(a)] As in the case of $T_2'^{H}$ (Table 3.1), each measurement consisted of 20 data points, which were fitted with a single exponential decay. The following rotor-synchronized increments of $\tau$ were used: $\Delta\tau$ = 48 us (MAS) and $\Delta\tau$ = 240 us (SAM3, PMLG5$\bar{5}^{\bar{x}}_{m}$ and PMLG5$\bar{5}^{\bar{x}\bar{x}}_{mm}$). The data were acquired with $\tau_{RD}$ = 2 s and $\tau_{CP}$ = 0.3 ms, using the RF magnetic fields $\nu_{RF}^{H}$ = 150 kHz during $\pi/2$ and PMLG pulses; $\nu_{RF}^{H}$ = 135 kHz during SAM3 sequence; $\nu_{RF}^{H}$ = 62 kHz during CP (tangent); $\nu_{RF}^{H}$ = 11 kHz during SPINAL-64 decoupling at $\nu_R$ = 41.667 kHz; $\nu_{RF}^{H}$ = 100 kHz during SPINAL-64 decoupling at $\nu_R$ = 20.833 kHz; $\nu_{RF}^{C}$ = 104 kHz during CP and $\pi$ pulse. The optimized homonuclear decoupling conditions were the same as those described in Table 3.1 (footnote (a)).

[(b)] Data obtained with $\nu_R$ = 20.833 kHz are given in italics.

[(c)] At $\nu_R$ = 20.833 kHz, peaks at 25.0 and 24.6 ppm were not resolved because the acquisition period has been limited to 10 ms to lessen the burden of high-power decoupling on the NMR probe. Therefore, the $T_2'^{C}$ values could not be independently measured for $L^{\gamma}$ and $L^{\delta 1}$.

www.manaraa.com

Table 3.2. (continued)

| Functional group | | $\delta_{13C}$ [ppm] | $T_2^C$ [ms][(a)] | | | | | |
|---|---|---|---|---|---|---|---|---|
| | | | MAS only $s_f = 1.0$ | SAM3 $s_f = 0.71$ | PMLG5$\bar{5}^{\bar{x}}_{m}$ [(b)] $s_f = 0.71$ (*0.49*) | | PMLG5$\bar{5}^{\bar{x}x}_{mm}$ [(b)] $s_f = 0.36$ (*0.29*) | |
| CH | $F^{\alpha}$ | 54.3 | 1.4 | 9.7 | 17.5 | *16.9* | 18.5 | *18.8* |
| | $F^{\zeta}$ | 127.6 | 1.2 | 3.8 | 4.6 | *7.7* | 5.9 | *6.4* |
| | Formyl | 165.2 | 2.3 | 14.4 | 21.9 | *17.4* | 19.2 | *12.6* |
| $CH_2$ | $M^{\beta}$ | 37.5 | 0.9 | 4.9 | 7.6 | *9.0* | 9.6 | *9.8* |
| | $M^{\gamma}$ | 28.7 | 0.9 | 4.0 | 5.1 | *5.6* | 7.1 | *6.2* |
| | $L^{\beta}$ | 40.6 | 0.3 | 1.8 | 4.7 | *5.4* | 4.8 | *5.9* |
| | $F^{\beta}$ | 36.9 | 0.7 | 2.0 | 3.9 | *4.5* | 5.0 | *5.5* |
| $CH_3$ | $M^{\delta}$ | 14.0 | 5.3 | 9.1 | 11.4 | *21.7* | 25.1 | *27.1* |
| | $L^{\delta 1}$ | 24.6 | 3.1 | 7.0 | 11.3 | -[(c)] | 18.2 | -[(c)] |
| | $L^{\delta 2}$ | 19.6 | 2.7 | 6.6 | 10.6 | *16.1* | 19.1 | *22.9* |

*Efficiency of polarization transfer via INEPTR*

Below we analyze the effect of RF decoupling on the efficiency of the INEPTR transfer in f-MLF-OH, focusing on fast MAS. The measurements of $T'^{H}_{2}$ and $T'^{C}_{2}$ showed that the PMLG5$\bar{5}^{\bar{x}}_{m}$ and PMLG5$\bar{5}^{\bar{x}x}_{mm}$ sequences performed better than SAM3. However, it is not immediately obvious which of the two PMLG schemes should be used, because of the effect of scaling factor $s_f$. The signal intensity observed in the INEPTR experiment can be written

www.manaraa.com

$$\begin{aligned} I(\tau_1,\tau_2) &= \frac{\gamma_{exc}}{\gamma_{obs}} I_1(\tau_1) I_2(\tau_2) \\ &= \frac{\gamma_{exc}}{\gamma_{obs}} [\sin(2\pi J s_f \tau_1)] e^{-2\tau_1 / T_2^{'H}} \\ &\quad [a_1 \sin(2\pi p_1 J s_f \tau_2) + a_2 \sin(2\pi p_2 J s_f \tau_2)] e^{-2\tau_2 / T_2^{'C}} \end{aligned}$$

(3.1)

In $^{13}$C-detected INEPTR the gyromagnetic ratios of the excited and observed nuclei are $\gamma_{exc} = \gamma_H$ and $\gamma_{obs} = \gamma_C$, respectively, and the precessions of the components of $CH_n$ multiplets are given by

$$CH: \quad a_1 = 1, p_1 = 1, a_2 = 0,$$

$$CH_2: \quad a_1 = 1, p_1 = 2, a_2 = 0,$$

(3.2)

$$CH_3: \quad a_1 = a_2 = \frac{3}{4}, p_1 = 1, p_2 = 3$$

We compared the effect of PMLG5$^{\bar{x}}_{m}$ and PMLG5$^{\bar{x}\bar{x}}_{mm}$ on the evolutions of CH, $CH_2$ and $CH_3$ groups, using the average $T'^{H}_2$ and $T'^{C}_2$ values measured for each group, and assuming the same typical value of one-bond coupling $J_{CH}$ = 130 Hz. The evolution during the polarization period ($\tau_1$) for the CH, $CH_2$ and $CH_3$ groups in f-MLF-OH is shown in Figure 3.3a, where the signal intensity expected under MAS and MAS with PMLG5$^{\bar{x}}_{m}$ or PMLG5$^{\bar{x}\bar{x}}_{mm}$ decoupling was calculated relative to that corresponding to infinitely long $T'^{H}_2$ (liquid-state, curve not shown). The effect of various decoupling schemes is further illustrated in Figure 3.3b, which shows the $^1$H intensities obtained using the spin-echo sequence in Figure 3.1a with $\tau_1$ = 1.2 ms. The maximum intensities $I_1(\tau_1^{max})$ and $I_2(\tau_2^{max})$ expected in f-MLF-OH, as well as the corresponding delays $\tau_1^{max}$ and $\tau_2^{max}$, are

www.manaraa.com

listed in Table 3.3. Also listed in the last column of Table 3.3 are the overall intensities $I_1(\tau_1)I_2(\tau_2)$.

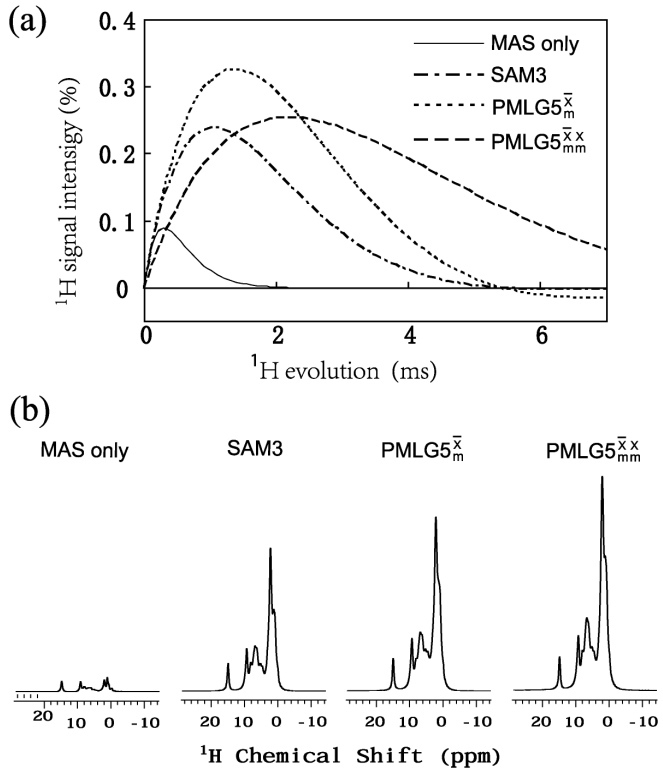


**Fig. 3.3**. (a) Decoherence of $^1$H signal due to $T'^{H}_{2}$ as a function of $\tau_1$ measured under various decoupling conditions using the spin-echo sequence. The signal intensity is shown relative to that corresponding to infinitely long $T'^{H}_{2}$. (b) The corresponding $^1$H spectra obtained at $\tau_1$ = 1.2 ms.

www.manaraa.com

Table 3.3. The effect of decoupling during $^{1}H \rightarrow ^{13}C$ INEPTR on the efficiency of polarization transfer in f-MLF-OH under fast MAS ($\nu_R$ = 41.667 kHz).

| Group | RF decoupling | $T'^{H}_{2}$ [ms] | $\tau_1^{max}$ [ms] | $I_1(\tau_1^{max})$ | $T'^{C}_{2}$ [a] [ms] | $\tau_2^{max}$ [ms] | $I_2(\tau_2^{max})$ | $I_1(\tau_1^{max})I_2(\tau_2^{max})$ |
|---|---|---|---|---|---|---|---|---|
| CH | none | 0.6 | 0.3 | 0.09 | 1.5 | 0.7 | 0.21 | 0.02 |
| | PMLG5$^{\bar{x}}_{m}$ | 3.5 | 1.4 | 0.33 | 18 | 2.4 | 0.75 | 0.25 |
| | PMLG5$^{\bar{x}\bar{x}}_{mm}$ | 5.1 | 2.2 | 0.25 | 16 | 4.0 | 0.56 | 0.14 |
| $CH_2$ | none | 0.6 | 0.3 | 0.09 | 0.9 | 0.4 | 0.25 | 0.02 |
| | PMLG5$^{\bar{x}}_{m}$ | 5.3 | 1.7 | 0.44 | 5.3 | 1.1 | 0.64 | 0.28 |
| | PMLG5$^{\bar{x}\bar{x}}_{mm}$ | 10 | 3.3 | 0.43 | 6.6 | 1.9 | 0.50 | 0.21 |
| $CH_3$ | none | 0.4 | 0.2 | 0.06 | 3.7 | 0.8 | 0.91 | 0.05 |
| | PMLG5$^{\bar{x}}_{m}$ | 4.4 | 1.6 | 0.39 | 11 | 1.0 | 0.96 | 0.37 |
| | PMLG5$^{\bar{x}\bar{x}}_{mm}$ | 11 | 3.5 | 0.45 | 21 | 1.9 | 0.95 | 0.43 |

[a] These are average $T'^{C}_{2}$ values for each group calculated from the data in Table 3.2.

Based on the results in Table 3.3, the PMLG5$^{\bar{x}}_{m}$ decoupling is most suitable for application during INEPTR, in spite of the fact that the PMLG5$^{\bar{x}\bar{x}}_{mm}$ sequence yields longer $T'^{H}_{2}$ and $T'^{C}_{2}$ relaxation times. The use of PMLG5$^{\bar{x}}_{m}$ may reduce the relaxation losses by more than 10 times for CH and $CH_2$, and up to 7 times for $CH_3$ relative to fast MAS alone. Ultimately, one set of $\tau_1$ and $\tau_2$ values must be chosen in order to achieve the best overall sensitivity. In solution NMR this is achieved with $\tau_1 \cong 1/4J_{CH}$ and $\tau_2 \cong 0.3/J_{CH}$ (note that the requirement for full refocusing depends on multiplicity [41]), where $J_{CH}$ is the typical expected value for the $J$ coupling: e.g., for $J_{CH}$ = 130 Hz, $\tau_1$ and $\tau_2$ are both on the order of 2 ms. In samples with considerable range of couplings and multiplicities, non-ideal transfers are unavoidable. In solids, non-uniform $T'_2$ relaxation may introduce additional

www.manaraa.com

inaccuracy. Still, our data suggest that by using $\tau_1$ and $\tau_2$ delays of around 1.5 ms, the overall efficiency of $^1H \rightarrow ^{13}C$ INEPTR transfer should be on the order of 25% of the ideal transfer in liquid state. As noted in Section 3.1, for most sites the $T'^H_2$ times and $T'^C_2$ times measured with PMLG$5^{\bar{x}}_m$ decoupling at $\nu_R$ = 20.833 kHz are longer and similar, respectively, to those at $\nu_R$ = 41.667 kHz. However, this increase is more than offset by the reduced scaling factors (see Tables 3.1 and 3.2), leading to lower overall sensitivity.

The indirectly detected experiments utilizing $^{13}C \rightarrow ^1H$ INEPTR should benefit from homonuclear $^1H$ decoupling in a similar way. In this case $\gamma_{exc} = \gamma_C$ and $\gamma_{obs} = \gamma_H$, yet the sensitivity ratio between solid-state and liquid-state experiments will remain similar to that given in the last column of Table 3.3.

Our 2D experiments, discussed in the sections below, have substantiated the above expectations.

*2D through-bond HETCOR spectra of f-MLF-OH*

Here, the qualities of various approaches to 2D HETCOR NMR are assessed experimentally through a series of directly and indirectly detected measurements on tripeptide f-MLF-OH. The experimental schemes and conditions are summarized in Table 3.4, and selected spectra are shown in Figure 3.4 and 3.5. All experiments were individually optimized and carried out under well-matched conditions. The $^1H$-detected spectra used $^1H \rightarrow ^{13}C$ cross-polarization to create initial $^{13}C$ magnetization, which imposed quantitative distortions consistent with those in Figure 3.2a. Below we compare the overall sensitivity, resolution and structural information offered by these methods.

www.manaraa.com

Table 3.4. The list of 2D HETCOR experiments performed on f-MLF-OH. The experiments used the pulse sequences shown in Figure 3.1b and c, and were individually optimized as explained in section 3.3.

| Experiment[(a)] | | $\nu_R$ [kHz] | Decoupling during $t_1$ | Mixing | $\tau_1^{max}$ [ms] | $\tau_2^{max}$ [ms] | Decoupling during $\tau_1, \tau_2$ | Decoupling during $t_2$ |
|---|---|---|---|---|---|---|---|---|
| **1** | $^{13}C\{^1H\}$ | 41.667 | SPINAL-64 | INEPTR | 1.20 | 0.84 | $PMLG5^{\bar{x}}_{m}$ | SPINAL-64 |
| **2** | $^{13}C\{^1H\}$ | 41.667 | $PMLG5^{\bar{x}}_{m}$ | INEPTR | 1.20 | 0.84 | $PMLG5^{\bar{x}}_{m}$ | SPINAL-64 |
| **3** | $^{13}C\{^1H\}$ | 41.667 | $PMLG5^{\bar{x}x}_{mm}$ | INEPTR | 1.20 | 0.84 | $PMLG5^{\bar{x}}_{m}$ | SPINAL-64 |
| **4** | $^{13}C\{^1H\}$ | 20.833 | $PMLG5^{\bar{x}}_{m}$ | INEPTR | 1.68 | 1.44 | $PMLG5^{\bar{x}}_{m}$ | SPINAL-64 |
| **5** | $^1H\{^{13}C\}$ | 41.667 | SPINAL-64 | INEPTR | 0.31 | 0.22 | - | SPINAL-64 |
| **6** | $^1H\{^{13}C\}$ | 41.667 | SPINAL-64 | INEPTR | 0.84 | 1.20 | $PMLG5^{\bar{x}}_{m}$ | SPINAL-64 |
| **7** | $^1H\{^{13}C\}$ | 41.667 | SPINAL-64 | CP | - | | - | SPINAL-64 |

[(a)] All measurements were performed with a fully loaded rotor (~8 μL). Initial $^{13}C$ polarization in the $^1H$-detected experiments (**5-7**) was produced via CP under the conditions given in the caption to Figure 3.2. The homo- and heteronuclear $^1H$ decoupling conditions were the same as given in footnote (a) to Tables 3.1 and 3.2. During the acquisition of $^1H$-detected spectra, SPINAL-64 heteronuclear decoupling performed very well at low power ($\nu_{RF}^{C}$ = 11 kHz). Additional experimental details are as follows: experiment **1**: NS = 64, $\Delta t_1$ = 24 μs (64 rows), AT = 4.7 h; experiment **2**: NS = 16, $\Delta t_1$ = 5 μs (300 rows), AT = 5.5 h; experiment **3**: NS = 16, $\Delta t_1$ = 30 μs (300 rows), AT = 5.5 h; experiment **4**: NS = 16, $\Delta t_1$ = 27 μs (190 rows), AT = 3.5 h; experiment **5**: $\tau_{RR}$ = 48 ms, NS = 32, $\Delta t_1$ = 24 μs (800 rows), AT = 30 h; experiment **6**: $\tau_{RR}$ = 48 ms, NS = 16, $\Delta t_1$ = 24 μs (800 rows), AT = 15 h; and experiment **7**: $\tau_{RR}$ = 48 ms, $\tau_{CP}$ = 0.3 ms, NS = 16, $\Delta t_1$ = 24 μs (800 rows), AT = 15 h.

www.manaraa.com

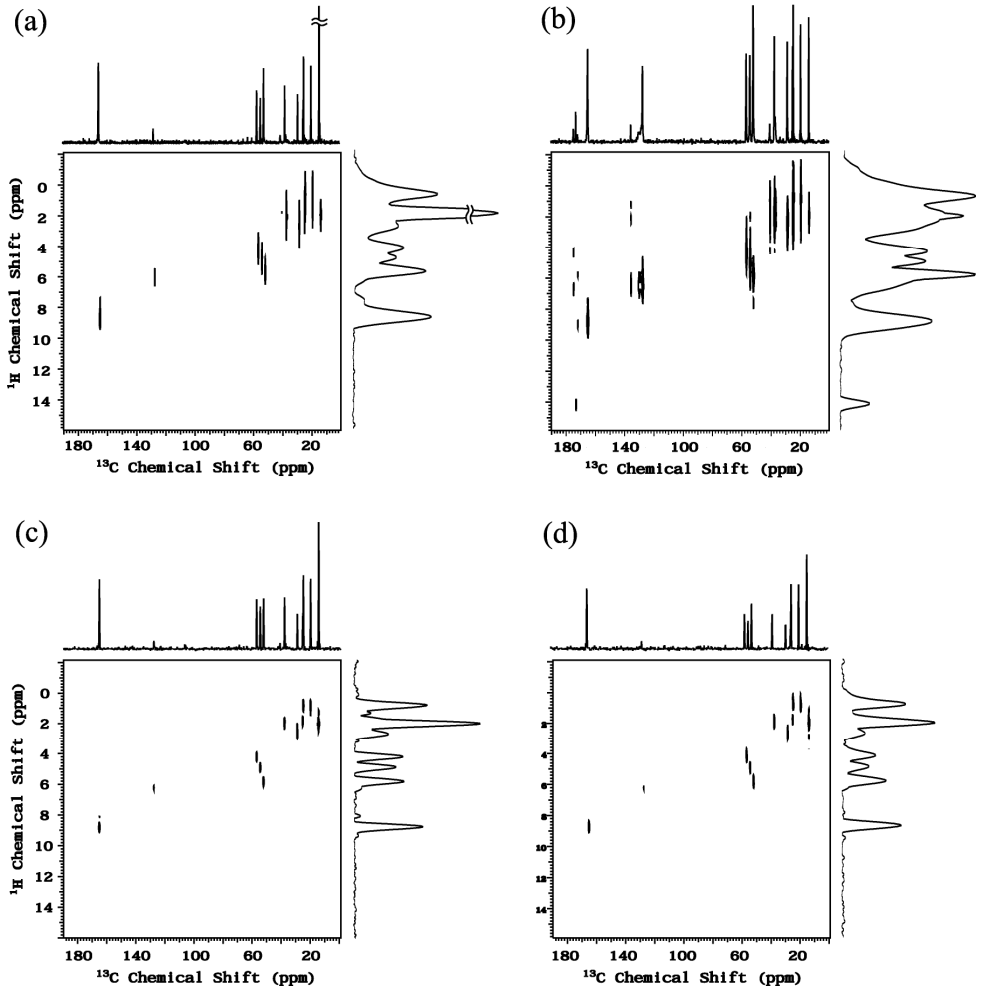


**Fig 3.4**. 2D HETCOR spectra of f-MLF-OH obtained using (a) $^{1}$H detection, INEPTR mixing and $\nu_R$ = 41.667 kHz, (b) $^{1}$H detection, CP mixing and $\nu_R$ = 41.667 kHz, (c) $^{13}$C detection, INEPTR mixing and $\nu_R$ = 41.667 kHz and (d) $^{13}$C detection, INEPTR mixing and $\nu_R$ = 20.833 kHz (experiments **6**, **7**, **2** and **4**, respectively). Acquisition times were 15 h (a,b), 5.5 h (c) and 3.5 h (d). Other experimental details are given in the footnotes to Tables 3.1, 3.2 and 3.4. Note that the spectra acquired with $\nu_R$ = 41.667 kHz (a-c) used low-power SPINAL-64 decoupling. Since spectrum (d) required the use of high power ($\nu_{RF}^{H}$ = 100 kHz, see Table 3.2), the acquisition period was limited to 10 ms. To compare spectra (c) and (d), the former was also broadened accordingly. Such broadening was not applied to this spectrum in Figure 3.5.

www.manaraa.com

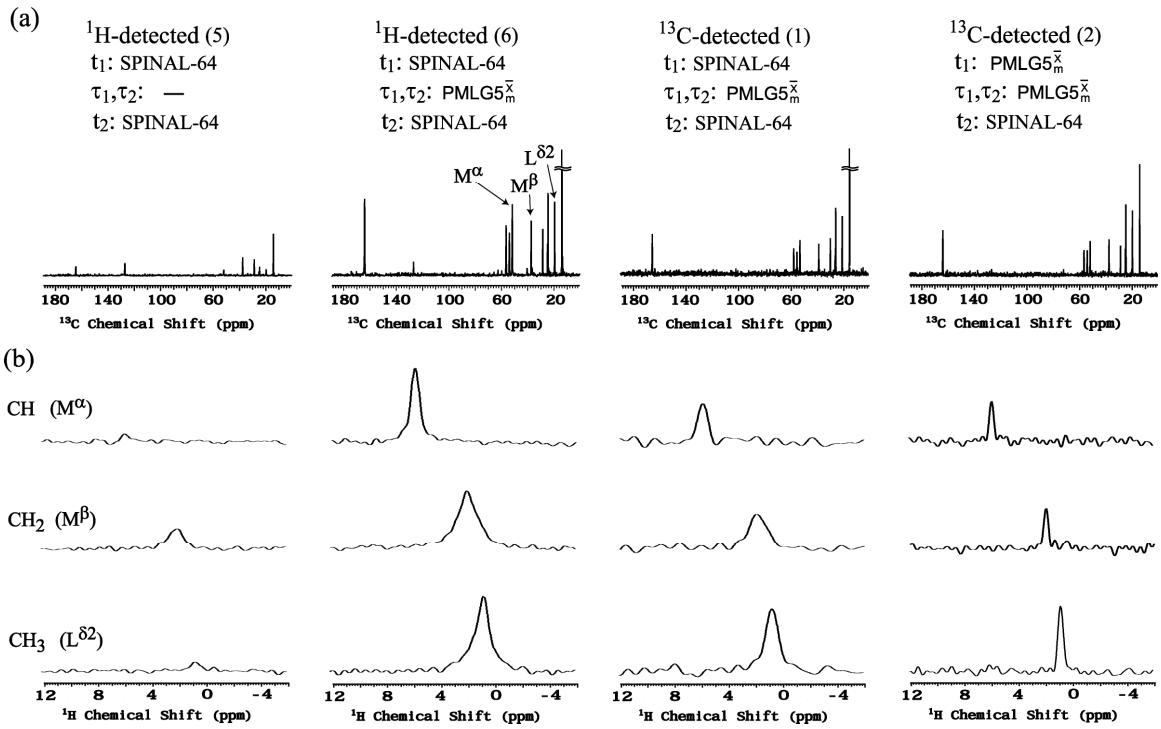


**Fig. 3.5**. (a) 1D $^{13}$C skyline projections and (b) representative $^1$H slices from spectra **5**, **6**, **1** and **2**. All experiments used mixing via INEPTR and MAS at 41.667 kHz. For clarity, the decoupling conditions are listed at the top of each column. Other experimental details are given in footnotes to Tables 3.1, 3.2 and 3.4. The spectra are normalized such that the peak heights are proportional to sensitivity per scan.

*Sensitivity and resolution*.

Our experiments showed that high-quality through-bond HETCOR spectra can be obtained under fast MAS using both direct and indirect detection and confirmed that the sensitivity can indeed be dramatically increased by the use of homonuclear $^1$H decoupling during $\tau_1$ and $\tau_2$ (Figure 3.4 and 3.5).

In the top row of Figure 3.5, the skyline $^{13}$C projections of $^1$H-detected spectra **5** and **6** (obtained without and with PMLG5$^{\bar{x}}_{m}$ decoupling during INEPTR) are shown along with

www.manaraa.com

the projections of $^{13}$C-detected spectrum **1** (obtained with PMLG5$^{\bar{x}}_{m}$ decoupling applied only during INEPTR) and spectrum **2** (where PMLG5$^{\bar{x}}_{m}$ decoupling was also applied during $t_1$). Selected $^1$H cross sections of peaks representing CH ($M^{\alpha}$), $CH_2$ ($M^{\beta}$) and $CH_3$ ($L^{\delta 1}$) are compared below. In the case of $^1$H{$^{13}$C} HETCOR, the S/N gain due to $^1$H decoupling during INEPTR is approximately 10-fold for CH, at least 3-fold for $CH_2$ and 7-fold for $CH_3$ groups (compare Figure 3.5a and b). For CH and $CH_3$ groups the result is approximately as expected from Table 3.3, although the maximum intensity was observed at lower-than-expected values of $\tau_1$ and $\tau_2$ (compare Tables 3.3 and 3.4). It is clear in Figure 3.4a, c, d and Figure 3.5 that the methyl carbons and all carbons exhibiting strong (i.e. unaffected by motion) $^1$H-$^{13}$C couplings ($M^{\alpha}$, $L^{\alpha}$, $F^{\alpha}$, $M^{\beta}$, $M^{\gamma}$, $L^{\gamma}$ and formyl groups) can achieve through-bond polarization relatively easily. The methylene carbons $L^{\beta}$ and $F^{\beta}$, resonating at 40.6 ppm and 36.9 ppm, are polarized less efficiently, as expected from the transverse relaxation data.

When comparing the indirect and direct methods we recall that the sensitivity gain not only depends on the polarization efficiency, but is also proportional to $(\gamma_{obs}/\gamma_{exc})^{3/2}$ and to the square root of the NMR linewidths in Hz $(\Delta\nu_{exc}/\Delta\nu_{obs})^{1/2}$ [6]. Remarkably, the $^1$H-detected experiment **6** provided higher overall S/N per unit time than $^{13}$C-detected experiments **1** and **2** (Figure 3.5), in spite of the unfavourable linewidth ratio in f-MLF-OH. However, experiment **2** yielded much better resolution in the $^1$H dimension, making it potentially advantageous in studies of complex molecules. In this context, it is important to note that the use of PMLG5$^{\bar{x}\bar{x}}_{mm}$ during $t_1$, which we tested in experiment **3** (spectrum not shown), did not offer any advantage yielding a spectrum with similar $^1$H linewidths (in ppm) and sensitivity as that in experiment **2** (Figure 3.4c).

*Fast MAS versus 'slow' MAS.*

www.manaraa.com

The merit of using fast MAS in $^{13}$C-detected INEPT experiments can be gauged by comparing the best spectra taken at $\nu_R$ = 41.667 kHz and 20.883 kHz (experiments **2** and **4**, shown in Figure 3.4c and d, respectively). Optimization of these experiments yielded different conditions for $^{1}$H homonuclear decoupling, as shown in footnote (a) to Table 3.1. When experiment **4** was performed under the $^{1}$H decoupling conditions optimal for experiment **2**, the spectrum lacked sensitivity, especially with regard to methylene groups, which were almost completely lost (spectrum not shown). We further note that in experiment **4** the SPINAL-64 $^{1}$H decoupling had to be performed using a high RF magnetic field of $\nu_{RF}^{H} \cong$ 100 kHz. To lessen the burden on the probe, the acquisition period $t_2$ was limited to 10 ms, causing broadening of the $^{13}$C lines. In order to make spectra **2** and **4** easier to compare, spectrum **2**, which was acquired without truncation under low-power decoupling and is displayed in Figure 3.4c, was broadened accordingly during processing (Figure 3.4c). Although spectrum **2** has comparable S/N per unit time, it is better resolved in the $^{1}$H dimension and more quantitative than the one obtained with $\nu_R$ = 20.883 kHz. Perhaps the resolution in spectrum **4** could be improved by reducing the sample volume to improve the homogeneity of the RF magnetic field.

*Through-bond versus through-space correlations*.

Finally, it is instructive to compare the through-bond $^{1}$H{$^{13}$C} correlation spectra with those obtained using CP under otherwise identical conditions (experiments **6** and **7**, spectra shown in Figure 3.4a and b, respectively). To maximize the polarization of carbon sites, the CP-based spectrum was acquired using $\tau_{CP}$ from 0.3 ms. For protonated carbons, the sensitivity of this spectrum is 1.5-2 times higher than that of spectrum **6**. As expected, it features a number of additional correlations involving all carbons identified in the 1D CPMAS spectrum of f-MLF-OH (Figure 3.2a). These long-range correlations can be suppressed by limiting the contact time to less than 50 μs, which would considerably

www.manaraa.com

reduce the overall sensitivity. Bearing in mind that CP-based can be affected by motion, RF homogeneity, and $T_{1\rho}$ relaxation, our results show that through-bond correlation NMR spectroscopy under fast MAS can be a very effective tool for studying fully coupled, naturally abundant solids.

*2D HETCOR spectra of brown coal*

Fossil fuels are structurally very heterogeneous, which is reflected in their $^{1}H$ and $^{13}C$ solid-state NMR spectra. Even when state-of-the-art line narrowing methods are used, the solid-state NMR spectra of both nuclei feature relatively broad bands representing sp, $sp^2$ and $sp^3$ functionalities. The structual characterization of coals by NMR has been mainly confined to utilization of liquid-state studies of coal-derived liquids and 1D spectral editing techniques developed for simplification of solid-state spectra [42]. Until now, relatively few 2D solid-state NMR experiments have been applied to this purpose [42-44].

Indirectly detected $^{1}H\{^{13}C\}$ spectra of brown coal were acquired with mixing via INEPTR (experiment **6**, Figure 3.6a) and CP (experiment **7**, Figure 3.6b), yielding comparable intensities. Experiment **2** (not shown) was also performed, but was less sensitive and did not provide improved resolution in the $^{1}H$ dimension. The INEPTR-based spectrum in Figure 3.6a does not feature any $^{13}C$ resonances near 180 ppm, which are quite intense in the CP-based spectrum. This range of chemical shifts represents various types of carbonyl groups, in particular those involved in aldehyde and carboxylic functionalities. Another 'missing' resonance in Figure 3.6a is one centred at 150 ppm, generally associated with various types of quaternary aromatic carbons, including aliphatic chain- and oxygen-bound carbons. A discernible resonance near 80 ppm is present in both spectra, which suggests the presence of sp carbons in alkynes and $sp^2$ carbons in olefins.

www.manaraa.com

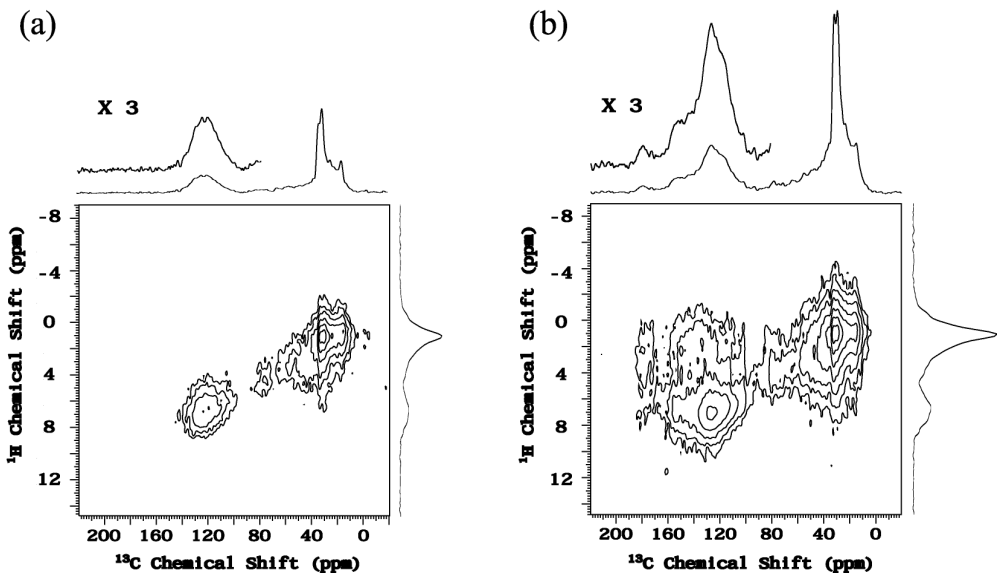


**Fig. 3.6**. 2D $^1$H{$^{13}$C} HETCOR spectra of brown coal acquired using INEPTR (a) and CP (b) transfers during mixing. The following RF magnetic fields were used: $\nu_{RF}^{H}$ = 150 kHz during π/2 and PMLG5$_m^{\bar{x}}$ pulses, $\nu_{RF}^{H}$ = 62 kHz during CP (tangent), $\nu_{RF}^{H}$ = 11 kHz during SPINAL-64 decoupling in $t_1$, $\nu_{RF}^{C}$ = 104 kHz during CP, π/2 and π pulses, and $\nu_{RF}^{C}$ = 11 kHz during SPINAL-64 decoupling in $t_2$. Other experimental conditions were as follows: $\nu_R$ = 41.667 kHz, $\tau_{CP}$ = 1.5 ms, $\tau_{RR}$ = 24 ms, $\tau_1$ = 0.84 ms, $\tau_2$ = 1.2 ms, $\tau_{PMLG}$ = 0.75 us, $\tau_c$ = 15 us, $\tau_{RD}$ = 0.8 s, NS = 176, $\Delta t_1$ = 24 μs (100 rows), and AT = 8.7 h.

### 3.5 Conclusions

*J* couplings can be successfully exploited in directly and indirectly detected 2D HSQC-type HETCOR experiments under fast MAS (~42 kHz), providing through-bond $^{13}$C-$^1$H correlations in naturally abundant solids with an efficiency that rivals that of traditional through-space experiments. Efficient $^1$H decoupling plays a key role in preventing the decoherence of $^1$H and $^{13}$C magnetizations during polarization transfer via INEPTR.

www.manaraa.com

Among the tested decoupling schemes ( PMLG5$^{\bar{x}}_{m}$ , PMLG5$^{\bar{x}x}_{mm}$ and SAM3), PMLG5$^{\bar{x}}_{m}$ proved most suitable, providing sensitivity gains of 3-10 in strongly coupled $^{1}$H-$^{13}$C pairs. Remarkably, the best results were obtained when $\nu_R$ was smaller than $\nu_c$ (in the case of PMLG5$^{\bar{x}x}_{mm}$ for $\nu_R/\nu_c \approx 0.62$) due to good decoupling efficiency and a high scaling factor. At ultrahigh speeds (~70 kHz), the SAM3 method may become competitive with PMLG schemes.

2D HETCOR spectra of well ordered (crystalline tripeptide f-MLF-OH) and highly disordered (brown coal) samples were measured and analyzed. In spite of an unfavorable $^{1}$H to $^{13}$C linewidth ratio in f-MLF-OH, the indirect detection method offered higher overall sensitivity. However, in cases where $^{1}$H resolution under fast MAS alone is unsatisfactory, $^{13}$C detection with $^{1}$H homonuclear decoupling during $t_1$ may be the method of choice. Our measurements showed that experiments performed under fast MAS compare favorably with those carried out at a lower spinning rate (~21 kHz). Proper optimization of $^{1}$H homonuclear decoupling proved very important in achieving high efficiency and resolution. A simple and reliable optimization scheme was used, which will be detailed in a forthcoming publication. The through-bond polarization transfer will undoubtedly become an important addition to cross-polarization in designing new multidimensional schemes dedicated for high-field, fast-MAS applications.

### 3.6 Acknowledgment

This research was supported at the Ames Laboratory by the U.S. Department of Energy, Office of Basic Energy Sciences, under Contract No. DE-AC02-07CH11358. The authors thank Drs. J.-P. Amoureux and M. Hong for helpful discussions and Dr. J. Wiench for experimental assistance. The sample of brown coal was kindly provided by Prof. D. Michel.

www.manaraa.com

### 3.7 References

[1] A. Samoson, Extended magic-angle spinning, in: D.M.R. Grant, K. Harris (Eds.), *Encyclopedia of Nuclear Magnetic Resonance*, Vol. 9, John Wiley & Sons, Chichester, 2002, pp. 59-64.

[2] L.S. Du, A. Samoson, T. Tuherm, C.P. Grey, 19F/23Na double resonance MAS NMR study of oxygen/fluorine ordering in the oxyfluoride Na5W3O9F5, *Chem. Mater.* 12 (2000) 3611-3616.

[3] M. Ernst, A. Detken, A. Böckmann, B.H. Meier, NMR spectra of a microcrystalline protein at 30 kHz MAS, *J. Am. Chem. Soc.* 125 (2003) 15807-15810.

[4] J. Trebosc, J.W. Wiench, S. Huh, V.S.-Y. Lin, M. Pruski, Studies of organically functionalized mesoporous silicas using heteronuclear solid-state correlation NMR spectroscopy under fast magic angle spinning, *J. Am. Chem. Soc.* 127 (2005) 7587-7593.

[5] M. Ernst, M.A. Meier, T. Tuherm, A. Samoson, B.H. Meier, Low-power high-resolution solid-state NMR of peptides and proteins, *J. Am. Chem. Soc.* 126 (2004) 4764-4765.

[6] Y. Ishii, R. Tycko, Sensitivity enhancement in solid state 15N NMR by indirect detection with high-speed magic angle spinning, *J. Magn. Reson.* 142 (2000) 199-204.

[7] B. Reif, R.G. Griffin, $^{1}$H detected $^{1}$H,$^{15}$N correlation spectroscopy in rotating solids, *J. Magn. Reson.* 160 (2003) 78-83.

[8] J.W. Wiench, C.E. Bronniman, V.S.-Y. Lin, M. Pruski, Chemical shift correlation NMR spectroscopy with indirect detection in fast rotating solids: Studies of organically functionalized mesoporous silicas, *J. Am. Chem. Soc.* 129 (2007) 12076-12077.

www.manaraa.com

[9] D.H. Zhou, G. Shah, M. Cormos, C. Mullen, D. Sandoz, C.M. Rienstra, Proton-detected solid-state NMR spectroscopy of fully protonated proteins at 40 kHz magic-angle-spinning, *J. Am. Chem. Soc.* 129 (2007) 11791-11801.

[10] D.H. Zhou, C.M. Rienstra, Rapid analysis of organic compounds by proton-detected heteronuclear correlation NMR spectroscopy with 40 kHz magic angle spinning, *Angew. Chem. Int. Ed.* 47 (2008) 7328-7331.

[11] M. Leskes, S. Steuernagel, D. Schneider, P.K. Madhu, S. Vega, Homonuclear dipolar decoupling at magic angle spinning frequencies up to 65 kHz in solid-state nuclear magnetic resonance, *Chem. Phys. Lett.* 466 (2008) 95-99.

[12] J.-P. Amoureux, B. Hu, J. Trebosc, Enhanced resolution in proton solid-state NMR with very fast MAS experiments, *J. Magn. Reson.* 193 (2008) 305-307.

[13] B. Elena, A. Lesage, S. Steuernagel, A. Böckmann, L. Emsley, Proton to Carbon-13 INEPT in Solid-State NMR Spectroscopy, *J. Am. Chem. Soc.* 127 (2005) 17296-17302.

[14] K. Mao, J.W. Wiench, V.S.-Y. Lin and M. Pruski, Indirectly detected through-bond chemical shift correlation NMR spectroscopy under fast MAS: Studies of organic-inorganic hybrid materials, *J. Magn. Reson.* 196 (2009) 92-95.

[15] M. Mehring, J.S. Waugh, Magic-Angle NMR in solids, *Phys. Rev. B.* 5 (1972) 3459-3481.

[16] B.C. Gerstein, R.G. Pembleton, R.C. Wilson, L.M.J. Ryan, High resolution NMR in randomly oriented solids with homonuclear dipolar broadening: Combined multiple pulse NMR and magic angle spinning, *Chem. Phys.* 66 (1977) 361-362.

[17] E. Vinogradov, P.K. Madhu, S. Vega, Strategies for high-resolution proton spectroscopy, *Top. Curr. Chem.* 246 (2004) 33-90.

www.manaraa.com

[18] D. Sakellariou, A. Leasge, P. Hodgkinson, L. Emsley, Homonuclear dipolar decoupling in solid-state NMR using continuous phase modulation, *Chem. Phys. Lett.* 319 (2000) 253-260.

[19] P.K. Madhu, X. Zhao, M.H. Levitt, High-resolution $^{1}$H NMR in the solid state using symmetry-based pulse sequences, *Chem. Phys. Lett.* 346 (2001) 142-148.

[20] S. Paul, R.S. Thakur, P.K. Madhu, $^{1}$H homonuclear dipolar decoupling at high magic-angle spinning frequencies with rotor-synchronized symmetry sequences, *Chem. Phys. Lett.* 456 (2008) 253-256.

[21] E. Vinogradov, P.K. Madhu, S. Vega, High-resolution proton solid-state NMR spectroscopy by phase-modulated Lee-Goldburg experiment, *Chem. Phys. Lett.* 314 (1999) 443-450.

[22] A. Bielecki, A.C. Kolbert, M.H. Levitt, Frequency-switched pulse sequences – homonuclear decoupling and dilute spin NMR in solids, *Chem. Phys. Lett.* 155 (1989) 341-346.

[23] M. Leskes, P.K. Madhu, S. Vega, A broad-banded z-rotation windowed phase-modulated Lee-Goldburg pulse sequence for $^{1}$H spectroscopy in solid-state NMR, *Chem. Phys. Lett.* 447 (2007) 370-374.

[24] E. Vinogradov, P.K. Madhu, S. Vega, A bimodal Floquet analysis of phase modulated Lee-Goldburg high resolution proton magic angle spinning NMR experiments, *Chem. Phys. Lett.* 329 (2000) 207-214.

[25] E. Vinogradov, P.K. Madhu, S. Vega, Phase-modulated Lee-Goldburg magic angle spinning proton nuclear magnetic resonance experiments in the solid state: A bimodal Floquet theoretical treatment, *J. Chem. Phys.* 115 (2001) 8983-9000.

[26] E. Vinogradov, P.K. Madhu, S. Vega, Proton spectroscopy in solid-state nuclear magnetic resonance with windowed phase modulated Lee-Goldburg decoupling sequences, *Chem. Phys. Lett.* 354 (2002) 193-202.

www.manaraa.com

[27] L. Bosman, P.K. Madhu, S. Vega, E. Vinogradov, Improvement of dipolar decoupling sequences in solid-state nuclear magnetic resonance utilizing radiofrequency imperfections, *J. Magn. Reson.* 169 (2004) 39-48.

[28] M. Leskes, P.K. Madhu, S. Vega, Proton line narrowing in solid-state nuclear magnetic resonance: New insights from windowed phase-modulated Lee-Goldburg sequence, *J. Chem. Phys.* 125 (2006) 124506/1-18.

[29] E.K. Paulson, C.R. Morcombe, V. Gaponenko, B. Dancheck, R.A. Byrd, K.W. Zilm, Sensitive high resolution inverse detection NMR spectroscopy of proteins in the solid state, *J. Am. Chem. Soc.* 125 (2003) 15831-15836.

[30] Y. Ishii, J.P. Yesionowski, R. Tycko, Sensitivity enhancement in solid-state $^{13}C$ NMR of synthetic polymers and biopolymers by $^{1}H$ NMR detection with high-speed magic angle spinning, *J. Am. Chem. Soc.* 123 (2001) 2921-2922.

[31] B.M. Fung, A.K. Khitrin, K. Ermolaev, An Improved Broadband Decoupling sequence for Liquid Crystals and solids, *J. Magn. Reson.* 142 (2000) 97-101.

[32] M. Ernst, A. Samoson, B.H. Meier, Low-power decoupling in fast magic-angle spinning NMR, *Chem. Phys. Lett.* 348 (2001) 293-302.

[33] C.M. Rienstra, L. Tucker-Kellogg, C.P. Jaroniec, M. Hohwy, B. Rief, M.T. McMahon, B. Tidor, T. Lozano-Perez, R.G. Griffin, De novo determination of peptide structure with solid-state magic-angle spinning NMR spectroscopy, *Proc. Natl. Acad. Sci. U.S.A.* 99 (2002) 10260-10265.

[34] A.N. Garroway, D.L. VanderHart, W.L. Earl, $^{13}C$ n.m.r. in organic solids: limits to spectral resolution and to determination of molecular motion, *Philos. Trans. R. Soc. London, Ser. A* 299 (1981) 609-628.

[35] U. Schwerk, D. Michel, M. Pruski, Local magnetic field distribution in a polycrystalline sample exposed to a strong magnetic field, *J. Magn. Reson.* 119A (1996) 157-164.

www.manaraa.com

[36] A. Samoson, T. Tuherm, Z. Gan, High-field high-speed MAS resolution enhencement in $^{1}$H NMR spectroscopy of solids, *Solid State Nucl. Magn. Reson.* 20 (2001) 130-136.

[37] V.E. Zorin, S.P. Brown, P. Hodgkinson, Origins of linewidth in $^{1}$H magic-angle spinning NMR, *J. Chem. Phys.* 125 (2006) 144508.

[38] E. Brunner, D. Freude, B.C. Gerstein, H. Pfeifer, Residual linewidths of NMR-spectra of spin-1/2 systems under magic-angle spinning, *J. Magn. Reson.* 90 (1990) 90-90.

[39] U. Haeberlen, J.S. Waugh, Coherent averaging effects in magnetic resonance, *Phys. Rev.* 175 (1968) 453-467.

[40] V.S. Bajaj, P.C.A. van der Wel, R.G. Griffin, Observation of a low-temperature, dynamically driven structural transition in a polypeptide by solid-state NMR spectroscopy, *J. Am. Chem. Soc.* 131 (2009) 118-128.

[41] D.T. Pegg, D.M. Doddrell, W.M. Brooks, M.R. Bendall, Proton polarization transfer enhancement for a nucleus with arbitrary spin quantum number from n-scalar coupled protons for arbitrary preparation times, *J. Magn. Reson.* 44 (1981) 32-40.

[42] R.E. Botto, Fossil Fuels, in: D.M. Grant, R.K. Harris (Eds.), *Encyclopedia of Nuclear Magnetic Resonance*, Vol. 3, John Wiley & Sons, Chichester, 1996, pp. 2101-2118.

[43] K.W. Zilm, G.G. Webb, C-13 proton shift correlation spectroscopy of a whole coal, *Fuel*, 65 (1986) 721-724.

[44] J.Z. Hu, M.S. Solum, C.M.V. Taylor, R.J. Pugmire, D.M. Grant, Structural determination in carbonaceous solids using advanced solid-state NMR techniques, *Energy & Fuels* 15 (2001) 14-22.

www.manaraa.com

# Chapter 4

## Homonuclear dipolar decoupling under fast MAS: Resolution patterns and simple optimization strategy

Published in *J. Magn. Reson*. 203 (2010) 144-149

Kanmi Mao, and Marek Pruski

### 4.1 Abstract

A simple method is shown for optimization of $^{1}$H homonuclear dipolar decoupling at MAS rates exceeding 10 kHz. By monitoring the intensity of a spin-echo under the decoupling conditions, it is possible to optimize the amplitude of the RF magnetic field, the cycle time of the decoupling sequence and the resonance offset within minutes. As a result, the decoupling efficiency can be quickly and reliably fine-tuned without using a reference sample. The utility of this method has been confirmed by studying the resolution patterns for the supercycled PMLG scheme, which were found to be in excellent agreement with earlier theoretical predictions and verified in high-resolution 2D $^{1}$H-$^{1}$H experiments.

### 4.2 Introduction

Overcoming the strong homonuclear dipolar interactions between $^{1}$H nuclei in has been one of the principal pursuits in solid-state NMR spectroscopy for several decades. The advancement of high resolution $^{1}$H NMR in solids commenced with the introduction of Lee-Goldburg (LG) RF decoupling [1] and was followed by the development of multiple-pulse sequences for static samples [2-4]. The first highly resolved $^{1}$H spectra were attained by combining these sequences with slow magic spinning (MAS), to eliminate the chemical shift anisotropy (CSA), in an experiment referred to as CRAMPS (combined rotation and multiple pulse sequence) [5]. Subsequently, improved RF schemes emerged that enabled high-resolution $^{1}$H NMR at MAS rates up to 25 kHz, which included frequency-switched LG

www.manaraa.com

(FSLG) [6], phase-modulated LG (PMLG) [7], decoupling using mind-boggling optimization (DUMBO) [8] and symmetry-based (R-based and smooth amplitude modulation, SAM) [9,10] pulse sequences. In depth theoretical analyses of most of these experiments were offered based on the average Hamiltonian theory [11,12] and the Floquet theory [13,14]. It has been generally implied that the homonuclear decoupling sequences perform well under the so-called 'quasi-static condition', where the sample spinning period $\tau_R = (\nu_R)^{-1}$ is long relative to the cycle time of the RF sequence $\tau_c$. However, the development of ultra fast MAS [15], which can now reach frequencies in the range $40 \leq \nu_R \leq 70$ kHz, induced interest in application of homonuclear decoupling under conditions that can no longer be 'quasi-static' under practical RF amplitudes. Most recently, the windowed and windowless PMLG, DUMBO and SAM schemes were shown to perform surprisingly well in the regime where $\tau_R$ and $\tau_c$ are comparable (but not equal), both in terms of resolution [16,17] and sensitivity [17], and theoretical arguments were presented that rationalize the experimentally observed resolution patterns [18]. These findings open new opportunities for designing two- and three-dimensional (2D and 3D) correlation experiments, which involve at least one $^1$H dimension with CRAMPS-quality resolution and utilize the spectral range, sensitivity and RF flexibility offered by fast MAS probes.

In spite of the importance of the homonuclear decoupling techniques, their widespread use by the scientific community has been affected by the experimental challenges involved in the setup and optimization. Early CRAMPS experiments, which used homebuilt RF circuitry and probes, were intricate due to rigorous requirements on pulse shapes, phases, timing and RF homogeneity [19,20]. Extensive analyses have been dedicated to the practical aspects of the currently used PMLG and DUMBO sequences. Although the difficulties due to RF imperfections and instabilities have been largely overcome in present-day spectrometers, practical implementation of $^1$H homonuclear decoupling remains demanding and time consuming. The performance of state-of-the-art sequences is defined by a number of parameters, most of which are difficult to predict a priori. In particular, the optimum RF

www.manaraa.com

amplitude for PMLG decoupling does not necessarily correspond to the LG condition [18,21]. More importantly, the decoupling deteriorates rapidly when the ratio $\psi = \nu_c/\nu_R$ (where $\nu_c = (\tau_c)^{-1}$) is near the so-called degeneracy conditions $n\nu_c = m\nu_R$ (n, m = 1, 2, …). The limitations imposed by these conditions on the experimental parameters strongly depend on the MAS rate [18].

One of the optimization strategies relies upon monitoring the effect of $^1$H decoupling on $^{13}$C spectra, e.g. of adamantane or alanine [6,22,23]. The suppression of $^1$H homonuclear dipolar interactions renders the $^1$H-$^{13}$C spin pairs equivalent to the AX system in solution [24,25], providing a sensitive probe of the decoupling efficiency and a good estimate of the scaling factor through the observation of *J*-multiplets. A more direct method involves acquisition of high-resolution 1D or 2D $^1$H-$^1$H spectra of a reference sample, usually glycine, which allows for optimization of the amplitude of the RF magnetic field $\nu_{RF}$ and the $\tau_c/\tau_R$ ratio [13,17,18,21,22,26,27], calibration of the effective field [26] and the scaling factor [23,26,27], optimization of the resonance offset, the pulse imperfections and the spectral artifacts [13, 21,27,28].

Recently, we studied the utility of $^1$H decoupling under fast MAS in $^{13}$C and $^1$H-detected through-bond heteronuclear correlation (HETCOR) experiments [29], where the best performance of PMLG and SAM3 sequences was found by minimizing the loss of signal due to transverse relaxation ($T_2'$) in a simple spin-echo experiment. Here, we will demonstrate that this strategy is of general practical relevance to high-resolution $^1$H spectroscopy. By monitoring the echo intensity for a fixed delay $\tau$, it is possible to quickly and reliably navigate through the complex space of experimental parameters and gauge the decoupling efficiency of the supercycled PMLG scheme as a function of $\nu_{RF}$, $\nu_R$, $\nu_c$, and the resonance offset without acquiring high-resolution spectra. The observed patterns are compared with those recently calculated by Vega et al. based on the bimodal Floquet theory [18]. We

www.manaraa.com

conclude by offering a tuning 'recipe', which affords simple and fast optimization of the homonuclear decoupling using directly the sample of interest.

### 4.3 Results and Discussion

*Resolution patterns*

The pulse sequences for spin-echo and 2D $^{1}$H-$^{1}$H correlation experiments are shown in Figure 4.1a and b. All experiments were performed using the supercycled PMLG scheme, denoted $PMLG5^{\bar{x}x}_{mm}$, which consists of two blocks $PMLG5^{x}_{m}$ and $PMLG5^{\bar{x}}_{m}$ with phase rotation as shown in Figure 4.1c [30].

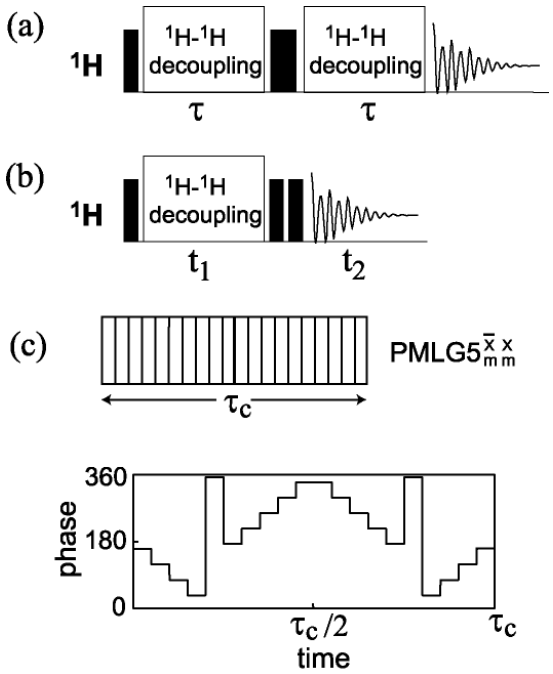


**Fig. 4.1**. Pulse sequences for (a) spin-echo experiment with $PMLG5^{\bar{x}x}_{mm}$ $^{1}$H homonuclear decoupling during τ, (b) 2D $^{1}$H-$^{1}$H correlation experiment using $PMLG5^{\bar{x}x}_{mm}$ decoupling in the indirect dimension, and (c) schematic representation of the $PMLG5^{\bar{x}x}_{mm}$ block.

www.manaraa.com

The contour plots shown in Figure 4.2a, b and c represent the intensities of spin-echoes observed for glycine (full rotor) using a constant $\tau$ value of approximately 2 ms, the carrier frequency at 4 ppm with respect to TMS, and three different PMLG5$^{\bar{x}x}_{mm}$ cycle periods $\tau_c$ of 50 μs ($\nu_c$ = 20 kHz), 32 μs ($\nu_c$ = 31.25 kHz) and 25 μs ($\nu_c$ = 40 kHz). Each plot consists of 2000 data points representing the total echo intensity, including the spinning sidebands, measured for 50 values of $\nu_{RF}$ and 40 values of $\nu_R$, the ranges of which are compatible with the theoretical results of Vega et al. (Figures 4.2 and 4.3 in reference [18]), within the capabilities of our Varian FastMAS$^{TM}$ probe. The results shown in Figure 4.2a, b and c (as well as those in Figure 4.3a and b, below) were obtained using rotor synchronization. Under such conditions, $\tau$ is not in general a multiple of $\tau_c$, in which case $^1$H decoupling is 'off' for a fraction of the rotor period on each side of the $\pi$ pulse. During these 'off' periods, which vary with $\tau_R$ and $\tau_c$, $^1$H magnetization evolves only under MAS. The resulting dephasing is insignificant at high MAS rates, especially when short $\tau_c$ values are used, but it can interfere with the optimization process at $\nu_R \leq 10$ kHz, at least for glycine. We should point out, however, that identical spin-echo patterns were observed without rotor synchronization. As noted in Section 2.2, at $\nu_R$ = 10 kHz, the non-synchronized patterns were in fact more reliable, at least in naturally abundant samples studied here.

There are clear similarities between the experimental and theoretical patterns. The left and right vertical lines in Figure 4.2a-c, which correspond to $\psi$ = 1 (i.e. $\nu_c = \nu_R$) and 2 ($\nu_c = 2\nu_R$) correspond to areas with the lowest echo intensity. The same areas were identified as most sensitive to the zero-order degeneracy conditions in the Floquet Hamiltonian. Other such areas correspond to $\psi$ = 1/2 and 2/3 in Figure 4.2a. Weak echo intensity has been also observed at $\psi$ = 3/2, as indicated by the central vertical line in Figure 4.2a-c. This coincides with the region of first-order degeneracy effect, where the decline in PMLG5$^{\bar{x}x}_{mm}$ decoupling was detected using numerical simulations [18]. Additional 'dips' in echo intensity observed

www.manaraa.com

for high MAS rates in Figure 4.2a are also due to first-order degeneracies, which are closely spaced for $\psi \leq 3/2$ (see Figure 4.3a, below).

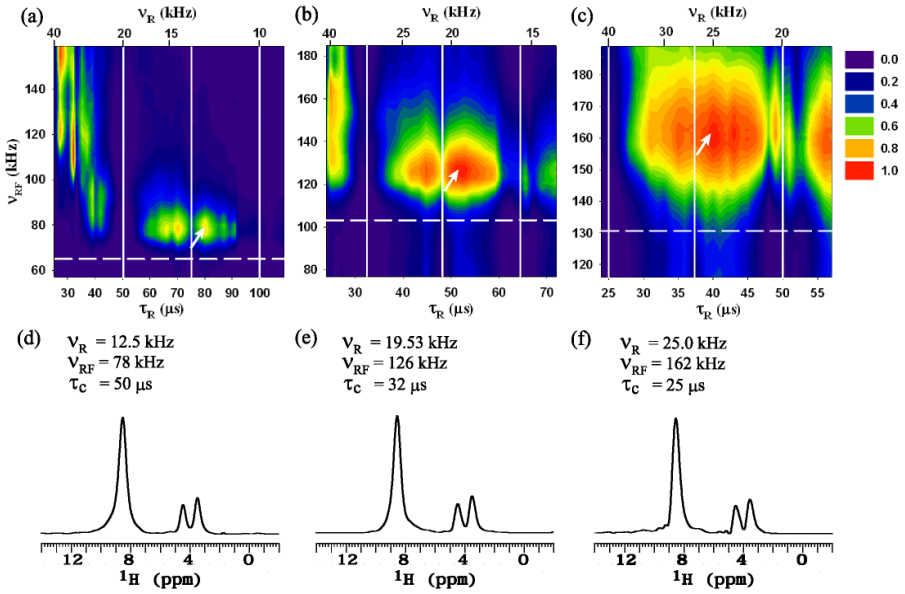


**Fig. 4.2**. The integrated intensity of spin-echo in glycine as a function of $\tau_R$ and $\nu_{RF}$, measured under PMLG5$^{\bar{x}x}_{mm}$ decoupling, with $\tau \cong 2$ ms, the carrier frequency set at 4 ppm from TMS, and $\tau_c$ = 50 μs (a), 32 μs (b) and 25 μs (c). The experiments were performed at 14.1 T on a Varian NMR System 600 MHz spectrometer, equipped with 1.6 mm triple-resonance MAS probe. The plots comprise 2000 points representing integrated intensity of the entire echo signal measured for 40 values of $\tau_R$ and 50 values of $\nu_{RF}$. Each signal consisted of 4 scans acquired using acquisition delay of 2s. Total measurement time was approximately 3 days per plot. The contours were normalized relative to the highest intensity observed in each plot. The vertical lines correspond from left to right to $\psi$ = 1, 3/2 and 2. The dashed line represents the LG value $\nu_{RF,LG} = 4\sqrt{2/3}\nu_c$. (d-f) The projections of indirect dimensions of 2D $^1$H-$^1$H correlation spectra measured using the $\nu_R$ and $\nu_{RF}$ values indicated by arrows in (a-c). Each spectrum was acquired in 160 rows, 8 scan per row, with $t_1$ increment of ~ 100 μs, and the total experiment time was 1.5 hrs.

www.manaraa.com

The spectra in Figure 4.2d, e and f represent high-resolution projections of the 2D $^{1}$H-$^{1}$H spectra measured under the conditions indicated by arrows in Figure 4.2a, b and c. Clearly, high quality decoupling has been achieved in all three spectra. These results show that the best refocusing has not been reached under the LG condition $\nu_{RF,LG} = 4\sqrt{2/3}\nu_c$, indicated by the dashed horizontal line in Figure 4.2a-c, but at the $\nu_{RF}$ values approximately 20% higher. Interestingly, these values are within ±3% of the theoretically determined maxima of decoupling efficiency (Figure 4.2a-c in reference [18]), which implies that the observed divergence is not due to inaccurate estimate of $\nu_{RF}$ or RF inhomogeneity. Note, however, that under MAS at 41.67 kHz, the best resolution was found at $\nu_{RF} < \nu_{RF,LG}$ (see below).

The $\psi$ values of 1.4 and 1.6 appear to be universally reliable, which in the case of fast MAS implies the use of high $\nu_c$ as well as high $\nu_{RF.}$ The parameter space associated with high echo intensity increases considerably with increasing $\nu_c$, which favors probes with excellent RF capabilities. In general, the decoupling efficiency depends on the proximity of these areas to $\nu_{RF,LG}$. The overall decoupling performance also depends on the scaling factor $s_f$, which is not discernible in the spin-echo experiment. As expected, the scaling factor is unrelated to $\nu_R$, with $\nu_c$ and $\nu_{RF}$ being constant. For any given set of $\nu_c$ and $\nu_R$, an increase of $\nu_{RF}$ lowers the scaling factor. For example, the spectra shown in Figure 4.2 have approximately the same value $s_f \cong 0.30$. Spectra of similar quality can be obtained within the 'red area' on the right side of Figure 4.2c, whereas the $s_f$ value is considerably reduced for the area of high echo intensity in the upper left part of Figure 4.2a.

www.manaraa.com

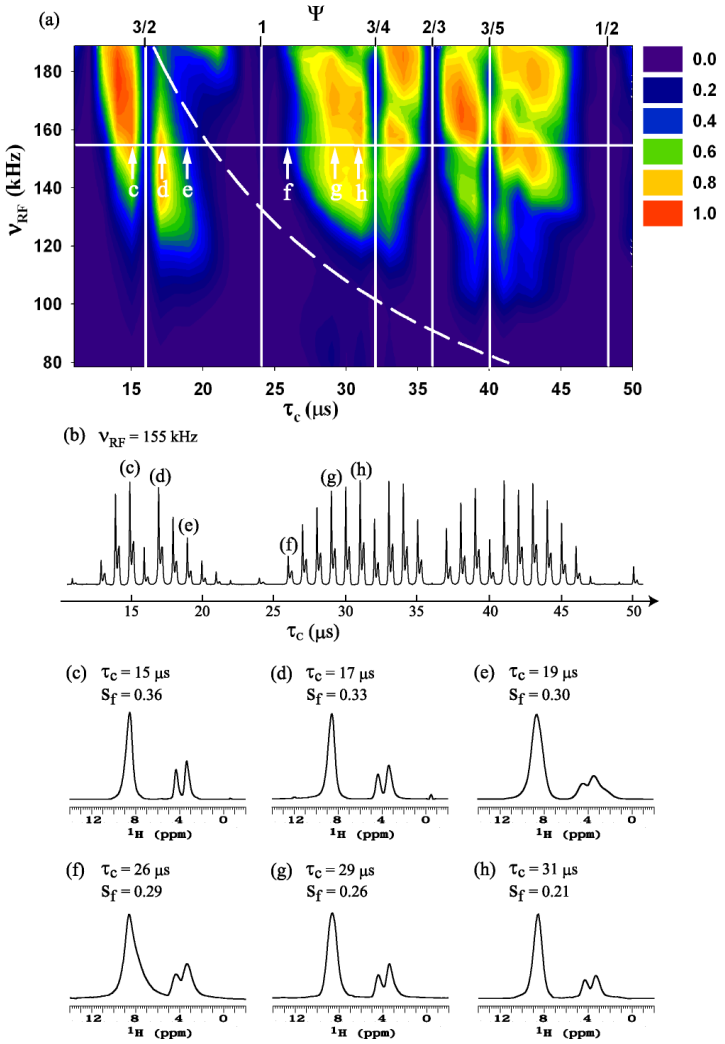


**Fig. 4.3**. (a) The integrated intensity of spin-echo in glycine as a function of $\tau_c$ and $\nu_{RF}$, measured under PMLG5$^{\bar{x}x}_{mm}$ decoupling, with $\tau \cong 2$ ms and $\tau_R = 24$ μs ($\nu_R = 41.67$ kHz). The plot consists of 1920 points representing integrated intensity of the entire echo signal measured for 40 values of $\tau_c$ and 48 values of $\nu_{RF}$. The dashed curve corresponds to the LG condition $\nu_{RF,LG}$ and the vertical lines to $\psi$ = 3/2, 1, 3/4, 2/3, 3/5 and 1/2. The measurement time was approximately 4 hours. (b) A series of 1D spectra measured for $\nu_{RF}$ = 155 kHz (horizontal line in (a)). (c-h) The projections of 2D $^1$H-$^1$H correlation spectra obtained under decoupling conditions marked in Figure 4.3a and b. Other experimental conditions were as given in the caption to Figure 4.2.

www.manaraa.com

Additional insights can be obtained by monitoring the echo intensity as a function of $\tau_c$ and $\nu_{RF}$, at a constant MAS rate. Figure 4.3a represents a contour plot measured at $\nu_R$ = 41.67 kHz ($\tau_R$ = 24 μs). Note that the slices at $\tau_c$ = 25, 32 and 50 μs match up closely with the left vertical edges of Figure 4.2a, b and c. The areas of low echo intensity include the entire bottom half of the figure ($\nu_{RF}$ < 140 kHz), the vicinity of LG condition, and the vertical strips corresponding to low $\psi$ values of 3/2, 1 (broad region), 3/4, 2/3, 3/5, and 1/2 (broad region).

The set of spectra in Figure 4.3b corresponds directly to the horizontal slice at $\nu_{RF}$ = 155 kHz (solid line in Figure 4.3a). The high-resolution $^1$H spectra shown in Figure 4.3c-h were measured under the conditions designated by (c), (d), (e), (f), (g) and (h) in Figure 4.3b. As a general rule, under constant $\nu_{RF}$ the scaling factor improves for short $\tau_c$ (see Figure 4.3c-h), and under constant $\tau_c$ for low $\nu_{RF}$, as noted earlier. Overall, the best performance is again observed around $\psi$ = 1.6 and 1.4 (Figure 4.3c and d), whereas experiments corresponding to low intensity echoes near $\nu_{RF,LG}$ (Figure 4.3e) or high intensity echoes further away from $\nu_{RF,LG}$ (Figure 4.3h) yield poor $^1$H resolution.

Finally, we show the effect of the resonance offset on spin-echo intensity and $^1$H resolution (Figure 4.4). Again, the decoupling efficiency can be easily assessed based on the echo intensity, although the effect of offset varies across each spectrum.

www.manaraa.com

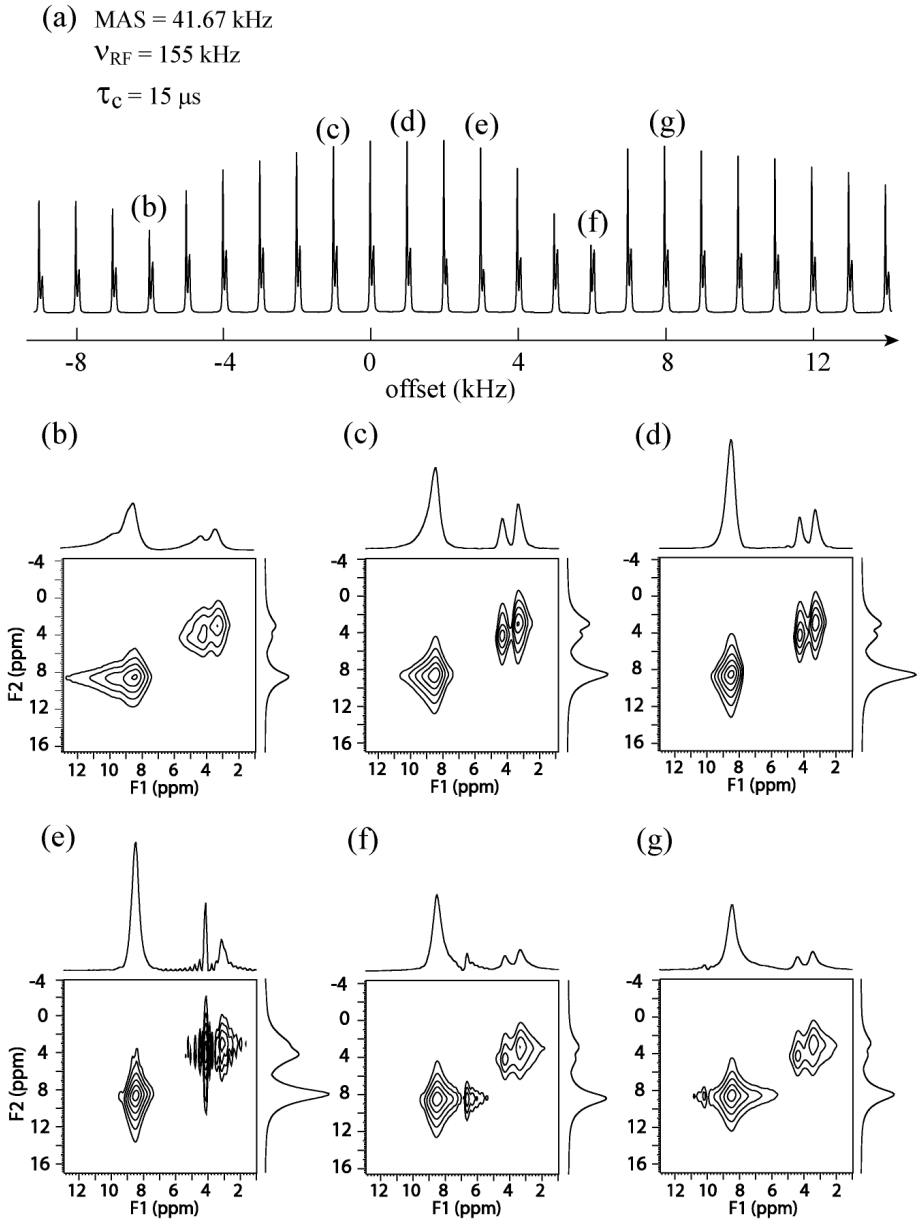


**Fig. 4.4**. (a) The spin-echo spectra of glycine as a function of resonance offset with respect to the carrier frequency used in previous measurements, set at 4 ppm from TMS. The experimental parameters were the same as for the spectrum shown in Figure 4.3c, which corresponds to offset equal zero. (b-g) 2D $^{1}$H-$^{1}$H correlation spectra measured under decoupling conditions marked in (a). Other experimental conditions were as given in the caption to Figure 4.2.

www.manaraa.com

*Simple optimization strategy*

The measurements shown in Figures 4.2 and 4.3, which took days and hours to acquire, respectively, are not needed in routine optimizations of the decoupling efficiency. The selection of proper experimental parameters ($\nu_R$, $\nu_{RF}$, $\nu_c$ and the resonance offset) can be done quickly and reliably by performing a very limited number of spin-echo experiments. The choice of $\nu_R$ is usually dictated by the research needs and probe capabilities, and we first assume the use of fast MAS, as required in HETCOR experiments at high magnetic fields. It is clear from Figure 4.3a that this implies the use of the strongest available RF field. The best value of $\nu_c$ must be correlated with $\nu_{RF}$ by the LG condition (roughly) and with $\nu_R$ via the constrains imposed by the $\psi$ ratio. We used the following steps:

(i) set $\nu_{RF}$ at 80-90% of the maximum 'safe' value for the probe and $\tau$ at around 2 ms,

(ii) measure a series of spin-echo spectra as a function of $\tau_c$ similar to that shown in Figure 4.3b,

(iii) choose the best value of $\tau_c$ (see below) and fine-tune $\nu_{RF}$ by arraying it around the starting value, and

(iv) use the best values of $\tau_c$ and $\nu_{RF}$ to optimize the offset, again by collecting a series of echoes.

We should remark that step (iii) may involve some ambiguity when comparable echo maxima are observed for different values of $\tau_c$, such as those marked (c) and (h) in Figure 4.3b. In such case the maximum associated with shorter $\tau_c$ is preferred, because it is associated with a higher scaling factor, as indeed confirmed in Figure 4.2c and h. A more methodical search can be initially carried out by the repeating steps (ii) and (iii) for several values of $\nu_{RF}$, but it is not needed once the routine is established. In samples studied in our laboratory (glycine, tripeptide f-MLF-OH and a series of coals) these tasks could be performed directly on the sample of interest within 20-30 minutes and invariably led to excellent resolution.

www.manaraa.com

As Figure 4.2 demonstrates, a similar strategy can be applied at lower MAS rates, down to at least 10 kHz. Rotor-synchronization should be avoided under slow MAS because the echo patterns observed as a function of $\tau_c$ (step (ii)) may become $\tau$-dependent due to the abovementioned difficulties with timing of the sequence.

## 4.4 Conclusion

The spin-echo measurement provides a quick and reliable method for optimization of $^1$H homonuclear decoupling without using a reference sample. Its utility has been confirmed at MAS rates above 10 kHz by excellent agreement of the observed efficiency patterns of the supercycled Lee-Goldburg sequence with earlier theoretical predictions and verified in high-resolution 2D $^1$H-$^1$H experiments. For this sequence, the best performance was observed when the ratio $\psi = \nu_c/\nu_R$ was approximately 1.4 or 1.6.

Although further studies are needed in order to better understand the relationship between transverse coherence lifetime of protons and the functioning of homonuclear decoupling, we expect that similar strategy can be used to optimize other homonuclear decoupling sequences, such as SAM and PMLG5$^x_m$ (which we verified, see Ref. [29]) or DUMBO, under windowed and windowless conditions. In sequences where the average Hamiltonian does not generate *z*-rotation, additional pulses before and after each decoupling block should be used to rotate the $^1$H magnetization into the *xy* plane.

## 4.5 Acknowledgment

The authors thank Dr. Shimon Vega for helpful discussions. This research was supported at the Ames Laboratory by the U.S. Department of Energy, Office of Basic Energy Sciences, under Contract No. DE-AC02-07CH11358.

## 4.6 References

www.manaraa.com

[1] M. Lee, W. Goldburg, Nuclear magnetic resonance line narrowing by rotating rf field, *Phys. Rev. A* 140 (1965) 1261-1271.

[2] J.S. Waugh, L.M. Huber, U. Haeberlen, WHH, Approach to high-resolution nmr in solids, *Phys. Rev. Lett.* 20 (1968) 180-183.

[3] W.K. Rhim, D.D. Elleman, R.W. Vaughan, Enhanced resolution for solid state NMR, *J. Chem. Phys.* 59 (1973) 1772-1773.

[4] D.P. Burum, W.K. Rhim, Analysis of multiple pulse NMR in solids, *J. Chem. Phys.* 71 (1979) 944-956.

[5] B.C. Gerstein, R.G. Pembleton, R.C. Wilson, L.M.J. Ryan, High resolution NMR in randomly oriented solids with homonuclear dipolar broadening: Combined multiple pulse NMR and magic angle spinning, *Chem. Phys.* 66 (1977) 361-362.

[6] A. Bielecki, A.C. Kolbert, M.H. Levitt, Frequency-switched pulse sequences – homonuclear decoupling and dilute spin NMR in solids, *Chem. Phys. Lett.* 155 (1989) 341-346.

[7] E. Vinogradov, P.K. Madhu, S. Vega, High-resolution proton solid-state NMR spectroscopy by phase-modulated Lee-Goldburg experiment, *Chem. Phys. Lett.* 314 (1999) 443-450.

[8] D. Sakellariou, A. Leasge, P. Hodgkinson, L. Emsley, Homonuclear dipolar decoupling in solid-state NMR using continuous phase modulation, *Chem. Phys. Lett.* 319 (2000) 253-260.

[9] P.K. Madhu, X. Zhao, M.H. Levitt, High-resolution $^{1}$H NMR in the solid state using symmetry-based pulse sequences, *Chem. Phys. Lett.* 346 (2001) 142-148.

[10] J.-P. Amoureux, B. Hu, J. Trebosc, Enhanced resolution in proton solid-state NMR with very fast MAS experiments, *J. Magn. Reson.* 193 (2008) 305-307.

[11] U. Haeberlen, J.S. Waugh, Coherent averaging effects in magnetic resonance, *Phys. Rev.* 175 (1968) 453-456.

www.manaraa.com

[12] M.H. Levitt, Symmetry in the design of NMR multiple-pulse sequences, *J. Chem. Phys.* 128 (2008) 052205.

[13] Leskes, P.K. Madhu, S. Vega, Supercycled homonuclear dipolar decoupling in solid-state NMR: Toward cleaner $^{1}$H spectrum and higher spinning rates, *J. Chem. Phys.* 128 (2008) 052309.

[14] E. Vinogradov, P.K. Madhu, S. Vega, Strategies for high-resolution proton spectroscopy, *Top. Curr. Chem.* 246 (2004) 33-99.

[15] A. Samoson, T. Tuherm, J. Past, A. Reinhold, T. Anupold, I. Heinmaa, New horizons for magic angle spinning NMR, *Top. Curr. Chem.* 246 (2005) 15-31.

[16] M. Leskes, S. Steuernagel, D. Schneider, P.K. Madhu, S. Vega, Homonuclear dipolar decoupling at magic angle spinning frequencies up to 65 kHz in solid-state nuclear magnetic resonance, *Chem. Phys. Lett.* 466 (2008) 95-99.

[17] E. Salager, R.S. Stein, S. Steuernagel, A. Lesage, B. Eléna, L. Emsley, Enhanced sensitivity in high-resolution $^{1}$H solid-state NMR spectroscopy with DUMBO dipolar decoupling under ultra-fast MAS, *Chem. Phys. Lett.* 469 (2009) 336-341.

[18] M. Leskes, P.K. Madhu, S. Vega, Why does PMLG proton decoupling work at 65 kHz MAS?, *J. Magn. Reson* 199 (2009) 208-213.

[19] B.C. Gerstein, C.R. Dybowski, Transient techniques in NMR in solids, Academic, New York, 1985.

[20] C.E. Bronnimann, B.L. Hawkins, M. Zhang, G.E. Maciel, Combined rotation and multiple pulse spectroscopy as an analytical proton nuclear magnetic resonance technique for solids, *Anal. Chem.* 60 (1988) 1743-1750.

[21] C. Coelho, J. Rocha, P.K. Madhu, L. Mafra, Practical aspects of Lee-Goldburg based CRAMPS techniques for high-resolution $^{1}$H NMR spectroscopy in solids: Implementation and applications, *J. Magn. Reson.*, 194 (2008) 264-282.

www.manaraa.com

[22] M.E. Stoll, A.J. Vega, R.W. Vaughan, Heteronuclear dipolar modulated chemical shift spectra for geometrical information in polycrystalline solids, *J. Chem. Phys.*, 65 (1976) 4093-4098.

[23] M. Leskes, P.K. Madhu, S. Vega, Proton line narrowing in solid-state nuclear magnetic resonance: New insights from windowed phase-modulated Lee-Goldburg sequence, *J. Chem. Phys.* 125 (2006) 124506.

[24] T. Terao, H. Miura, A. Saika, Measurements of the $^{13}C$-$^{1}H$ coupling constants in solid adamantane: resolution enhancement by multiple-pulse decoupling, *J. Magn. Reson.* 49 (1982) 365-367.

[25] B. Elena, G. de Paëpe, L. Emsley, Direct optimization of proton-proton homonuclear dipolar decoupling in solid-state NMR, *Chem. Phys. Lett.* 398 (2004) 532-538.

[26] A. Lesage, D. Sakellariou, S. Hediger, B. Eléna, P. Charmont, S. Steuernagel, L. Emsley, Experimental aspects of proton NMR spectroscopy in solids using phase-modulated homonuclear dipolar decoupling, *J. Magn. Reson.*, 163 (2003) 105-113.

[27] S. Paul, R.S. Thakur, M. Goswami, A.C. Sauerwein, S. Mamone, H. Förster, M.H. Levitt, P.K. Madhu, Supercycled homonuclear dipolar decoupling sequences in solid-state NMR, *J. Magn. Reson.* 197 (2009) 14-19.

[28] A. J. Vega, Controlling the effects of pulse transients and RF inhomegeneity in phase-modulated multiple-pulse sequences for homonuclear decoupling in solid-state NMR, *J. Magn. Reson.* 170 (2004) 22-41.

[29] K. Mao, M. Pruski, Directly and indirectly detected through-bond heteronuclear correlation solid-state NMR spectroscopy under fast MAS, *J. Magn. Reson.* 201 (2009) 165-174.

[30] M. Leskes, P.K. Madhu, S. Vega, A broad-banded z-rotation windowed phase-modulated Lee-Goldburg pulse sequence for $^{1}H$ spectroscopy in solid-state NMR, *Chem. Phys. Lett.*, 447 (2007) 370-374.

www.manaraa.com

# Chapter 5

# Conformations of Silica-Bound (Pentafluorophenyl)Propyl Groups Determined by Solid-State NMR Spectroscopy and Theoretical Calculations

Published in *J. Am. Chem. Soc.* 132 (2010) 12452-12457

Kanmi Mao, Takeshi Kobayashi, Jerzy W. Wiench, Hung-Ting Chen, Chih-Hsiang Tsai, Victor S.-Y. Lin, and Marek Pruski

## 5.1 Abstract.

The conformations of (pentafluorophenyl)propyl groups ($–CH_2–CH_2–CH_2–C_6F_5$, abbreviated as PFP), covalently bound to the surface of mesoporous silica nanoparticles (MSNs), were determined by solid-state NMR spectroscopy and further refined by theoretical modeling. Two types of PFP groups were described, including molecules in the prone position with the perfluorinated aromatic rings located above the siloxane bridges (PFP-p) and the PFP groups denoted as upright (PFP-u), whose aromatic rings do not interact with the silica surface. Two-dimensional (2D) $^{13}C$-$^{1}H$, $^{13}C$-$^{19}F$ and $^{19}F$-$^{29}Si$ heteronuclear correlation (HETCOR) spectra were obtained with high sensitivity on natural abundance samples using fast magic angle spinning (MAS), indirect detection of low-γ nuclei and signal enhancement by Carr-Purcell-Meiboom-Gill (CPMG) spin-echo sequence. 2D double-quantum (DQ) $^{19}F$ MAS NMR spectra and spin-echo measurements provided additional information about the structure and mobility of the pentafluorophenyl rings. Optimization of the PFP geometry, as well as calculations of the interaction energies and $^{19}F$ chemical shifts, proved very useful in refining the structural features of PFP-p and PFP-u functional groups on the silica surface. The prospects of using the PFP-functionalized surface to modify its properties (e.g., the

www.manaraa.com

interaction with solvents, especially water) and design new types of the heterogeneous catalytic system are discussed.

**5.2 Introduction**

In spite of a long history of organofluorine chemistry, fluorocarbons are of growing interest in academic studies and chemical industry [1-7]. Due to high electronegativity and low electron polarizability of fluorine, the physical and chemical properties of these compounds differ from their hydrocarbon analogs. They exhibit extremely weak intermolecular Van der Waals interactions, which gives rise to high volatility, low refractive index and small surface tension [8-9]. Accordingly, modification of surface by fluorocarbons can influence the surface wettability. Indeed, a monolayer of $CF_3(CF_2)_{10}CO_2H$ molecules on platinum produced a non-wettable surface with the lowest tension value (6 dyn/cm) ever reported [10]. Similarly, an 'ultrahydrophobic' surface was formed on the silicon wafer via layer-by-layer sequential adsorption of perfluorinated polyelectrolytes [11]. Several mesoporous silica materials with fluorocarbon-modified surfaces have been recently reported [12-14]. For example, Corma and colleagues synthesized a mesoporous silica material with immobilized perfluorosulfonic acid and used it as a catalyst for esterification and acylation. The studies have shown that the surface properties of mesoporous channels can be strongly influenced by the presence of fluorocarbons, even when the surface coverage is only a fraction of a monolayer.

The goal of the present study is to demonstrate that the fundamental properties of surface-bound fluorocarbon molecules can be investigated in unprecedented detail by using the advanced two-dimensional solid-state NMR experiments and theoretical calculations. Specifically, we focus on understanding the molecular structure and conformation of the surface-bound PFP groups in the mesoporous silica nanoparticles (MSNs). The NMR studies used newly developed schemes for enhancement of sensitivity under fast magic angle spinning (MAS), which enabled the detection of heteronuclear correlation (HETCOR)

www.manaraa.com

spectra of naturally abundant $^{13}C$ and $^{29}Si$ nuclei on the silica surface with exceptional sensitivity. The theoretical investigations provided invaluable assistance in refining the conformational details of two types of PFP species described by NMR.

**5.3 Material and Methods.**

*PFP-MSN Material*

The sample containing (pentafluorophenyl)propyl groups ($–CH_2–CH_2–CH_2–C_6F_5$) covalently bound to MSNs, referred to as PFP-MSN, was synthesized via the previously reported co-condensation method [12, 15-17]. A mixture of cetyltrimethylammonium bromide (1.0 g, 2.75 mmol), 2 M NaOH(*aq*) (3.5 ml, 7.0 mmol), and 480 ml $H_2O$ was stirred at 80 °C for 10 min, followed by the addition of tetraethoxysilane (TEOS, 5 ml, 22.4 mmol) and pentafluorophenyl propyltrimethoxysilane (0.58 ml, 2.24 mmol). The solution was maintained at 80 °C for 2 h and separated by filtration. The resulting product was sequentially washed with water, methanol, and dried under vacuum yielding 1.0 g of as-made PFP-MSN. The surfactant was removed using acid-extraction, by refluxing the as-made PFP-MSN in methanolic solution of hydrochloric acid (1.0 ml of *conc.* HCl in 100 ml MeOH) for 6 h. After filtration and extensive washing with water and methanol, 0.7 g of the surfactant-free PFP-MSN was obtained in the form of white fine powder [12].

The TEM micrograph of PFP-MSN (not shown) indicated that the particles had elliptical shape with an average length of 300 nm and an aspect ratio of 1.5-2. The parallel, cylindrical pores formed a hexagonal mesostructure, as further confirmed by powder XRD experiments. The measured BET surface area and the pore diameter were 844 ±10 $m^2/g$ and 2.2 ±0.2 nm, respectively. Based on the analysis of nitrogen adsorption, the mesopore volume was estimated at 0.75 $cm^3/g$.

*Solid-State NMR*

www.manaraa.com

Solid-state NMR experiments were performed on a Varian NMR System spectrometer, equipped with a 1.6-mm triple resonance FastMAS$^{TM}$ probe and operated at 599.6 MHz for $^{1}$H, 564.2 MHz for $^{19}$F, 150.8 MHz for $^{13}$C and 119.1 MHz for $^{29}$Si nuclei. The sample was packed in the MAS rotor after the exposure to ambient conditions in the laboratory. Several one-dimensional (1D) and two-dimensional (2D) experiments were used, including 1D MAS with direct polarization (DPMAS), spin-echo, 2D through-bond and through-space HETCOR NMR utilizing the refocused INEPT (INEPTR) and cross-polarization (CP), respectively, and 2D double-quantum (DQ) MAS NMR. To increase the sensitivity, the $^{1}$H-$^{13}$C and $^{19}$F-$^{13}$C HETCOR experiments were performed with indirect detection of heteronuclei ($^{13}$C) under fast MAS [19-21]. The pulse sequences used in the indirectly detected through-space and through-bond HETCOR experiments are analogous to those reported elsewhere [20-21]. The $^{19}$F-$^{29}$Si HETCOR spectra were acquired using cross-polarization and the Carr-Purcell-Meiboom-Gill (CPMG) refocusing of $^{29}$Si magnetization [22-23].

The experimental parameters are given in figure captions, using the following symbols: $\nu_R$ denotes the magic angle spinning (MAS) rate, $\nu_{RF}^{X}$ the magnitude of the RF magnetic field applied to X spins, $\tau_{CP}$ the cross-polarization time, $\tau_1$ and $\tau_2$ the delays used during refocused INEPTR, $\tau_{RR}$ the rotary resonance recoupling time, $N_{CPMG}$ the number of echoes used during the CPMG acquisition, $\tau_{CPMG}$ the time interval between $\pi$ pulses in the CPMG sequence, $\Delta t_1$ the increment of $t_1$ during 2D acquisition, NS the number of scans, $\tau_{RD}$ the recycle delay, and AT the total acquisition time of a 2D spectrum. The $^{1}$H, $^{13}$C and $^{29}$Si chemical shifts are reported using the $\delta$ scale and are referenced to TMS at 0 ppm. The $^{19}$F NMR spectra are referred to $CFCl_3$ ($\delta$ = 0 ppm), based on substitution of the secondary reference of NaF aqueous solution (-121.5 ppm) [24].

*Theoretical Calculations*

www.manaraa.com

The geometry of the PFP functional group inside the MSN was studied by theoretical calculations using $C_6F_6$ and Si-containing cluster models for the surface oxygen sites of the MSN, as described in Results and Discussion. The geometries of the models were first approximated by the MM2 level calculations and further refined with the quantum mechanical theory using the Firefly program package [25-26]. The quantum mechanical calculations were carried out at the Møller-Plesset second-order perturbation theory (MP2) level with the 6-311++G(d,p) basis set. The interaction energies in the optimized geometries were corrected for the basis set superposition error (BSSE) using the counterpoise method [27]. Density functional theory (DFT) calculations of the NMR tensors were carried out at the B3LYP level using ORCA program package [28]. An IGLO-II type basis set [29] was employed in the DFT calculations. Theoretical shieldings were transformed to relative chemical shifts δ by subtracting the calculated chemical shift of $CFCl_3$.

### 5.4 Results and Discussion

*Solid-State NMR*

The $^{29}$Si DPMAS spectrum of PFP-MSN (Figure 5.1) is dominated by resonance lines at around -113 and -104 ppm representing silicon sites $Q^4$ ((≡SiO–)$_4$**Si**) and $Q^3$ ((≡SiO–)$_3$**Si**(–OH)), respectively. The presence of peaks centered at around -70 and -60 ppm, which are assigned to silicon atoms in positions (SiO)$_3$**Si**R and (SiO)$_2$**Si**R (denoted as $T^3$ and $T^2$), shows that the organic groups are indeed covalently bound to the surface.[22] Based on integration of the $^{29}$Si DPMAS spectrum we estimated that 13 ± 2% of silicon atoms in this sample are bound to carbon, which corresponds to the PFP concentration of 1.2 mmol/g, or roughly 1 molecule per nm$^2$. This last estimate was made by assuming that the inner pore surface area in PFP-MSN constitutes 90% of the total surface area of 844 m$^2$/g. Since the footprint area of the PFP complex is ~0.6 nm$^2$, this concentration would correspond to surface coverage of around 60%, if all molecules assumed the prone position.

www.manaraa.com

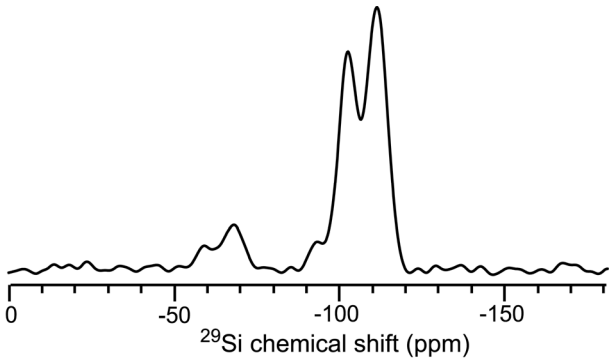


**Fig. 5.1**. $^{29}$Si DPMAS NMR spectrum of PFP-MSN taken under the following experimental conditions: $\nu_R$ = 10 kHz, $\nu_{RF}^{Si}$ = 86 kHz during short pulses, $\nu_{RF}^{H}$ = 45 kHz during TPPM decoupling, $N_{CPMG}$ = 25, $\tau_{CPMG}$ = 6 ms, $\tau_{RD}$ = 300 s and NS = 120.

With the static $^{1}$H and $^{19}$F linewidths being on the order of 10-20 kHz, the 2D HETCOR spectra of PFP-MSN could be best measured using the indirect detection of heteronuclei under fast MAS [19-21]. The indirectly detected, INEPTR-based $^{13}$C-$^{1}$H spectrum of PFP-MSN is shown in Figure 5.2a. The observed correlations between directly bound C1-H1, C2-H2 and C3-H3 pairs are consistent with the expected structure of the PFP groups covalently attached to the silica surface. Also observed is a resonance due to surface methoxy functionality, as shown in our earlier report [21]. The same correlations, as well as those due to long-range, through-space interactions between C2-H1, C2-H3 and C3-H2 are observed in the spectrum derived thorough space with $\tau_{CP}$ = 4.5 ms (Figure 5.2b). Also observed in Figure 5.2b is the correlation between H3 and the aromatic ring (carbon C4).

www.manaraa.com

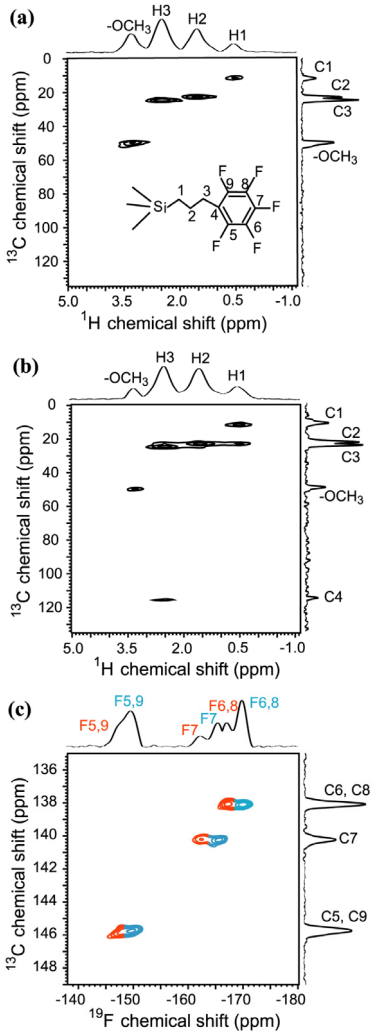


**Fig. 5.2**. 2D indirectly detected $^{13}$C-$^{1}$H (a,b) and $^{13}$C-$^{19}$F (c) spectra of PFP-MSN. Spectra (a) and (b), obtained using through-bond (INEPTR) and through-space (CP) mixing, were used in our earlier report on indirect detection.[21] They were recorded using $\nu_R$ = 40 kHz, $\nu_{RF}^H$ = 110 kHz during short pulses, $\nu_{RF}^H$ = 60 kHz during tangent ramp CP, $\nu_{RF}^H$ = 20 kHz during $\tau_{RR}$, $\nu_{RF}^C$ = 100 kHz during short pulses and CP, $\nu_{RF}^C$ = 10 kHz during SPINAL-64 decoupling, $\tau_{CP}$ = 4.5 ms, $\tau_1$ = 0.6 ms, $\tau_2$ = 0.8 ms, $\tau_{RR}$ = 80 ms, 160 rows with $\Delta t_1$ = 25 μs, 128 (a) and 48 (b) scans per row, $\tau_{RD}$ = 1.5 s, and AT = 12.5 h (a) and 4.5 h (b). Spectrum (c) was obtained using INEPTR under similar conditions, exclusive of $\tau_1$ = 1.0 ms, $\tau_2$ = 0.9 ms, 80 rows, $\Delta t_1$ = 200 μs, 400 scans per row, $\tau_{RD}$ = 0.8 s, and AT = 15.5 hr.

www.manaraa.com

In the $^{13}C$-$^{19}F$ HETCOR spectrum shown in Figure 5.2c, the aromatic carbons in PFP-MSN are observed through J couplings with the directly bound fluorines. The observed $^{13}C$ shifts are consistent with those expected for carbons C5-C9. Surprisingly, each $^{13}C$ resonance is involved in double cross-peaks along the $^{19}F$ dimension, labeled in red and blue in Figure 5.2c, representing fluorine sites with similar but discernible chemical shifts. This suggests the presence of two PFP functionalities, which reside on the silica surface in separate average environments and do not change on the time scale of $(\Delta\nu)^{-1} \cong 1$ ms (where $\Delta\nu$ is the difference between the corresponding $^{19}F$ resonance frequencies in both species). For reasons to be explained later, we denote the molecules represented by 'blue' and 'red' resonances as PFP-u and PFP-p.

The presence of two non-exchanging conformations of PFP is further verified by the 2D $^{19}F$-$^{19}F$ DQMAS measurement (Figure 5.3), which under the excitation and refocusing conditions used here (see figure caption) found only intramolecular correlations between $^{19}F$ nuclei, via the dipole-dipole coupling. In the DQ dimension, the signals representing two coupled nuclei resonating at $\omega_1$ and $\omega_2$ occur at the sum frequency $\omega_1 + \omega_2$, whereas the signals from non-interacting nuclei are suppressed by the DQ filtering [30]. Thus, the spatial proximities between $^{19}F$ nuclei can be identified by following the cross-peaks along the horizontal and vertical pathways, as shown in Figure 5.3 for PFP-p (solid lines) and PFP-u (dashed lines). In the PFP-p functional groups, correlations between all intramolecular neighbors are observed, including the diagonal cross-peaks F5-F9 and F6-F8, and the off-diagonal superpositions of (F5-F6)+(F8-F9) and (F7-F6)+(F7-F8). Similar spectral features are observed for PFP-u, except for the diagonal peaks F5-F9 and F6-F8, which barely exceed the noise level. The differences between relative intensities in $^{19}F$ projections in Figures 5.2c and 5.3 are insignificant because they result from different spin dynamics involved in $^{13}C$-$^{19}F$ HETCOR and $^{19}F$-$^{19}F$ DQ MAS experiments.

www.manaraa.com

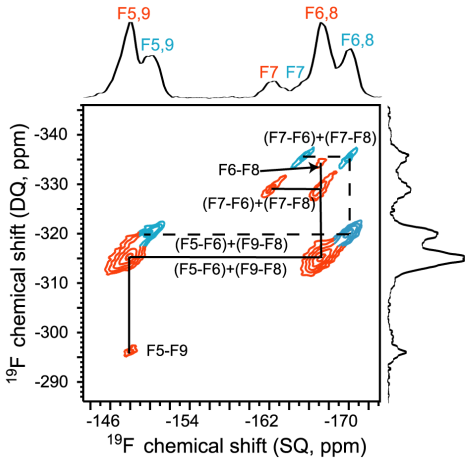


**Fig. 5.3**. 2D $^{19}$F-$^{19}$F DQMAS spectrum of PFP-MSN. The DQ excitation and reconversion was achieved using back-to-back (BABA) pulse sequence [31], $\nu_R$ = 40 kHz, $\nu_{RF}^F$ = 110 kHz, and excitation/reconversion length = 0.4 ms. The spectrum was acquired in 80 rows, with 128 scans per row, $\Delta t_1$ = 25 μs, $\tau_{RD}$ = 1 s, and AT = 6 hr.

To delineate the nature of PFP-p and PFP-u species, we probed their interaction with the silica surface, by measuring a 2D $^{19}$F-$^{29}$Si HETCOR spectrum of PFP-MSN (Figure 5.4). The measurement was enabled by using the CPMG refocusing of $^{29}$Si magnetization [22], which afforded a six-fold sensitivity gain (note that without the CPMG refocusing this spectrum would require two months of acquisition time). Notwithstanding the fact that both PFP-p and PFP-u were present in the sample, as evidenced by the $^{19}$F MAS spectrum shown along the $\omega_1$ dimension, the only observed $^{19}$F-$^{29}$Si correlations are associated with the PFP-p species. This demonstrates that the difference between PFP-p and PFP-u functional groups is in their interaction with the surface to which both are covalently bound. All $^{19}$F nuclei in PFP-p groups correlate with $Q^3$ and $Q^4$ silicon sites, which indicates that they reside in prone positions with respect to the silica surface and are less mobile. The lack of $^{19}$F-$^{29}$Si polarization transfer from the PFP-u species suggests that their aromatic rings are not located near the surface. The increased mobility of the PFP-u species may further contribute to

www.manaraa.com

weakening of the $^{19}F$-$^{29}Si$ dipole-dipole interactions (see the discussion of relaxation data and static NMR spectrum, below). No correlations involving the *T* sites and the aromatic ring were detected.

The $^{13}C$-$^{19}F$ HETCOR spectrum of Figure 5.2c shows that the interaction with the surface shifts the $^{19}F$ resonances in PFP-p by 2 to 3 ppm in the direction of higher frequency (less shielded) with respect to PFP-u molecules, but has a very small effect (<0.1 ppm) on the $^{13}C$ chemical shifts. An earlier study showed that adsorption of fluoroaromatic molecules (hexafluorobenzene, $C_6F_6$) on the surface of alumina has a deshielding effect on the $^{19}F$ nuclei compared to the same molecules in the gas phase [32].

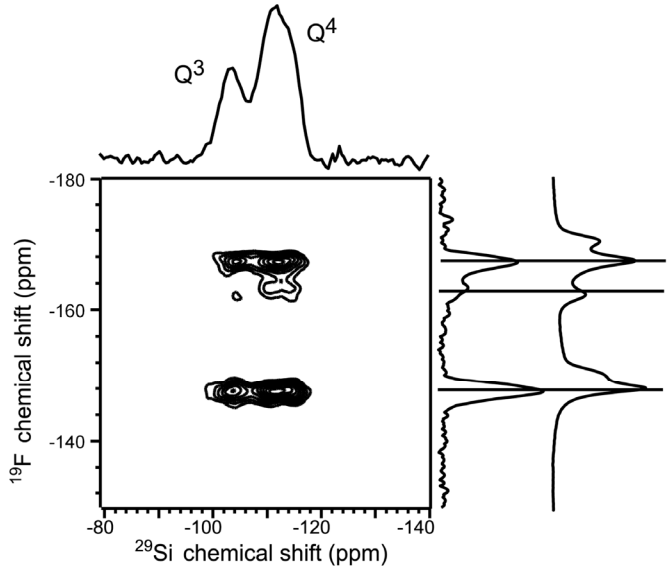


**Fig. 5.4**. 2D $^{19}F$-$^{29}Si$ CP-based CPMG-HETCOR spectrum of PFP-MSN obtained using $\nu_R$ = 40 kHz, $\nu_{RF}^{F}$ = 110 kHz during short pulses, $\nu_{RF}^{F}$ = 60 kHz during tangent CP, $\nu_{RF}^{Si}$ = 100 kHz during short pulses and CP, $\tau_{CP}$ = 20 ms, $N_{CPMG}$ = 250 and $\tau_{CPMG}$ = 4 ms. The data were acquired in 40 rows, with $\Delta t_1$ = 25 μs, 2000 scans per row, $\tau_{RD}$ = 0.8 s, and AT = 47 hr. Also shown is the corresponding 1D $^{19}F$ MAS spectrum.

www.manaraa.com

Further corroboration of these assignments was obtained by measuring the transverse relaxation time ($T_2$') of $^{19}$F nuclei under the spin-echo sequence π/2 - τ - π - τ - detect. The $T_2$' values obtained under fast MAS for PFP-u exceeded those for PFP-p by a factor of ~8 (12 ms versus 1.5 ms). Indeed, the spectra in Figure 5.5 show that nuclei in PFP-u and PFP-p were refocused with τ = 0.1 ms, but only those in PFP-u were observed with τ = 2 ms, which is consistent with the increased mobility. The existence of two populations of PFP species with different mobilities can be also inferred from the analysis of static $^{19}$F NMR spectrum (not shown) consisting of two superimposed components with the linewidths of 16 ± 2 kHz and 6 ± 1 kHz, which are mainly due to homonuclear $^{19}$F-$^{19}$F dipolar interactions. This is a crude approximation, as each component is a superposition of 3 resonances representing F5,9, F6,8 and F7. Still, these values are close, respectively, to those expected for perfluotinated rings that are rigid (PFP-p) and undergo limited motion, such as librational rotation (PFP-u). Note, however, that such mobility alone should not prevent the PFP-u species from being observed in the 2D $^{19}$F-$^{29}$Si HETCOR spectrum.

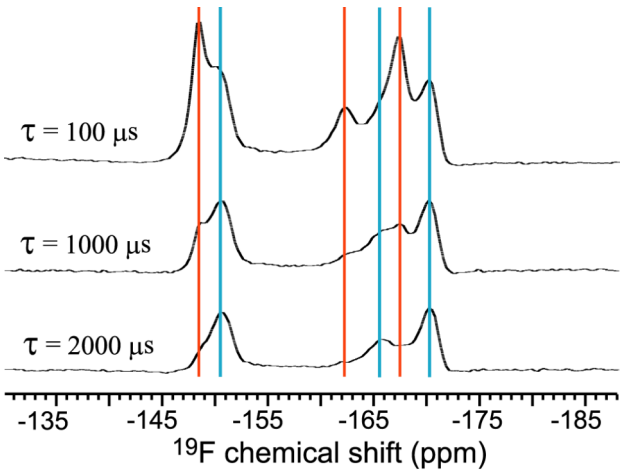


**Fig. 5.5**. $^{19}$F spectra of dried PFP-MSN obtained under MAS at 40 kHz using the spin-echo sequence with $\tau$ = 0.1, 1.0 and 2.0 ms.

www.manaraa.com

In short, solid-state NMR spectroscopy provided ample evidence for the existence of two distinct populations of PFP functional groups in the MSNs, both of which are covalently bound to the surface, have the same bond structure, but reside in positions described as 'prone' (PFP-p) and 'upright' (PFP-u) inside the mesopores. The NMR data provide several additional insights about the physicochemical nature of these species. The existence of separate sets of $^{19}F$ peaks representing both species shows that they do not change their conformations on the NMR time scale of ~1 ms. Based on the $^{19}F$-$^{29}Si$ CP efficiency, we can estimate that the PFP-p groups are located within ~0.45 nm from the nearest $Q^3$ and $Q^4$ silicon sites. This is a rough estimate, based on the maximum CP intensity being observed at $\tau_{CP}$ = 20 ms and the assumption that the CP dynamics for an rigid pair of spins reaches maximum at $\tau_{CP,opt}$ = 1.7/D, where the dipolar coupling D depends on the internuclear distance [33].

*Theoretical Modeling*

To propose a model of the geometry of the PFP-p species inside the MSNs, we support the solid-state NMR results with theoretical calculations. We point out that the surface of mesoporous silica comprises a complex network of *Q* and *T* sites with widely distributed ranges of $^{29}Si$ chemical shifts, which reflect their diverse local environments. Our aim is to put forth a simplified model that incorporates the basic chemical properties of the PFP-MSN surface and is consistent with both experimental and theoretical studies. Earlier *ab initio* studies of the interaction between an isolated pair of water and $C_6F_6$ molecules have shown that $C_6F_6$ can act as a lone-pair acceptor and interact with the oxygen center of $H_2O$ forming a dimer with a binding energy of about -8 kJ/mol [34]. Due to the electron-withdrawing effect of the fluorine atoms and the resulting electron deficiency of the $C_6F_6$ aromatic π-system, the oxygen of water is located approximately 0.32 nm from the center of the molecule, with both hydrogen atoms pointing away from the ring. This is in contrast to water-benzene interaction, which leads to a different π-electron distribution and results in

www.manaraa.com

formation of a weak hydrogen bond with water, such that both hydrogen atoms point toward the ring [34]. Following the Lewis's acid and base concept, in the $C_6F_6$-$H_2O$ system the oxygen atom acts as a Lewis base and the aromatic ring may exhibit Lewis acidity, whereas in $C_6H_6$-$H_2O$ system water plays the role of an acid. These properties of the PFP functional groups are relevant to surface science and catalysis, as will be pointed out in the Conclusion.

The abovementioned *ab initio* studies of the $C_6F_6$-$H_2O$ system [34] evoke a possibility that pentafluorophenyl groups of the PFP functionalities act in a similar fashion as a lone-pair acceptor and interact with the oxygen atom of the MSN surface. We have optimized the geometries of $C_6F_6$ interacting with two major oxygen species on the MSN surface: the oxygen atoms of silanol groups, H**O**–Si(–OSi≡)$_3$, and siloxane bridges, (≡SiO–)$_3$Si–**O**–Si(–OSi≡)$_3$. The surface models for these species were created based on β-cristobalite structure (Si–O bond length = 0.161 nm and Si–O–Si bond angle = 146.4°) [35-36], because the local structure of MSN is similar to that of amorphous silica [37-38] and X-ray work on amorphous silicas suggests that their structure most closely resembles that of β-cristobalite [39]. The Si–O– H bond angle was initially set to 121° [40]. The silicon atoms that do not carry the full complement of hydroxyl or siloxane bridges were terminated by hydrogen atoms. The structure of the Si-containing clusters was fixed during the optimization, except for the OH moieties of the silanol groups. The resulting geometries of the $C_6F_6$-silanol and $C_6F_6$-siloxane environments are shown in Figure 5.6. In both structures, the center of the $C_6F_6$ molecule appears to be located near the oxygen atom.

www.manaraa.com

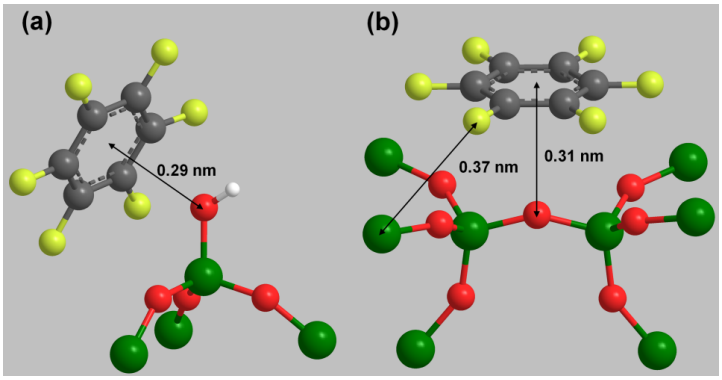


**Fig. 5.6.** The optimized geometries of (a) $C_6F_6$-silanol and (b) $C_6F_6$-siloxane models. Silicon atoms are green, oxygen atoms are red, carbon atoms are gray, fluorine atoms are yellow, and hydrogen atom is white. Silanol hydrogen is the only one shown.

In the optimized $C_6F_6$-silanol geometry (Figure 5.6a), the distance between the oxygen atom and the center of mass of the aromatic ring and the interaction energy are calculated to be $d$ = 0.29 nm and $\Delta E$ = -5.6 kJ/mol, respectively. Furthermore, five fluorine atoms of the $C_6F_6$ are separated from the nearest silicon atom ($Q^3$ site) by more than the NMR estimate (0.45 nm). The hydrogen bonds between the surface silanols and the fluorine atoms do not seem to form on the silica surface, which is consistent with the previous studies of the $C_6F_6$-$H_2O$ system [34]. This result is not surprising, because fluorine that bonds to $sp^2$ carbon is a poor hydrogen-bond acceptor [40]. The geometry shown in Figure 5.6a suggests that on 'real' MSN surface the $C_6F_6$-silanol interaction can be affected by steric hindrance within the system. Furthermore, fast librational motions of the silanol OH moieties [40] make it difficult for the aromatic ring and the silanol oxygen to interact with each other.

An optimized geometry of the $C_6F_6$-siloxane system is shown in Figure 5.6b. In this case, the $C_6F_6$ molecule lies flat above the siloxane oxygen at a distance of $d$ = 0.31 nm with all fluorine atoms having one or more neighboring silicon atoms within 0.45 nm. The computed interaction energy ($\Delta E$ = -11.0 kJ/mol) is larger than that for the $C_6F_6$-silanol model. The mobility of the $C_6F_6$ molecule under such conditions is expected to be limited.

www.manaraa.com

The $C_6F_6$-siloxane system is further studied by theoretical calculation of the $^{19}F$ chemical shift. The computation of the $^{19}F$ chemical shift of an isolated $C_6F_6$ molecule yielded -165.2 ppm, which is close to the reported value in the gas phase (-167.75 ppm) [32]. The $^{19}F$ chemical shift of the $C_6F_6$ molecule in the optimized $C_6F_6$-siloxane system was calculated to be -155.9 ppm (average of all six fluorine atoms), which demonstrates that the interaction of $C_6F_6$ molecules with the siloxane oxygen has a deshielding effect on the $^{19}F$ nuclei compared to the $C_6F_6$ in the gas phase. This deshielding effect is in agreement with $^{19}F$ NMR data, although its size exceeds the experimental value of ~3 ppm. However, on the 'real' surface, the aromatic ring of the PFP-p species is not located in the geometry where it maximally interacts with the siloxane oxygen because of the constraints imposed by the propyl chain, as well as the physical topology and chemical structure (e.g., concentration of silanol groups) of the MSN surface. Besides, even the PFP-u species are not truly isolated in the narrow pore of the MSN materials. Thus, the difference in $^{19}F$ chemical shifts between PFP-p and PFP-u is likely to be smaller than that calculated for the $C_6F_6$-siloxane model.

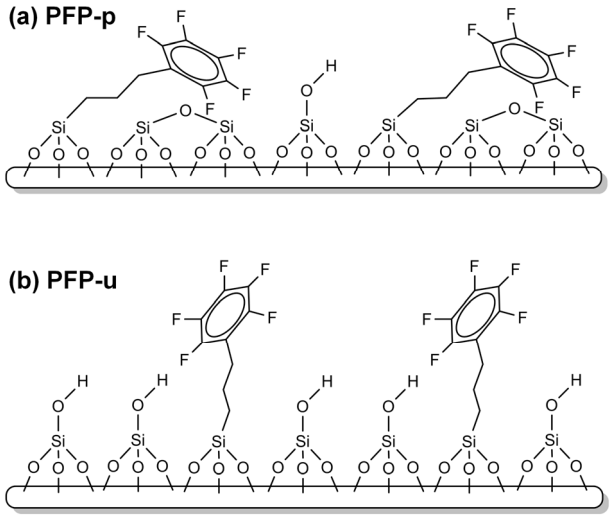


**Fig. 5.7.** The schematic representation of (a) PFP-p and (b) PFP-u functional groups on the silica surface. The aromatic rings of PFP-p interact with the siloxane oxygen, whereas those in PFP-u are located further from the surface and are more mobile.

www.manaraa.com

The theoretical calculations suggest that a feasible model representing the PFP-p species is one in which the aromatic ring of the PFP group is located above the siloxane oxygen in parallel to the MSN surface (Figure 5.7a). This geometry is consistent with the following NMR results: (1) all $^{19}F$ nuclei in PFP-p groups are located within ~0.45 nm from the nearest $Q^3$ and $Q^4$ silicon sites, (2) the mobility of the ring is restricted compared to PFP-u, (3) the $^{19}F$ nuclei of the PFP-p are deshielded by the interaction with silica. Due to the abovementioned constraints, only a fraction of the PPF groups can be located above the siloxane oxygen as PFP-p, whereas the others are confined to PFP-u positions. The most likely structure of PFP-u is shown in Figure 5.7b. We should emphasize that the designation of PFP-u molecules as 'upright' does not imply that they assume rigid vertical position on the surface. The NMR data showed reduced $^{19}F$ linewidth and slower transverse relaxation in PFP-u, most likely as a result of librational flips or rotations. Whereas this mobility may slow down the $^{19}F$-$^{29}Si$ CP process, the absence of resonances representing PFP-u in the $^{19}F$-$^{29}Si$ HETCOR spectrum and the change in $^{19}F$ chemical shifts demonstrate that these species are more distant from the MSN surface than PFP-p.

**5.5 Conclusion**

The NMR results and the theoretical calculations presented in this study showed that the PFP-MSN material hosts two types of covalently bound PFP species with similar bond topologies but different conformations: the PFP-p groups with the aromatic rings located above the surface siloxanes the PFP-u molecules in the roughly upright position. The fundamental understanding of the catalyst surface provided by this investigation can be used to enhance the catalytic performance in a predictable way. The interaction energy calculated for the $C_6F_6$-siloxane model system is larger than the adsorption energy of water molecules to dehydrated surface of a mesoporous silica material at low vapor pressure.[42] Since surface siloxanes of MSN materials are easily hydrolyzed to form silanols by water adsorption even

www.manaraa.com

at room temperature [43-44], keeping the hydrophobic character of these materials by protecting the siloxanes from water should be beneficial for their catalytic applications.

Indeed, in a forthcoming publication we will report on the design of a bifunctional MSN-based catalyst containing an acidic catalytic site and PFP functionalities for an esterification reaction. The presence of PFP improved considerably the catalytic performance, which is attributed to efficient expulsion of the byproduct (water) from the PFP-coated mesochannels. Further experimental and theoretical investigations are underway to describe the behavior of the PFP functional groups on the MSN surfaces in the presence of solvents.

### 5.6 Acknowledgment

This research was supported at the Ames Laboratory by the U.S. Department of Energy, Office of Basic Energy Sciences, under Contract No. DE-AC02-07CH11358. We would also like to thank the U.S. Department of Energy, Office of Energy Efficiency and Renewable Energy (grant no.: DE-FG26-0NT08854) for financial support.

### 5.7 References

[1] D.P. Curran, Strategy-level separations in organic synthesis: From planning to practice, *Angew. Chem., Int. Ed.*, 37 (1998) 1175-1196.

[2] W. Zhang, and D.P. Curran, Synthetic applications of fluorous solid-phase extraction (F-SPE), *Tetrahedron*, 62 (2006) 11837-11865.

[3] W.R. Dolbier, Fluorine chemistry at the millennium, *J. Fluorine Chem*., 126 (2005) 157-163.

[4] D.M. Lemal, Perspective on fluorocarbon chemistry, *J. Org. Chem.*, 69 (2004) 1-11.

[5] K. Uneyama, *Organofluorine Chemistry*; Wiley-Blackwell: Oxford UK, 2006.

www.manaraa.com

[6] R.E. Banks, B.E. Smart, and J.C. Tatlow, *Organofluorine Chemistry: Principles and Commercial Applications*; Springer: New York, 1994.

[7] T. Hiyama, *Organofluorine Compounds: Chemistry and Applications*; Springer: New York, 2000.

[8] D.F. Persico, R.J. Lagow, L.C. Clark, and H.-N Huang, A general-synthesis for symmetrical highly branched perfluoro ethers – a new class of oxygen carriers, *J. Org. Chem.*, 50 (1985) 5156-5159.

[9] D.S.L. Slinn, and S.W. Green, In *Properties and Industrial Applications of Organofluorine Compounds*; Banks, R. E., Ed.; Ellis Horwood: Chichester, 1982, pp45-82.

[10] E.F. Hare, E.G. Shafrin, and W.A. Zisman, Properties of films of adsorbed fluorinated acids, *J. Phys. Chem.*, 58 (1954) 236-239.

[11] R.M. Jisr, H.H. Rmaile, and J.B. Schlenoff, Hydrophobic and ultrahydrophobic multilayer thin films from perfluorinated polyelectrolytes, *Angew. Chem., Int. Ed*., 44 (2005) 782-785.

[12] R. Kumar, H.-T. Chen, J.L.V. Escoto, V.S.Y. Lin, and M Pruski, Template removal and thermal stability of organically functionalized mesoporous sillca nanoparticles, *Chem. Mater*., 18 (2006) 4319-4327.

[13] M. Alvaro, A. Corma, D. Das, V. Fomes, and H. Garcia, "Nafion"-functionalized mesoporous MCM-41 silica shows high activity and selectivity for carboxylic acid esterification and Friedel-Crafts acylation reactions, *J. Catal*., 231 (2005) 48-55.

[14] M. Alvaro, A. Corma, D. Das, V. Fomes, and H. Garcia, Single-step preparation and catalytic activity of mesoporous MCM-41 and SBA-15 silicas functionalized with perfluoroalkylsulfonic acid groups analogous to Nafion (R), *Chem. Commun*., (2004) 956-957.

[15] H.T. Chen, S. Huh, and V.S.Y. Lin, In *Catalyst Preparation*; J. Regalbuto Ed.; CRC Press, 2007, pp 45-74.

www.manaraa.com

[16] H.T. Chen, S. Huh, J.W. Wiench, M. Pruski, and V.S.Y. Lin, Dialkylaminopyridine-functionalized mesoporous silica nanosphere as an efficient and highly stable heterogeneous nucleophilic catalyst, *J. Am. Chem. Soc.*, 127 (2005) 13305-13311.

[17] S. Huh, H.T. Chen, J.W. Wiench, M. Pruski, and V.S.Y. Lin, Cooperative catalysis by general acid and base bifunctionalized mesoporous silica nanospheres, *Angew. Chem., Int. Ed.*, 44 (2005) 1826-1830.

[18] S. Huh, H.T. Chen, J.W. Wiench, M. Pruski, and V.S.Y. Lin, Controlling the selectivity of competitive nitroaldol condensation by using a bifunctionalized mesoporous silica nanosphere-based catalytic system, *J. Am. Chem. Soc.*, 126 (2004) 1010-1011.

[19] Y. Ishii and R. Tycko, Sensitivity enhancement in solid state $^{15}$N NMR by indirect detection with high-speed magic angle spinning, *J. Magn. Reson.*, 142 (2000) 19-204.

[20] J.W. Wiench, C.E. Bronnimann, V.S.-Y. Lin, and M. Pruski, Chemical Shift Correlation NMR Spectroscopy with Indirect Detection in Fast Rotating Solids: Studies of Organically Functionalized Mesoporous Silicas, *J. Am. Chem. Soc.,* 129, (2007) 12076-12077.

[21] K. Mao, J.W. Wiench, V.S.-Y. Lin, and M. Pruski, Indirectly detected through-bond chemical shift correlation NMR spectroscopy under fast MAS: Studies of organic-inorganic hybrid materials, *J. Magn. Reson.*, 196 (2009) 92-95.

[22] J.W. Wiench, V.S.-Y. Lin, and M. Pruski, $^{29}$Si NMR in Solid State with CPMG Acquisition under MAS, *J. Magn. Reson*., 193 (2008) 233-242.

[23] J. Trebosc, J. W. Wiench, S. Huh, V. S. Y. Lin, M. Pruski, Studies of Organically Functionalized Mesoporous Silicas Using Heteronuclear Solid-State Correlation NMR Spectroscopy under Fast Magic Angle Spinning, *J. Am. Chem. Soc.* 127 (2005) 7587-7593.

[24] E.Y. Chekmenev, S.K. Chow, D. Tofan, D.P. Weitekamp, B.D. Ross, and P. Bhattacharya, Fluorine-19 NMR chemical shift probes molecular binding to lipid membranes, *J. Phys. Chem. B.* 112 (2008) 6285-6287.

www.manaraa.com

[25] Granovsky, A. A., Firefly version 7.1.G, http://classic.chem.msu.su/gran/firefly/index.html

[26] M.W. Schmidt, K.K. Baldridge, J.A. Boatz, S.T. Elbert, M.S. Gordon, J.H. Jensen, S. Koseki, N. Matsunaga, K.A. Nguyen, S.J. Su, T.L. Windus, M. Dupuis, and J.A. Montgomery, General atomic and molecular electronic-structure system, *J. Comp. Chem.,* 14 (1993) 1347-1363.

[27] S.F. Boys, and F. Bernardi, Calculation of small molecular interactions by differences of separate total energies – some procedures with reduced errors, *Mol. Phys.*, 19 (1970) 553-566.

[28] F. Nesse, *ORCA-An Ab initio, DFT and Semiempirical Electronic Structure Package*, Ver. 2.7.0., 2010.

[29] W. Kutzelnigg, U. Fleischer, and M. Schindler, The IGLO-Method: Ab Initio Calculation and Interpretation of NMR Chemical Shifts and Magnetic Susceptibilities.; In Springer-Verlag: Heidelberg, 1990; Vol. 23.

[30] S. P., Brown and H. W. Spiess, Advanced solid-state NMR methods for the elucidation of structure and dynamics of molecular, macromolecular, and supramolecular systems, *Chem. Rev.*, 101 (2001) 4125-4155.

[30] M. Feike, D.E. Demco, R. Graf, J. Gottwald, S. Hafner, and H.W. Spiess, Broadband multiple-quantum NMR spectroscopy, *J. Magn. Reson. A*, 122 (1996) 214-221.

[32] V. L. Budarin, J. H. Clark, S. E. Hale, S. J. Tavener, K. T. Mueller, and N. M. Washton, NMR and IR study of fluorobenzene and hexafluorobenzene adsorbed on alumina, *Langmuir*, 23 (2007) 5412-5418.

[33] J.-P. Amoureux, and M. Pruski, Theoretical and experimental assessment of single- and multiple-quantum cross-polarization in solid-state NMR, *Mol. Phys.*, 100 (2002) 1595-1613.

[34] Y. Danten, T. Tassaing, and M. Besnard, On the nature of the water-hexafluorobenezne interaction, *J. Phys. Chem*. A, 103 (1999) 3530-3534.

www.manaraa.com

[35] T. Shimura, H. Misaki, M. Umeno, I. Takahashi, and J. Harada, X-ray diffraction evidence for the existence of epitaxial microcrystallites in thermally oxidized $SiO_2$ thin films on Si(111) surfaces, *J. Cryst. Growth,* 166 (1996) 786-791.

[36] D.R. Peacor, Hight Temperature Single-Crystal Study of Cristobalite Inversion, *Z. Kristall*, 138 (1973) 274-298.

[37] J.S. Beck, J.C. VartUli, W.J. Roth, M.E. Leonowicz, C.T. Kresge, K.D. Schmitt, T-W. Chu, D.H. Olson, E.W. Sheppard, S.B. McCullen, J.B. Higgins, and J.L. Schlenker, A New Family of Mesoporous Molecular Sieves Prepared with Liquid Crystal Templates, *J. Am. Chem. Soc*., 114 (1992) 10834-10843.

[38] K.J. Edler, P.A. Reynolds, and J.W. White, Small-Angle Neutron Scattering Studies on the Mesoporous Molecular Sieve MCM-41, *J. Phys. Chem.* B, 102 (1998) 3676-3683.

[39] C. Frondel, Crystalline Silica Hydrates from leached Silicates, *Am. Miner*., 64 (1979) 799-804.

[40] T. Kobayashi, J.A. DiVerdi, and G.E. Maciel, Silica Gel Surface: Molecular Dynamics of Surface Silanols, *J. Phys. Chem. C*, 112 (2008) 4315-4326.

[41] J.A.K. Howard, V.J. Hoy, D. Ohagan, and G.T. Smith, How good is fluorine as a hydrogen bond acceptor, *Tetrahedron*, 52 (1996) 12613-12622.

[42] A. Cauvel, D. Brunel, F. DiRenzo, E. Garrone, and B. Fubini, Hydrophobic and Hydrophilic Behavior of Micelle-Templated mesoporous Silica, *Langmuir,* 13 (1997) 2773-2778.

[43] A. Matsumoto, T. Sasaki, N. Nishimiya, and K. Tsutsumi, Evaluation of the hydrophobic properties of mesoporous FSM-16 by means of adsorption calorimetry, *Langmuir*, 17 (2001) 47-51.

[44] A. Matsumoto, K. Tsutsumi, K. Schumacher, and K.K. Unger, Surface functionalization and stabilization of mesoporous silica spheres by silanization and their adsorption characteristics, *Langmuir*, 18 (2002) 4014-4019.

www.manaraa.com

# Chapter 6

## Molecular ordering of mixed surfactants in mesoporous silicas: A solid-state NMR study

Published in *Solid-state NMR,* http://dx.doi.org/10.1016/j.ssnmr.**2011**.02.001

Takeshi Kobayashi, Kanmi Mao, Shy-Guey Wang, Victor S.-Y Lin, and Marek Pruski

### 6.1 Abstract

The use of mixed surfactants in the synthesis of mesoporous silica nanoparticles (MSNs) is of importance in the context of adjusting pore structures, sizes and morphologies. In the present study, the arrangement of molecules in micelles produced from a mixture of two surfactants, cetyltrimetylammoium bromide (CTAB) and cetylpyridinium bromide (CPB), was detailed by solid-state NMR spectroscopy. Proximities of methyl protons in the trimethylammonium headgroup of CTAB and protons in the pyridinium headgroup of CPB were observed under fast magic-angle spinning (MAS) by $^{1}H$–$^{1}H$ double quantum (DQ) MAS NMR and NOESY. This result suggested that CTAB and CPB co-exist in the pores without forming significant monocomponent domain structures. $^{1}H$–$^{29}Si$ heteronuclear correlation (HETCOR) NMR showed that protons in the headgroup of CTAB are in closer proximity to the silica surface than those in the CPB headgroups. On the other hand, relatively strong interaction was found between the silica surface and protons in the alkyl chain of the CPB molecule, suggesting that it assumes a 'folded-over' conformation near the pore wall. The structural information obtained in this investigation leads to better understanding of the mechanisms of self assembly and their role in determining the structure and morphology of mesoporous materials.

### 6.2 Introduction

www.manaraa.com

The use of templates to synthesize mesoporous silicas such as MCM-41 or SBA-15 has opened up new opportunities for controlling the structure of ordered porous materials, including pore size and particle morphology [1,2]. These characteristics are important for their applications as support materials in catalysis, adsorbents for separations or drug delivery, and membranes. The structure and size of pores in mesoporous materials can be controlled by using templates with different alkyl chain lengths [1,3,4], by expanding the template micelles with organic additives [1,5-7], by introducing a different type of organosilane in addition to TEOS, and controlling its concentration [8], or by using mixed micelles [9-13]. In particular, Khushalani et al. reported that pore size can be continuously tuned by changing the mixing ratio of two different surfactants [9]. The ratio of the surfactants in the resultant 'bulk' material was shown to be the same as in the starting mixture. However, the distribution and arrangement of mixed surfactants inside the pores are not well understood.

In the present study, we synthesized mesoporous silica nanoparticles (MSNs) using a mixture of two surfactants, cetyltrimethylammonium bromide (CTAB) and cetylpyridinium bromide (CPB), and studied the arrangement of these surfactants inside the MSN pores by solid-state NMR. We demonstrate that detailed structural information about internuclear proximities and molecular motions can be obtained from two-dimensional correlation NMR experiments exploiting homo- and heteronuclear dipolar interactions in the regime of fast magic angle spinning (MAS).

## 6.3 Materials and Methods

*MSN materials*

The samples were prepared following the previously described procedures [14]. A mixture of cetyltrimethylammonium bromide surfactant ($CH_3(CH_2)_{15}N(CH_3)_3Br$, referred to as CTAB) (0.5 g), cetylpyridinium bromide surfactant ($CH_3(CH_2)_{15}C_5H_5NBr$, referred to as CPB) (0.5 g), 2.0 M NaOH (3.5 ml), and $H_2O$ (480 ml) was heated at 80 °C for 30 min with

www.manaraa.com

constant stirring. To this clear solution, 5 ml of tetraethoxysilane ($Si(OCH_3)_4$, referred to as TEOS) was injected over 10 min yielding an opaque reaction mixture. The white solid products of synthesis were observed after vigorous stirring of the mixture for ~ 2 min. The as-synthesized mesoporous material, denoted as CTAB/CPB-MSN, was obtained after an additional 2 h of heating at 80 °C, followed by hot filtration, washing with a copious amount of water and ethanol, and drying under a vacuum. The same synthetic protocol was followed to prepare CTAB-MSN and CPB-MSN, where instead of the mixed surfactants 1 g of CTAB or 1 g of CPB was used, respectively.

*Solid-State NMR*

Solid-state NMR experiments were performed at 14.1 T on a Varian NMR System spectrometer, equipped with a 1.6-mm triple resonance FastMAS$^{TM}$ probe and operated at 599.6 MHz for $^1$H and 119.1 MHz for $^{29}$Si nuclei. A series of one- and two-dimensional (1D and 2D) experiments was carried out, including 1D $^1$H single-quantum (SQ) MAS, 2D $^1$H–$^1$H double-quantum (DQ) MAS, 2D NOESY and 2D $^1$H–$^{29}$Si heteronuclear correlation (HETCOR) NMR. All experiments were performed under fast MAS at a rate of 40 kHz.

The DQ coherences between $^1$H nuclei were obtained by dipolar recoupling using back-to-back (BABA) pulse sequence [15-17]. The $^1$H–$^{29}$Si spectra were acquired using cross-polarization (CP) and Car-Purcell-Meiboom-Gill (CPMG) refocusing of Si magnetization, as described earlier [14,18]. All pertinent experimental conditions are given in captions to Figures 6.2-6.5 using the following symbols: $\nu_{RF}^{X}$ the magnitude of the radio frequency magnetic field applied to X spins; $\nu_R$, the MAS rate; $\tau_R = (\nu_R)^{-1}$, the rotor period; $\tau_{CP}$, the cross-polarization time; $\tau_m$, the mixing time for NOESY; $\tau_{CPMG}$, the time interval between $\pi$ pulses in the CPMG sequence; $N_{CPMG}$, the number of echoes used during the CPMG acquisition; $\Delta t_1$, the increment of $t_1$ during 2D acquisition; $\tau_{RD}$, the recycle delay; and NS, the

www.manaraa.com

number of scans. $^{29}Si$ and $^{1}H$ chemical shifts were referenced with respect to tetramethylsilane (TMS) at 0 ppm.

## 6.4 Results and discussion

*Characterizations*

The XRD patterns of CTAB-MSN and CTAB/CPB-MSN (Figure 6.1a) indicate that the mesoporous channels are arranged in 2D hexagonal arrays. This was confirmed by the TEM images (Figure 6.1b), which also show that the particles having spherical shapes with an average diameter of ~150 nm. The physical properties of CTAB-MSN and CTAB/CPB-MSN obtained from XRD and nitrogen adsorption are listed in Table 6.1. The unit size and surface area of both materials are similar; however, the CTAB/CPB-MSNs have a larger pore diameter and thinner walls.

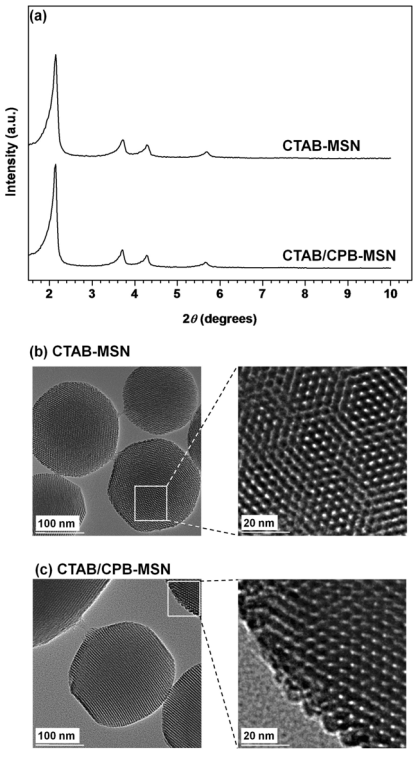


**Figure 6.1**. (a) Powder X-ray diffraction patterns and TEM images of (b) CTAB-MSN and (c) CTAB/CPB-MSN.

www.manaraa.com

Table 6.1. Structural properties of CTAB-MSN and CTAB/CPB-MSN.

| | CTAB | CTAB/CPB |
|---|---|---|
| *d*-spacing (nm)[(a)] | 4.1 | 4.1 |
| Pore diameter (nm)[(b)] | 3.0 | 3.3 |
| Surface area ($m^2/g$)[(b)] | 1058 | 1097 |
| Wall thickness (nm)[(c)] | 1.1 | 0.80 |

[(a)]The *d*-spacing (or unit cell size) corresponds to the main (100) XRD peak.

[(b)]The pore diameter and the surface area were obtained from the nitrogen adsorption/desorption data.

[(c)]The pore wall thickness is the difference between the *d*-spacing and pore diameter.

*Solid-State NMR*

*1D $^1H$ MAS spectra*. Figure 6.2a shows the $^1H$ SQMAS NMR spectrum of CTAB/CPB-MSN, along with the relevant structures and spectral assignments. The observed $^1H$ chemical shifts agree with those measured in homogeneous solutions of the corresponding surfactants. The resonances representing H3, H6, H8 and H10 are barely resolved, whereas those due to H4 and H5 overlap at around 3.5 ppm. The CTAB/CPB ratio in the CTAB/CPB-MSN sample was estimated by comparing the integrated signal intensities of protons in the headgroups of CTAB (H5 and H4) and CPB (H8-10). The resulting molar ratio (48/52) is equivalent to the CTAB/CPB ratio used in the synthesis (49/51).

Also shown, in Figure 6.2b, is the SQ projection of the $^1H$–$^1H$ DQMAS NMR spectrum of the same sample. We note that all resonances observed in the DQMAS spectrum have increased linewidth and lower spectral intensity compared to their SQMAS counterparts in Figure 6.2a. The increased linewidth is attributed to the selective nature of DQMAS measurement, which exploits homonuclear dipolar couplings and thus favors the strongly coupled $^1H$-$^1H$ pairs [19]. The lower intensity is due to DQ filtering, which will be discussed in more detail below. Here we only point out that Figure 6.2b lacks a broad resonance

www.manaraa.com

centered at around 5.8 ppm, which would represent hydrogen-bonded silanol groups on the silica surface [20,21].

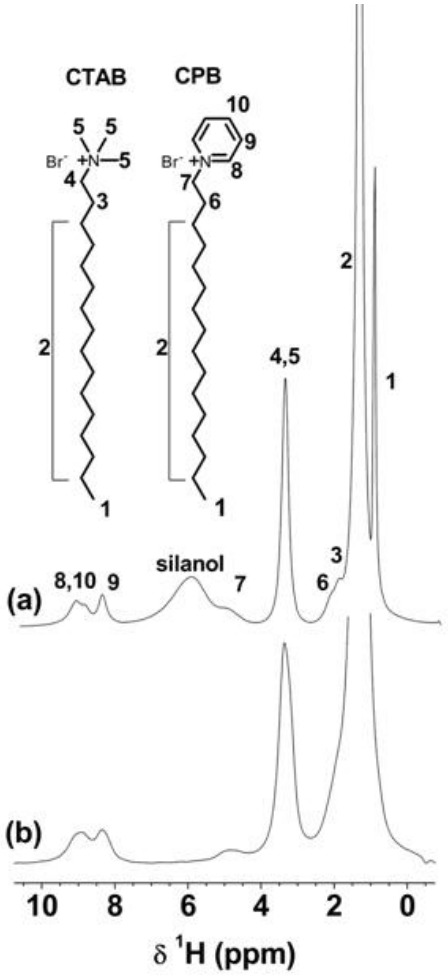


**Figure 6.2**. (a) $^{1}$H SQMAS spectrum of CTAB/CPB-MSN obtained using $\nu_R$ = 40 kHz, $\nu_{RF}^{H}$ = 120 kHz, $\tau_{RD}$ = 5 s, and NS = 16. (b) SQ projection of $^{1}$H-$^{1}$H DQMAS spectrum in Figure 6.3d. The spectra are scaled for visual clarity.

Also shown, in Figure 6.2b, is the SQ projection of the $^{1}$H–$^{1}$H DQMAS NMR spectrum of the same sample. We note that all resonances observed in the DQMAS spectrum have increased linewidth and lower spectral intensity compared to their SQMAS counterparts in Figure 6.2a. The increased linewidth is attributed to the selective nature of DQMAS

www.manaraa.com

measurement, which exploits homonuclear dipolar couplings and thus favors the strongly coupled $^{1}$H-$^{1}$H pairs [19]. The lower intensity is due to DQ filtering, which will be discussed in more detail below. Here we only point out that Figure 6.2b lacks a broad resonance centered at around 5.8 ppm, which would represent hydrogen-bonded silanol groups on the silica surface [20,21].

*Transverse relaxation*

The transverse relaxation time ($T_2$') of $^{1}$H nuclei (Table 6.2) was measured using a spin-echo sequence ($\pi/2$ - $\tau/2$ - $\pi$ - $\tau/2$ - detect) under 40 kHz MAS without $^{1}$H–$^{1}$H RF homonuclear decoupling. The relaxation due to the inhomogeneous component of the dipolar interactions and the anisotropic part of the $^{1}$H chemical shift (CSA) was eliminated by using $\tau$ values equal to the integer number of rotor periods, $\tau = n\tau_R$. Thus, the relaxation data reported in Table 6.2 are mainly affected by the residual homogeneous contribution from $^{1}$H-$^{1}$H dipolar coupling. The surfactants are expected to be intertwined within the pores, exhibiting a wide range of mobilities. The resulting spin dynamics in CTAB/CPB-MSN is too complex to permit exact rationalization of the observed $T_2$' values, as it also depends on the effective dimensionality of the coupling network and the interference between molecular motions and line-narrowing by MAS [22]. Still, the relaxation measurements can provide useful general insights into the mobility of different molecular groups in CTAB and CPB.

Table 6.2. Transverse relaxation time, $T_2$', in CTAB/CPB-MSN

| Moiety | | Proton | $T_2$' (ms) |
|---|---|---|---|
| $CH_3$ | tail | H1 | 27.3 |
| $CH_2$ | chain | H2 | 9.2 |
| $CH_3$ | CTAB head | H(4,5) | 5.6 |
| CH | CPB head | H(8-10) | 2.5 |

www.manaraa.com

We first note that the values reported in Table 6.2 exceed those typically observed in rigid organic materials, suggesting significant overall mobility. For example, the $^1$H $T_2'$ times measured under similar conditions ($\nu_R$ = 41.667 kHz) in crystalline tripeptide (N-formyl-L-methionyl-L-leucyl-L-phenylalanine, f-MLF-OH), which for the most part represents a strongly coupled spin system, were on the order of 1 ms or less [23]. Here, the longest $T_2'$ time (~27 ms) was associated with H1, indicating that the most mobile of the methyl groups are in the tail ends of CTAB and CPB are. This is consistent with the result of the DQMAS experiment shown in Figure 6.2b, in which the resonance representing H1 is largely depleted, suggesting the weakest coupling to other protons. The mobilities of protons H(4,5) and H(8-10) appear to be the most restricted. In an aqueous solution, the surfactants self-organize in such a way that the hydrophilic cationic headgroups participate in the deposition of a silicate precursor (here, TEOS) during the synthesis process. Thus, the small $T_2'$ values of H(4,5) and H(8-10) are due to the interactions between the headgroups of CTAB or CPB and the silica surface inside the pores of the MSNs. In the absence of any motions other than fast reorientation of the $CH_3$ groups, both headgroups should exhibit comparable relaxation. The fact that the $T_2'$ value of H(8-10) is smaller by a factor of ~2 than that of H(4,5), suggests the CPB headgroup is less mobile.

*$^1$H–$^1$H DQMAS and NOESY*

To investigate the proximity between various molecular fragments within the pores, we used the $^1$H–$^1$H DQMAS experiment, which serves to produce 2D correlations between the DQ and SQ coherences of spins that undergo strong dipolar interactions [15]. In the present study, the MAS-averaged dipolar interactions were reintroduced using a back-to-back (BABA) pulse sequence [17], which was chosen because of its robustness and insensitivity to off-resonance effects. In the DQ dimension, the signals representing two coupled nuclei resonating at $\omega_1$ and $\omega_2$ appear at the sum frequency $\omega_1 + \omega_2$, whereas the signals from non-coupled nuclei are removed by the DQ filter. Consequently, *all* cross-peaks in the DQMAS

www.manaraa.com

spectra result from spins in spatial proximity to each other. This is in contrast to the 2D SQ-SQ spectra based on an inter-spin exchange of magnetization, which are typically dominated by strong diagonal signals representing non-exchanged magnetization.

The 2D $^{1}H$–$^{1}H$ DQMAS spectra of CTAB-MSN, CPB-MSN and CTAB/CPB-MSN are shown in Figures 6.3a, 6.3b and 6.3d, respectively. Figure 6.3c depicts the result of the same experiment on a physical mixture of CTAB-MSN and CPB-MSN corresponding to the molar ratio of CTAB:CPB equal to 43:57 (CTAB+CPB-MSN-phys). The spectra of CTAB-MSN and CPB-MSN are dominated by strong diagonal peaks due to interactions between H2 protons. Also present in Figures 6.3a and 6.3b are the cross-peaks H(4,5)–H(4,5) and H2–H(4,5) in CTAB-MSN, as well as H2–H7, H2–H(8,10), H2–H9, H7–H7, H7–H(8-10) and superimposed cross-peaks involving H8, H9 and H10 in CPB-MSN. Signals associated with H1, H3 and H6 were not identified because of strong overlap with the dominant resonances representing H2. All cross-peaks observed in these two spectra can be attributed to a combination of intra- and intermolecular interactions. As expected, the physical mixture of CTAB-MSN and CPB-MSN yielded a result similar to the sum of individual components (Figure 6.3c). The spectrum of CTAB/CPB-MSN (Figure 6.3d) exhibits one notable difference: a pair of cross-peaks representing H(4,5)–H(8-10), whose presence unambiguously manifests that both surfactants occupy the same pores of CTAB/CPB-MSN such that the methyl groups in the CTAB headgroups and the pyridyl group in the CPB headgroups are located within the distance at which their protons are coupled with each other. The H(4,5)–H(8-10) correlation is quite weak and is no longer observed with 200 μs of excitation/reconversion period. Considering the restricted mobility of the CTAB and CPB headgroups, the presence of a weak H(4,5)–H(8-10) cross-peak suggests that the two surfactants form small individual patches with limited boundaries between them, or are well mixed in such a way that their headgroups are not coaligned.

www.manaraa.com

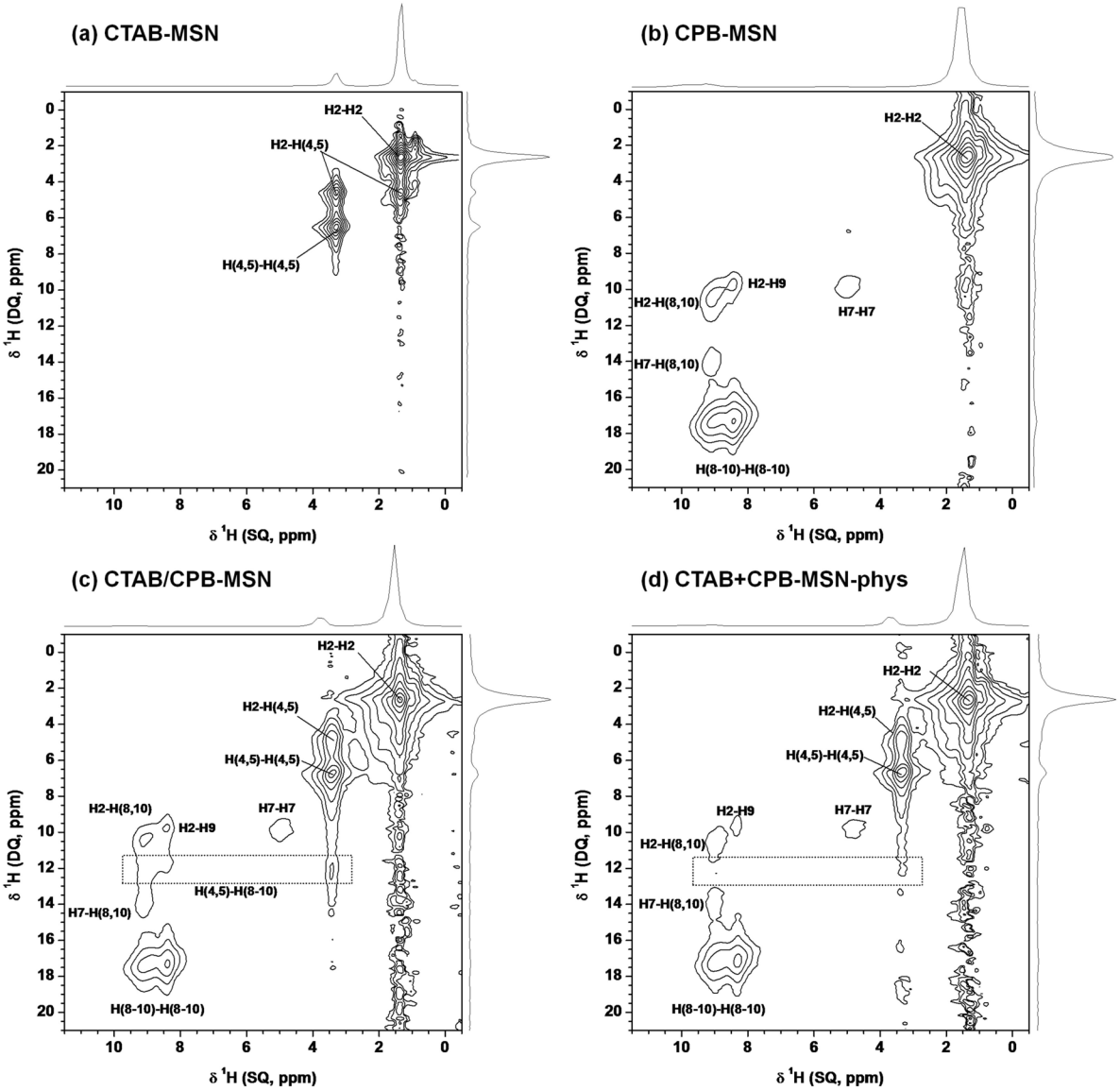


**Figure 6.3**. 2D $^{1}$H-$^{1}$H DQMAS spectra of (a) CTAB-MSN, (b) CPB-MSN, (c) physical mixture of CTAB-MSN and CPB-MSN, and (d) CTAB/CPB-MSN measured using a back-to-back (BABA) sequence with excitation and reconversion lengths of 100 μs ($4\tau_R$), $\nu_R$ = 40 kHz and $\nu_{RF}^{H}$ = 120 kHz. The acquisition involved 800 rows, with 16 scans per row, $\Delta t_1$ = 50 μs, and $\tau_{RD}$ = 1.2 s.

www.manaraa.com

Figure 6.4a shows the NOESY spectrum of CTAB/CPB-MSN. In contrast to DQMAS, the NOESY experiments are better suited for studying weak couplings between pairs of protons contributing to incoherent cross-relaxation processes [19,24]. A number of cross-peaks involving protons in CTAB headgroups, CPB headgroups, alkyl chains and surface silanol groups were observed with 20 ms of mixing time. The H(4,5)-H(8-10) cross-peaks barely visible in the DQMAS spectrum in Figure 6.3d appeared with much greater intensity. This observation further confirmed that CTAB headgroups and CPB headgroups interact with each other. In addition, the cross-peaks representing correlations between both surfactants and the silanol groups on silica surface were observed in the NOESY spectrum. One of these peaks involves the H6 protons in CPB, marked with the shaded area in Figure 6.4a. Considering the distance between the silica surface and silanol proton (~2Å, assuming $SiO_2$(111)-type surface), the presence of such a cross-peak implies that CPB headgroups rest flat on the silica surface or assume a folded-over conformation.

To further refine the understanding of interactions between both surfactants and the silica surface, we measured the NOE build-up curves, which reflect the strength of dipolar coupling between spins. In Figure 6.4b, we show the NOE build-up curves of cross-peaks involving the headgroups of CTAB and CPB (H(4,5) and H(8-10), respectively). The H(8-10)–silanol cross-peak builds up faster than the H(4,5)–silanol cross-peak, which suggests that (1) the CPB headgroups are less mobile than the methyl groups in the CTAB headgroups (as also indicated by the $T_2$' measurements), and/or (2) the protons in the CPB headgroups are closer to the silanols than those in the CTAB headgroups. This second possibility is not supported by the results of $^{1}H$–$^{29}Si$ HETCOR NMR discussed below.

www.manaraa.com

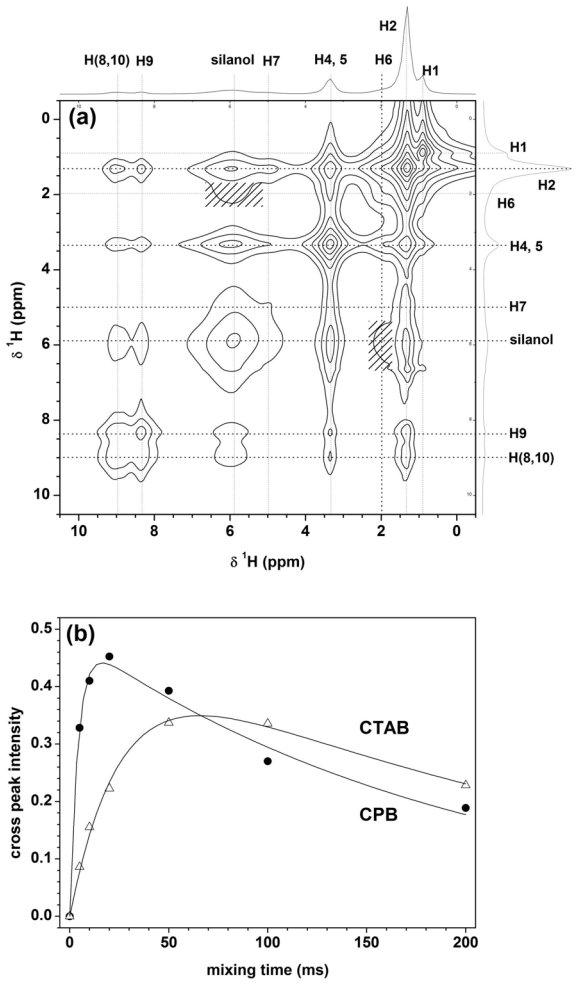


**Figure 6.4**. (a) NOESY spectrum of CTAB/CPB-MSN obtained using $\nu_R$ = 40 kHz, $\nu_{RF}^{H}$ = 120 kHz, and $\tau_m$ = 20 ms. The data were acquired in 800 rows, with $\Delta t_1$ = 50 μs, 8 scans per row, and $\tau_{RD}$ = 1.2 s. (b) Intensities of NOESY cross-peaks representing the CTAB headgroup-silanol and the CPB headgroup-silanol interactions as a function of mixing time, $\tau_m$. The intensities are normalized to similar heights.

*$^{1}H$–$^{29}Si$ HETCOR*

Finally, 2D $^{1}$H–$^{29}$Si HETCOR NMR measurements were carried out to probe the dipolar interactions between $^{1}$H nuclei in the surfactants and $^{29}$Si nuclei on the silica surface. The spectra of samples CTAB-MSN, CPB-MSN and CTAB/CPB-MSN, acquired under the same

www.manaraa.com

conditions (except $\tau_{CP}$ = 15 ms for CPB-MSN) are shown in Figure 6.5. $^{1}H–^{29}Si$ correlations associated with H2, H(4,5), H6 and H(8-10) were observed in the $^{1}H–^{29}Si$ spectrum of CTAB/CPB-MSN (Figure 6.5c). Interestingly, this spectrum differs from the sum of spectra representing CTAB-MSN and CPB-MSN (Figures 6.5a and 6.5b, respectively). The volume of the cross-peak H(8-10)–Si is about 3 times lower than that for H(4,5)–Si, after accounting for the number of protons involved in the CP transfer. Thus, the resonances representing the CPB headgroups are strongly underrepresented in Figure 6.5c, in spite of the higher rigidity of these groups, which should favor efficient $^{1}H–^{29}Si$ polarization transfer. This strongly suggests that in CTAB/CPB-MSN the CPB headgroups are more distant from the silica surface than the CTAB headgroups.

We also note that the volume of cross-peak representing H(8-10)–Si in CTAB/CPB-MSN is disproportionally low compared to that of H2–Si in the same sample. In CPB-MSN, these two cross-peaks have roughly the same volumes, whereas the cross-peak volume of the H(8-10)–Si is only half of that of H2–Si (assuming that ~half of the H2 protons belong to CPB, as indicated by $^{1}H$ SQMAS). We further point out that the cross-polarization time ($\tau_{CP}$) leading to the strongest H(8-10)–Si cross-peak was shorter in CPB-MSN than in CTAB/CPB-MSN. Again, these observations are consistent with the increased distance between the CPB headgroup and the silica surface in the mixed micelles. Finally, a cross-peak was observed in CTAB/CPB-MSN, representing proton H6, associated with the carbon that is located in the beta position to the pyridyl ring in CPB. This finding, which agrees with the result of the NOESY experiment shown in Figure 6.4a, suggests that the pyridyl headgroup of the CPB assumes a folded-over conformation near the outer surface of the micelle. This folded-over conformation of the CPB in the mixed micelles provides additional evidence for CTAB-CPB miscibility. If the surfactants were present in separate domains, the CPB headgroups would be expected to yield an intense H(8-10)–Si cross-peak, similar to that in CPB-MSN.

www.manaraa.com

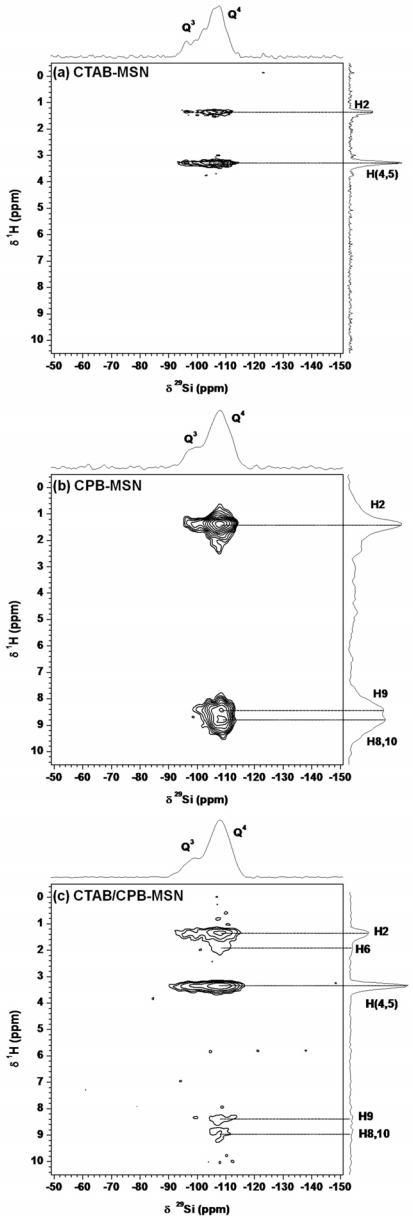


**Figure 6.5**. 2D $^{1}$H-$^{29}$Si CP-based CPMG-HETCOR spectra of (a) CTAB-MSN, (b) CPB-MSN, and (c) CTAB/CPB-MSN, obtained using $\nu_R$ = 40 kHz, $\nu_{RF}^{H}$ = 120 kHz during short pulses, $\nu_{RF}^{H}$ = 60 kHz during tangent CP, $\nu_{RF}^{H}$ = 10 kHz during SPINAL-64 decoupling, $\nu_{RF}^{Si}$ = 100 kHz during short pulses and CP, $\tau_{CP}$ = 20 ms (15 ms for CPB-MSN), $N_{CPMG}$ = 50, and $\tau_{CPMG}$ = 6 ms. The data were acquired in 512 rows, with $\Delta t_1$ = 100 µs, 96 scans per row, and $\tau_{RD}$ = 1.2 s.

www.manaraa.com

*Molecular ordering in CTAB/CPB-MSN*

Taken together, our findings corroborate the arrangement of CTAB and CPB inside the pores shown schematically in Figure 6.6. In CTAB-MSN the methyl functionalities in the trimethylammonium headgroups are located next to the silica surface, as is well known from earlier studies [25]. Similarly, the pyridyl headgroups of CPB in CPB-MSN assume a prone configuration in close proximity to silica, which again is in agreement with an earlier study of CPB adsorption on clay (montmorillonite) [26]. In the pores of CTAB/CPB-MSN, the surfactants appear to be intimately mixed with each other, without forming large separate domains. However, the headgroups of CTAB and CPB are not aligned next to each other. The trimethylammonium functionalities in CTAB are located closer to the silica surface, whereas the pyridyl groups in CPB appear to be more distant, most probably in folded-over position pointing away from the surface. The intermolecular interactions between the tailgroups could not be directly probed here because their NMR fingerprints in CTAB and CPB are indistinguishable. Since the pore radius in CTAB/CPB-MSN (~1.6 nm) is much smaller than the length of the surfactant molecules (~2.3 nm), their tailgroups are most likely intertwined inside the micelles. The folding of CPB molecules near the outer surface may be partly responsible for the difference between the pore radii, as well.

www.manaraa.com

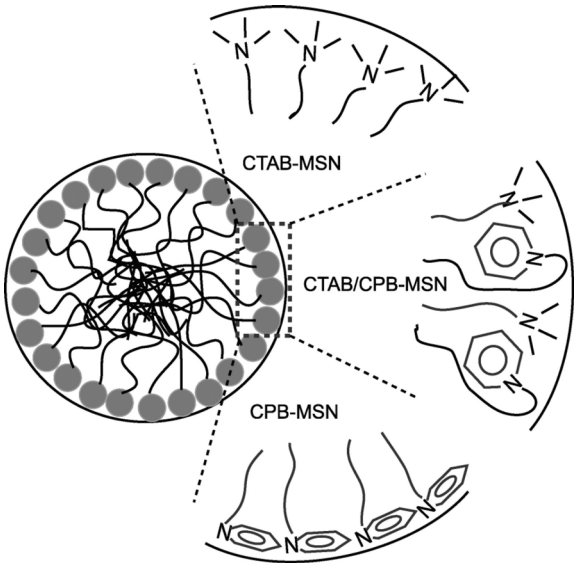


**Figure 6.6**. Schematic diagram of the arrangement of CTAB and CPB inside the pores of CTAB MSN, CPB-MSN and CTAB/CPB-MSN materials.

### 6.5 Conclusions

The results of 1D and 2D solid-state NMR measurements provided valuable insights into the arrangement of surfactants in MSN materials synthesized from mixed micelles composed of CTAB and CPB. Study of the detailed arrangement of the surfactants is important for understanding the mechanism by which pore structures can be adjusted, thereby 'tailoring' the morphologies of these materials to various applications, including the synthesis of mesoporous materials from mixed oxides.

### 6.6 Acknowledgment

This research was supported at the Ames Laboratory by the U.S. Department of Energy, Office of Basic Energy Sciences, under Contract No. DE-AC02-07CH11358.

### 6.7 References

www.manaraa.com

[1] J.S. Beck, J.C. Vartuli, W.J. Roth, M.E. Leonowicz, C.T. Kresge, K.D. Schmitt, C.T.W. Chu, D.H. Olson, E.W. Sheppard, S.B. McCullen, J.B. Higgins, and J.L. Schlenker, A new family of mesoporous molecular sieves prepared with liquid crystal templates, *J. Am. Chem. Soc.* 114 (1992) 10834-10843.

[2] C.G. Goltner, and M. Antonietti, Mesoporous materials by templating of liquid crystalline phases, *Adv. Mater.* 9 (1997) 431-436.

[3] C.T. Kresge, M.E. Leonowicz, W.J. Roth, J.C. Vartuli, and J.S. Beck, Ordered mesoporous molecular sieves synthesized by a liquid-crystal template mechanism, *Nature* 359 (1992) 710-712.

[4] D.Y. Zhao, J.L. Feng, Q.S. Huo, N. Melosh, G.H. Fredrickson, B.F. Chmelka, and G.D. Stucky, Triblock copolymer syntheses of mesoporous silica with periodic 50 to 300 angstrom pores, *Science* 279 (1998) 548-552.

[5] J.L. Blin, and B.L. Su, Tailoring pore size of ordered mesoporous silicas using one or two organic auxiliaries as expanders, *Langmuir* 18 (2002) 5303-5308.

[6] A. Sayari, M. Kruk, M. Jaroniec, and I.L. Moudrakovski, New approaches to pore size engineering of mesoporous silicates, *Adv. Mater.* 10 (1998) 1376-1379.

[7] M. Luechinger, G.D. Pirngruber, B. Lindlar, P. Laggner, and R. Prins, The effect of the hydrophobicity of aromatic swelling agents on pore size and shape of mesoporous silicas, *Microporous Mesoporous Mat.* 79 (2005) 41-52.

[8] S.G. Wang, C.W. Wu, K.M. Chen, and V.S.Y. Lin, Fine-tuning mesochannel orientation of organically functionalized mesoporous silica nanoparticles, *Chem.-Asian J.* 4 (2009) 658-661.

[9] D. Khushalani, A. Kuperman, N. Coombs, and G.A. Ozin, Mixed surfactant assemblies in the synthesis of mesoporous silicas, *Chem. Mat.* 8 (1996) 2188-2193.

[10] F.X. Chen, L.M. Huang, and Q.Z. Li, Synthesis of MCM-48 using mixed cationic-anionic surfactants as templates, *Chem. Mat.* 9 (1997) 2685-2686.

www.manaraa.com

[11] Y.R. Cheng, H.P. Lin, and C.Y. Mou, Control of mesostructure and morphology of surfactant-templated silica in a mixed surfactant system, *PCCP Phys. Chem. Chem. Phys.* 1 (1999) 5051-5058.

[12] Z.Y. Yuan, T.H. Chen, J.Z. Wang, and H.X. Li, Synthesis of mesostructured lamellar aluminophosphates in the presence of alkylpyridinium cationic surfactant, *Mater. Chem. Phys.* 68 (2001) 110-118.

[13] S. Namba, A. Mochizuki, and M. Kito, Fine control of pore size of highly ordered MCM-41 by using template mixtures of dodecyltrimethylammonium bromide/hexadecyltrimethylammonium bromide with various molar ratios, *Chem. Lett.* (1998) 569-570.

[14] J. Trebosc, J.W. Wiench, S. Huh, V.S.Y. Lin, and M. Pruski, Studies of organically functionalized mesoporous silicas using heteronuclear solid-state correlation NMR spectroscopy under fast magic angle spinning, *J. Am. Chem. Soc.* 127 (2005) 7587-7593.

[15] S.P. Brown, and H.W. Spiess, Advanced solid-state NMR methods for the elucidation of structure and dynamics of molecular, macromolecular, and supramolecular systems, *Chem. Rev.* 101 (2001) 4125-4155.

[16] I. Schnell, S.P. Brown, H.Y. Low, H. Ishida, and H.W. Spiess, An investigation of hydrogen bonding in benzoxazine dimers by fast magic-angle spinning and double-quantum $^{1}$H NMR spectroscopy, *J. Am. Chem. Soc.* 120 (1998) 11784-11795.

[17] M. Feike, D.E. Demco, R. Graf, J. Gottwald, S. Hafner, and H.W. Spiess, Broadband multiple-quantum NMR spectroscopy, *Journal of Magnetic Resonance Series A* 122 (1996) 214-221.

[18] J.W. Wiench, V.S.Y. Lin, and M. Pruski, $^{29}$Si NMR in solid state with CPMG acquisition under MAS, *J. Magn. Reson.* 193 (2008) 233-242.

www.manaraa.com

[19] G.R. Goward, M.F.H. Schuster, D. Sebastiani, I. Schnell, and H.W. Spiess, High-resolution solid-state NMR studies of imidazole-based proton conductors: Structrue motifs and chemical exchange from $^{1}$H NMR, *J. Phys. Chem. B* 106 (2002) 9322-9334.

[20] B. Grunberg, T. Emmler, E. Gedat, I. Shenderovich, G.H. Findenegg, H.H. Limbach, and G. Buntkowsky, Hydrogen bonding of water confined in mesoporous silica MCM-41 and SBA-15 studied by $^{1}$H solid-state NMR, *Chem.-Eur. J.* 10 (2004) 5689-5696.

[21] I.S. Chuang, D.R. Kinney, and G.E. Maciel, Interior hydroxyls of the silica gel system as studied by silico-29 CP-MAS NMR spectroscopy, *J. Am. Chem. Soc.* 115 (1993) 8695-8705.

[22] A.N. Garroway, Homogeneous and inhomogeneous nuclear spin echoes in organic solids: Adamantane, *J. Magn. Reson.* 28 (1977) 365-371.

[23] K.M. Mao, and M. Pruski, Directly and indirectly detected through-bond heteronuclear correlation solid-state NMR spectroscopy under fast MAS, *J. Magn. Reson.* 201 (2009) 165-174.

[24] T.M. Alam, B.C. Tischendorf, and R.K. Brow, High-speed $^{1}$H MAS investigations of the weathered surface of a phosphate glass, *Solid State NMR* 27 (2005) 99-111.

[25] A. Firouzi, F. Atef, A.G. Oertli, G.D. Stucky, and B.F. Chmelka, Alkaline lyotropic silicate-surfactant liquid crystals, *J. Am. Chem. Soc.* 119 (1997) 3596-3610.

[26] D.J. Greenland, and J.P. Quirk, Determination of surface areas by adsorption of cetyl pyridinium bromide from aqueous solution, *J. Phys. Chem.* 67 (1963) 2886-2887.

www.manaraa.com